Genetic Optimization of Turbomachinery Components using the Volute of a Transonic Centrifugal Compressor as a Case Study

To the Faculty of Mechanical, Process and Energy Engineering
of the Technische Universität Bergakademie Freiberg
approved

THESIS

to attain the academic degree of
Doktor-Ingenieur
(Dr.-Ing),

submitted

by Dipl.-Ing. Martin Heinrich
born on the July 2, 1985 in Freiberg

Reviewers: Prof. Dr.-Ing. habil. Rüdiger Schwarze, TU Bergakademie Freiberg
Prof. Dr.-Ing. habil. Ulrich Groß, TU Bergakademie Freiberg

Date of the award: November 22, 2016

Excerpts of this work have been published in peer-reviewed international journals and international conference proceedings:

M. Heinrich and R. Schwarze: *Simulation and Validation of the Compressor Stage of a Turbocharger using OpenFOAM*, 8th International Conference on Compressors and their Systems, ISBN: 978-1-78242-169-6, London, United Kingdom, 2013.

M. Heinrich and R. Schwarze: *All-Mach Number Density Based Flow Solver for OpenFOAM*, ASME Turbo Expo 2014: Power for Land, Sea and Air, no. GT2014-94511, DOI: 10.1115/GT2014-26220, Düsseldorf, Germany, 2014.

M. Heinrich and R. Schwarze: *Scripted CFD-Tool for the Automated Design of Volutes for Centrifugal Compressors*, ASME Turbo Expo 2015: Power for Land, Sea and Air, no. GT2015-42629, DOI: 10.1115/GT2015-42629, Montreal, Canada, 2015.

M. Heinrich and R. Schwarze: *Genetic Algorithm Optimization of the Volute Shape of a Centrifugal Compressor*, International Journal of Rotating Machinery, Volume 2016, 13 pages, DOI: 10.1155/2016/4849025, 2016.

Declaration

I hereby declare that I completed this work without any improper help from a third party and without using any aids other than those cited. All ideas derived directly or indirectly from other sources are identified as such.

In the selection and in the use of materials and in the writing of the manuscript I received support from the following persons:

Professor Dr.-Ing. habil. Rüdiger Schwarze

Persons other than those above did not contribute to the writing of this thesis. I did not seek the help of a professional doctorate-consultant. Only persons identified as having done so received any financial payment from me for any work done for me.

This thesis has not previously been submitted to another examination authority in the same or similar form in Germany or abroad.

Abstract

One elementary part of a centrifugal compressor is the volute, which is located downstream the impeller. Its purpose is to collect the flow and increase the static pressure by converting kinetic energy into potential energy. Despite its significant effect onto the design point and operating range of the compressor, the number of publications regarding this component is quite small. Therefore, a numerical optimization of the volute housing is performed in order to identify important geometric parameters and find an optimal volute geometry. For this purpose, a new density-based CFD solver for all Mach numbers is developed as well as an automated geometry generation tool for the volute housing.

The results show, that a volute with an inlet eccentricity of 0.9 and a slightly lower radial volute channel offers the best compressor efficiency. Moreover, the actual cross-sectional shape of the volute has only a minor influence onto the performance. As a result, the isentropic efficiency could be improved by up to 2 % compared to the reference compressor model, in particular at high off-design flow rates. These results are a novelty in the scientific community and help to design more efficient compressors.

Contents

List of Figures

List of Tables

Nomenclature

Latin Symbols

a	m^2/s	Thermal diffusivity
a_1, b_1, c_1	-	Constants in the SST $k-\omega$ turbulence model
A, $\underline{A}$	m^2	Area, surface area vector
b	m	Height of volute inlet
B	-	Constant in law of the wall
c_{r1}, c_{r2}, c_{r3}	-	Constants in the SST $k-\omega$ RC correction
c	m/s	Speed of sound
c_p	$\mathrm{J}/(\mathrm{kg\,K})$	Specific heat capacity at constant pressure
c_v	$\mathrm{J}/(\mathrm{kg\,K})$	Specific heat capacity at constant volume
$\underline{C}$	-	Curve of B-spline
C_1	$\mathrm{kg}/(\mathrm{m\,s}\sqrt{\mathrm{K}})$	Constant in Sutherland's law
C_2	K	Constant in Sutherland's law
C_p	-	Static pressure recovery coefficient
C_D	-	Drag coefficient
C_μ	-	Constant for turbulent inlet condition
$CD_{k\omega}$, $CD_{k\omega,\mathrm{min}}$	-	Limiter and constant in the F_1 blending function of the SST $k-\omega$ turbulence model
Co	-	Courant number
d	m	Diameter

D	1/s	Function in the SST $k-\omega$ RC correction
e	-	Eccentricity
e	m^2/s^2	Specific internal energy
E	m^2/s^2	Specific total energy
f	1/s	Vortex shedding frequency
$f(\underline{x})$	-	Function object
f_{r1}, f_{rot}	-	Functions in the SST $k-\omega$ RC correction
F_1, F_2, F_3	-	Blending functions in the SST $k-\omega$ turbulence model
$\underline{F}$	[various]	Numerical fluxes
$\underline{F}_{\text{D}}$	N	Drag force
g	m/s^2	Gravitational acceleration
g	-	Blending function for SLAU scheme
$\underline{g}(\underline{x})$	-	Nonlinear inequality constraints
h	m	Head
$\underline{h}(\underline{x})$	-	Nonlinear equality constraints
H	m^2/s^2	Specific total enthalpy
i	-	Runge-Kutta stage counter
$\underline{\underline{I}}$	-	Identity matrix
I_t	-	Turbulent intensity
j	-	Pseudo time index
k	-	Degree of B-spline
k	m^2/s^2	Turbulent kinetic energy
k_s	m	Equivalent sand grain roughness
K_p	-	Total pressure loss coefficient
L	m	Length
L_{mix}	m	Mixing length
L_t	m	Turbulent length scale

m	-	Number of knots of B-spline
m	-	Smoothing iteration index
$\dot{m}$	kg/s	Mass flow rate
$\underline{M}$	N m	Torque
Ma	-	Mach number
n	-	Number of control points of B-spline
n	-	Physical time index
n	min^{-1}	Rotational speed
$\underline{n}$, $\underline{N}$	-	Normal vector
N	-	B-spline basis function
p	Pa	Pressure
$\underline{p}$	-	Vector of control points
$\tilde{p}$	Pa	Pressure flux
P_k, $\widehat{P}_k$	$\mathrm{kg/(s^3\,m)}$	Production of turbulent kinetic energy
P_S	$\mathrm{kg/(m\,s^3\,K)}$	Entropy production rate
P_ω	$\mathrm{kg/(s^3\,m)}$	Production of specific dissipation
Pr	-	Prandtl number
$\underline{q}$	$\mathrm{W/m^2}$	Heat flux density
r	-	Ratio of successive gradients
r, $\underline{r}$	m	Radius, radius vector
r^*, $\hat{r}$	-	Functions in the SST $k-\omega$ RC correction
R	-	Correlation coefficient
$\underline{R}$	[various]	Residuals
R_i	J/(kg K)	Specific gas constant
R_z	m	Surface roughness
Re	-	Reynolds number
s	rad	Radian of volute element
S	1/s	Magnitude of strain rate tensor

$\underline{S}$	[various]	Source term
$\underline{\underline{S}}$, S_{ij}	1/s	Strain rate tensor
St	-	Strouhal number
t	-	Control variable for B-spline
t	s	Physical time
Δt	s	Physical time step
T	K	Temperature
$\underline{T}$	-	Knot vector for B-spline
$\underline{u}$, u_i	m/s	Velocity vector, i-th component
$u_{\parallel}$	m/s	Magnitude of velocity parallel to adjacent wall
u_τ	m/s	Friction velocity
V	m^3	Volume
$\dot{V}$	m^3/s	Volumetric flow rate
w	J/kg	Specific work
W	1/s	Magnitude of rotation rate tensor
$\underline{W}$	[various]	Conserved variables
$\underline{\underline{W}}$, W_{ij}	1/s	Rotation rate tensor
x, y, z	m	Cartesian coordinates
$\underline{x}$	-	Vector of design variables
$\underline{x}$, x_i	m	Position vector, i-th component
Δx	m	Characteristic cell length
y	m	Wall distance

Greek Symbols

α	°	Flow angle
α_i	-	Stage coefficients for Runge-Kutta scheme
β	m^2/s^2	Variable for preconditioning

β_1, β_2, β^*	-	Constants in the SST $k-\omega$ turbulence model
γ	-	Isentropic exponent
γ_1, γ_2	-	Constants in the SST $k-\omega$ turbulence model
$\underline{\underline{\Gamma}}$	-	Preconditioning matrix
δ_s	$^\circ$	Separation angle
ε	-	Coefficient for preconditioning
ε_{ijk}	-	Levi-Civita symbol
ϵ	-	Smoothing coefficient
ϵ	$\mathrm{m}^2/\mathrm{s}^3$	Turbulent dissipation
ζ	-	Function for flux calculation
η	-	Efficiency
θ	rad	Circumferential angle
$\Delta\theta$	$^\circ$	Relative rotor position
κ	-	Constant in law of the wall
λ	$\mathrm{W}/(\mathrm{m\,K})$	Thermal conductivity
μ	$\mathrm{Pa\,s}$	Dynamic viscosity
ν	m^2/s	Kinematic viscosity
Π	-	Pressure ratio
ρ	kg/m^3	Density
σ_{k1}, σ_{k2}, $\sigma_{\omega1}$, $\sigma_{\omega1}$	-	Constants in the SST $k-\omega$ turbulence model
τ	s	Pseudo time
$\Delta\tau$	s	Pseudo time step
$\underline{\underline{\tau}}$	N/m^2	Viscous stress tensor
υ	$^\circ$	Angle for volute design
ϕ	-	Flow coefficient
$\phi(r)$	-	Slope limiter function
χ	-	Variable for flux calculation
ψ	-	Pressure coefficient

$\underline{\Psi}$	[various]	Primitive variables
ω	1/s	Specific dissipation
$\underline{\omega}$	1/s	Angular velocity

Subscripts

2	Impeller exit
corr	Corrected
eff	Effective
in	Inlet
inv	Inviscid
is	Isentropic
L	Lower
log	Logarithmic
max	Maximum
n	Face normal
N	Neighbour cell
out	Outlet
p	Polytropic
P	Owner cell
r	Radial direction
ref	Reference
rel	Relative
rot	Rotation
t	Turbulent
tar	Target
tot	Total
tt	Total-to-total

U	Upper
vc	Volute cross-section center
vi	Volute inlet
vis	Viscous
w	Wake
wall	Wall
θ	Circumferential direction
τ	Friction
$\parallel$	Parallel to adjacent wall

Superscripts

$\bar{\phi}$	Averaged/weighted/smoothed quantity
$\hat{\phi}$	Limited quantity
ϕ^+	Dimensionless values
$\phi^{f\pm}$	Positive / negative face values
ϕ^T	Transposed quantity
$\lvert\phi\rvert$	Magnitude of ϕ
$\lVert\phi\rVert_n$	L_n Norm

Abbreviations

ANOVA	Analysis of Variance
AUSM	Advection Upstream Splitting Method
B-spline	Basis Spline
CFD	Computational Fluid Dynamics
CHT	Conjugate Heat Transfer
COLINY	Common Optimization Library Interface

DOE	Design of Experiments
HLLC	Harten-Lax-van Leer-Contact
HPC	High Performance Computing
max	Maximum
min	Minimum
MRF	Multiple Reference Frame
NURBS	Non-Uniform Rational Basis Spline
RANS	Reynolds-Averaged Navier-Stokes
RC	Rotation and Curvature
RS	Reynolds Stress
sgn	Signum Function
SIMPLE	Semi-Implicit Method for Pressure-Linked Equations
SLAU	Simple Low-Dissipation AUSM
SST	Shear-Stress Transport
STL	Stereo Lithography
TRIP	Transformation Induced Plasticity
TVD	Total Variation Diminishing

1 Introduction

Greenhouse gases such as carbon dioxide (CO_2) are the main reason for climate change. A reduction of these emissions is inevitable to stop global warming. Next to energy industries, traffic and transportation emit a significant amount of CO_2. According to the German Federal Environmental Agency [50], this proportion reached nearly 18 % in Germany in 2014. For this reason, politics impose strict emission standards for vehicles. For example, the emission reduction target in 2015 for newly registered passenger cars in the European Union is 130 g CO_2 per km for the average fleet of a car manufacture [35]. This corresponds to a fuel consumption of 5.6 l per 100 km of petrol or 4.9 l per 100 km of diesel. These restrictions are going to be tightened in future. In 2021, the emission reduction target will be cut down to 95 g CO_2 / km.

Despite the need for environmentally friendly vehicles, alternative powertrain systems are still a niche. As stated by the German Kraftfahrtbundesamt [59], 127 000 passenger cars with hybrid or electric drive were registered in Germany in 2014. This is equal to a relative share of less than 0.3 % of all registered cars. Current forecasts predict [20] that combustion engines (including hybrid vehicles) will still have a market share of 90 % in 2030. This shows, gasoline and diesel engines are essential part of traffic and transportation for a foreseeable period. Therefore, motor efficiency and performance gains are necessary to fulfill future emission standards and reduce CO_2 emissions.

One way to achieve this goal is downsizing. Thereby, a smaller engine is used in combination with a turbocharger to compensate the loss of performance and increase efficiency. A schematic of a turbocharged engine is shown in Figure 1.1. The turbocharger consists of a centrifugal compressor and a radial inflow turbine. The compressor is placed upstream the engine and used to increase the mass of intake air in the engine combustion chamber. Thus, more fuel can be burned leading to a higher engine power. An intercooler is often used to cool down the compressed air and

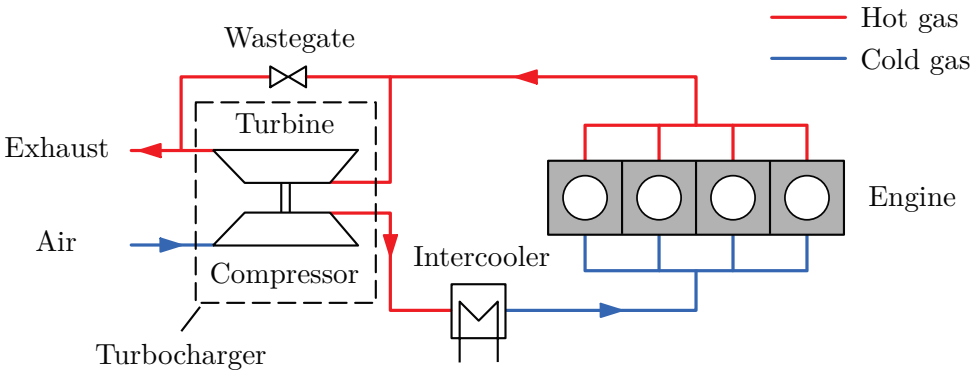

Figure 1.1: Schematics of a turbocharged engine (after Schreiner [88]).

increase the air density even further. The compressor is powered by a turbine, which recovers energy from the engine exhaust gases and converts it into mechanical power. Otherwise, this energy would be lost. In order to prevent the turbine from overheating, a wastegate is installed to limit the mass flow rate of exhaust gases going through the turbocharger. As a result, a smaller engine with the same performance as a naturally aspirated engine can be designed. This leads to increased efficiency, lower CO_2 emissions, and weight. According to a study of automotive supplier Honeywell [47], nearly every second car sold in 2020 will be equipped with a turbocharger. This corresponds to an increase in unit sales of 9 % per year. Thus, the turbocharger is an vital part of the drive train of modern passenger cars.

One essential component of a turbocharger is the centrifugal compressor. It typically consists of an inlet port, the compressor wheel and the volute with an exit pipe. The compressor wheel is well understood and studied thoroughly in recent decades. In contrast, the volute and its influence onto the compressor performance and efficiency are less investigated in scientific research. In particular, the number of publications regarding the numerical optimization of the volute housing is very low. However, a better understanding of the fluid flow inside the volute could lead to performance improvements of modern turbocharger and thus help to meet future emission standards.

As part of this study the centrifugal compressor of a turbocharger for light commercial vehicles and passenger cars has been simulated using computational fluid dynamics (CFD). For this reason, a new numerical model is developed utilizing a density-based solver with high accuracy at arbitrary Mach numbers. Different validation

cases are investigated to assess the accuracy of the CFD model. Furthermore, an automated geometry generation algorithm is written for the volute shape generation using B-splines. Based on the proposed numerical model and the automated geometry generation, a numerical optimization is performed with the following aims:

- improve the overall compressor efficiency
- obtain an optimal volute shape
- identify important geometric parameters for the volute performance.

This optimization of a volute shape is a novelty in the scientific field due to the complex numerical model, the large geometric freedom, and the huge number of investigated geometries. For this reason, it is an important part towards a better understanding of the flow inside a volute and the design of more efficient centrifugal compressor.

2 Centrifugal Compressor and Volute

The following chapter gives a short introduction of the flow in a centrifugal compressor and the design and working principle of the volute. Additionally, a literature overview is given about the influence of various geometric parameters onto the performance of the volute. Finally, optimization in turbomachinery application with focus on improvements in volute efficiency shows the potential of this thesis.

2.1 Centrifugal Compressor Principle

In a centrifugal compressor (also known as radial compressor), energy is transferred from a rotating compressor wheel to a working gas. This accelerates the fluid and increases its kinetic energy. Centrifugal compressors offer the advantage of higher pressure ratios at lower flow rates compared to axial compressors. They are commonly used in process industry, oil and gas industry, auxiliary power units, turbochargers, and gas turbines. The compressor consists of the following four major components: inlet, impeller, diffuser, and volute (see Figure 2.1).

Inlet The inlet to a centrifugal compressor is typically a simple pipe. However, it can also be ported extending the operational range of the compressor by shifting the surge line to lower mass flow rates. Furthermore, inlet guide vanes can be installed to pre-swirl the inflow.

Impeller A rotating set of blades gradually transfers energy onto the working gas. The gas enters the compressor in axial direction, gets accelerated and is expelled in radial direction. The impeller exit flow velocity can reach transonic speeds. The type of the compressor wheel is determined by the exit blade angle.

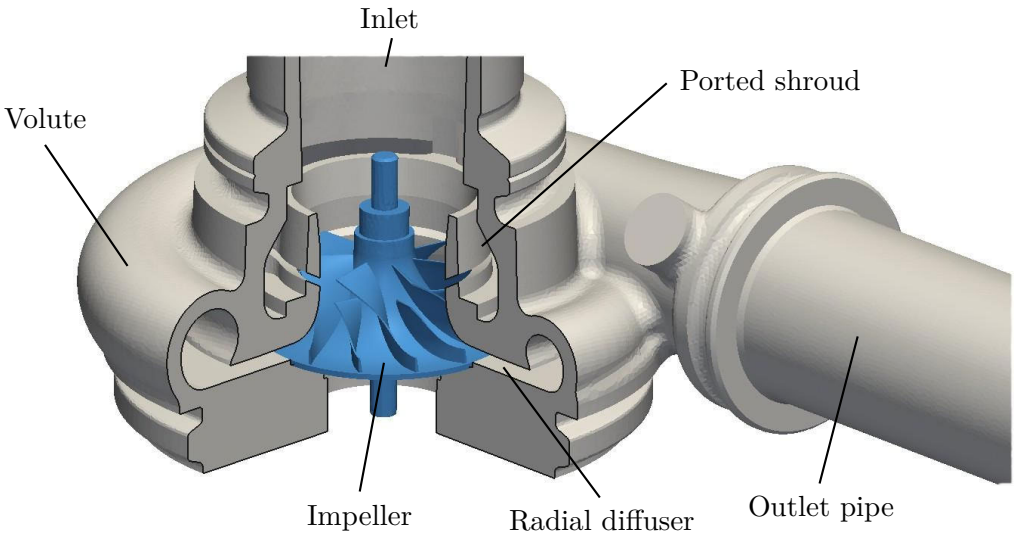

Figure 2.1: Main components of a centrifugal compressor in isometric view.

Radial diffuser The diffuser converts the kinetic energy of the working gas into potential energy (pressure). This is achieved by increasing the cross-sectional area and thus gradually reducing the flow velocity. Diffusers can be vaneless or vaned dependent on case of application.

Volute The volute collects the flow by redirecting it in circumferential direction and delivers it to the compressor outlet pipe. The flow velocity is further decreased in the flow channel and the static pressure is increased. The volute can take many different geometric shapes.

The idealized process for the compressor is an isentropic compression without heat exchange to the surroundings. This process can be characterized using two dimensionless quantities: total-to-total pressure ratio Π_{tt} and isentropic efficiency η_{is}. These are based on the assumption that the kinetic energy at the compressor outlet is useful energy (see Boyce [19]) and defined as following:

$$\Pi_{\mathrm{tt}} = \frac{p_{\mathrm{tot,out}}}{p_{\mathrm{tot,in}}} \,, \qquad \eta_{\mathrm{is}} = \frac{\Pi_{\mathrm{tt}}^{(\gamma-1)/\gamma} - 1}{\frac{T_{\mathrm{tot,out}}}{T_{\mathrm{tot,in}}} - 1} \,, \tag{2.1}$$

where p_{tot} is the total pressure and T_{tot} the total temperature at the compressor inlet (subscript: in) and outlet (subscript: out), respectively.

These total properties are defined as:

$$p_{\mathrm{tot}} = p\left(1 + \frac{\gamma - 1}{2}\mathrm{Ma}^2\right)^{\gamma/(\gamma-1)} , \qquad T_{\mathrm{tot}} = T\left(1 + \frac{\gamma - 1}{2}\mathrm{Ma}^2\right) , \tag{2.2}$$

with the isentropic exponent γ and the Mach number Ma defined as the ratio of flow velocity $\underline{u}$ to local speed of sound c:

$$\mathrm{Ma} = \frac{|\underline{u}|}{c} . \tag{2.3}$$

The compressor performance depends on the inlet conditions. Therefore, reference values have to be used to compare measurement data at different ambient conditions and the numerical results. The corrected mass flow rate $\dot{m}_{\mathrm{corr}}$ is formulated as follows:

$$\dot{m}_{\mathrm{corr}} = \dot{m}\frac{p_{\mathrm{ref}}}{p_{\mathrm{tot,in}}}\sqrt{\frac{T_{\mathrm{tot,in}}}{T_{\mathrm{ref}}}} , \tag{2.4}$$

based on the reference conditions:

$$p_{\mathrm{ref}} = 101\,325\,\mathrm{Pa} , \qquad T_{\mathrm{ref}} = 293.15\,\mathrm{K} . \tag{2.5}$$

The performance of the volute can be analyzed using the static pressure recovery C_p and total pressure loss coefficient K_p:

$$C_p = \frac{p_{\mathrm{out}} - p_{\mathrm{in}}}{p_{\mathrm{tot,in}} - p_{\mathrm{in}}} , \qquad K_p = \frac{p_{\mathrm{tot,in}} - p_{\mathrm{tot,out}}}{p_{\mathrm{tot,in}} - p_{\mathrm{in}}} \tag{2.6}$$

where in this case the inlet corresponds to the impeller exit and the outlet to the compressor outlet. The static pressure recovery coefficient assumes that kinetic energy at the volute outlet is lost and cannot be utilized. In contrast to that the total pressure loss coefficient defines the kinetic energy as useful. When applying this definition, the vaneless diffuser downstream the compressor wheel as well as the outlet pipe are included in the volute performance characteristics.

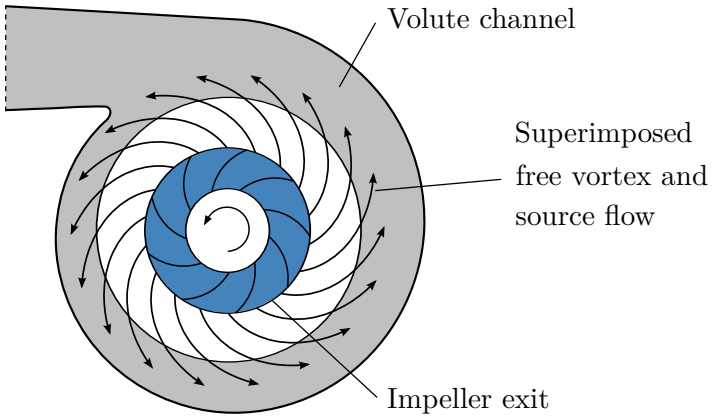

Figure 2.2: Flow pattern downstream the compressor wheel.

2.2 Volute Characteristics

The goal of the vaneless diffuser and the volute is to collect the flow, reduce flow speed and convert the kinetic energy into potential energy/static pressure. The pressure rise in the volute is in most cases equal to the pressure rise in the impeller. The volute itself does not take part in the energy transfer process onto the fluid. Therefore, all design considerations of the volute try to reduce the losses. Worster [108] states, the volute determines the point of best efficiency of pumps and compressors rather than the compressor wheel. This shows the importance of a careful design of this component of a turbomachine and the potential for improvements in this part of the compressor.

Design of a Volute

One common approach to design a volute is based on the conservation of mass and angular momentum of the flow (see Pfleiderer [83]). Under the assumption of no friction, the flow follows a path of a free vortex superimposed by a source flow downstream the impeller exit as shown in Figure 2.2. The shape of the volute should match this flow pattern. As the mass flow rate increases in streamwise direction inside the volute channel, the cross-sectional area A_{vc} of the volute must increase gradually to accommodate the fluid. The goal of the design is a uniform flow and constant static pressure at the volute inlet in circumferential direction. This is usually achieved at

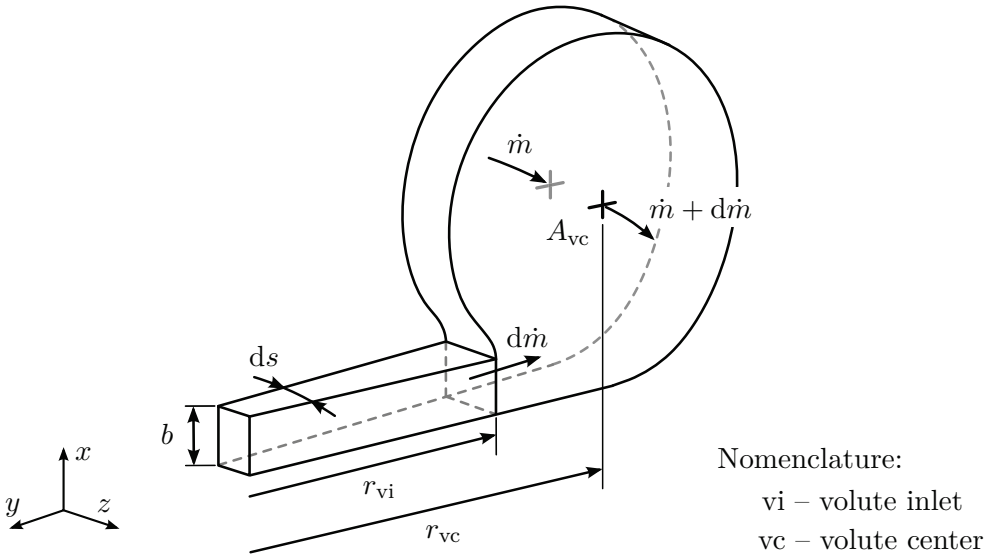

Figure 2.3: Definition of a finite cross section element of a volute (Mojaddam and Hajilouy-Benisi [77]).

design flow rate. At off-design conditions, the volute is either too large or too small. Therefore, pressure fluctuations develop circumferentially around the volute. These travel back to the impeller and reduce the compressor performance, decrease impeller flow stability and cause vibrations (see Eckert and Schnell [33]).

Figure 2.3 shows a finite cross section element of a volute including the vaneless diffuser, where b and $\mathrm{d}s$ denotes the height and the radian of the element, respectively. The volute inlet is marked with the subscript "vi" and the center of the volute cross section with "vc". The mass flow $\mathrm{d}\dot{m}$ entering the volute element is:

$$\mathrm{d}\dot{m} = \rho_{\mathrm{vi}} u_{\mathrm{vi,r}} b \mathrm{d}s \ , \tag{2.7}$$

with the density ρ_{vi} and radial velocity $u_{\mathrm{vi,r}}$ at volute inlet. The flow through the volute cross section is defined as:

$$\dot{m} = \int \rho u_\theta \mathrm{d}A_{\mathrm{vc}} \ , \tag{2.8}$$

with the velocity in circumferential direction u_θ and the cross sectional area of the volute A_{vc}. Using the assumption of constant density and velocity in the volute

element, this can be simplified to:

$$\dot{m} = \rho_{\mathrm{vc}} u_{\mathrm{vc},\theta} A_{\mathrm{vc}} \ . \tag{2.9}$$

Combining Equation (2.7) and (2.9) results in:

$$\mathrm{d}(u_{\mathrm{vc},\theta} A_{\mathrm{vc}}) = u_{\mathrm{vi,r}} r_{\mathrm{vi}} b \mathrm{d}\theta \ . \tag{2.10}$$

This is based on neglecting the density variation between the volute inlet and the volute element and expressing the radian as $\mathrm{d}s = r_{\mathrm{vi}}\mathrm{d}\theta$ with the circumferential angle θ. It is possible to calculate the geometric parameters such as A_{vc} if the circumferential velocity is known. This velocity component can be estimated based on a free vortex model:

$$r_{\mathrm{vc}} u_{\mathrm{vc},\theta} = r_{\mathrm{vi}} u_{\mathrm{vi},\theta} \ . \tag{2.11}$$

Substituting this expression in Equation (2.10) and integrating both sides leads to:

$$\frac{A_{\mathrm{vc}}}{r_{\mathrm{vc}}} = \frac{u_{\mathrm{vi,r}}}{u_{\mathrm{vi},\theta}} b\theta \ . \tag{2.12}$$

At each circumferential angle θ the geometric property $A_{\mathrm{vc}}/r_{\mathrm{vc}}$ can be calculated. Therefore, the geometric size of the volute channel is set. However, the actual shape is not defined. This allows for a wide range of different designs with a strong influence on the flow inside the volute and the overall performance of the centrifugal compressor.

Flow inside a Volute Channel

The flow field inside a volute was studied in detail by Ayder et al. [5–7]. It strongly depends on the vortex formation in the volute channel. Two different vortex patterns can be distinguished: Forced vortex, and free vortex flow. The former is characterized by an increase of tangential velocity with increasing radius, while the latter is defined by an inverse proportional tangential flow velocity with respect to the radius. Fluid close to the tongue at a small radius starts swirling around the center of the volute cross section. This results in large velocity gradients, shear stresses, and losses. The kinetic energy at the volute center is rapidly dissipated until a forced vortex is developed.

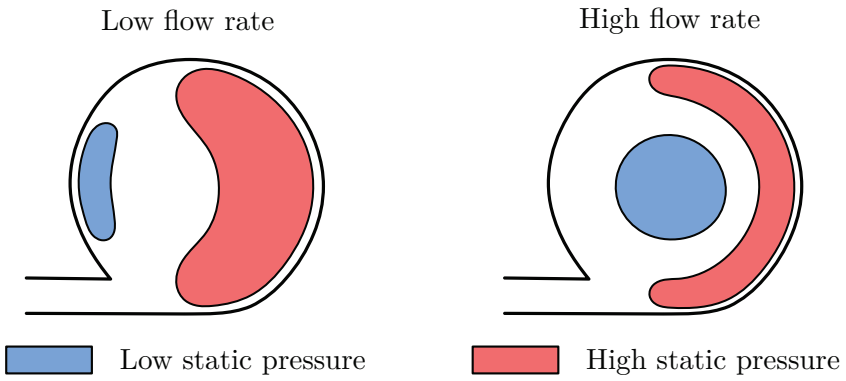

Figure 2.4: Characteristic static pressure distribution inside a volute channel for low and high flow rates.

Hence, a drop of total pressure is observed in the center of the volute channel. The flow pattern further downstream depends on the operating point.

At **lower flow rates**, there is only reduced swirl in the volute channel because of small radial flow velocities at the volute inlet. As a result, a forced vortex is formed due to internal shear stresses in the center of the volute cross section. Its extension increases gradually to cover the complete volute cross section further downstream. This leads to a more uniform distribution of total pressure with a minimum in the center due to energy dissipation. Centrifugal forces are weak at low flow rates. Thus, the static pressure at the inner volute wall is decreased due to higher flow velocities following from the conservation of angular momentum in the volute cross-section (see Figure 2.4 left).

At **high flow rates**, as the fluid moves downstream through the volute channel, it is wrapped around by fluid entering through the volute inlet creating a forced vortex. For this reason, the flow field and the total pressure distribution results from the volute inlet flow velocity distribution and the way the volute is filled, not from energy dissipation in the center of the volute cross section. Low energy fluid is accumulated in the center of the vortex resulting in a decrease of total pressure from the walls towards the center. The static pressure distribution is mainly affected by strong swirl velocities resulting in low static pressure in the center of the volute cross-section as shown in Figure 2.4 (right). Internal shear stresses in a forced vortex are zero. Consequently, only friction on the volute walls or an increase in radius at the exit diffuser could lead to an decrease of swirl in the volute.

Secondary vortices in the volute channel are mainly caused by radial pressure gradients and often occur in corners of the geometry. When low energy fluid in the boundary layer is subject to a radial pressure gradient, it can no longer follow the main swirl direction, but turns back towards the lower pressure.

2.3 Geometry Parameters on the Volute Flow

Investigations of different volute geometry parameters were performed as early as the 1940s. However, experimental investigations of different volute geometry configurations are limited due to production costs and time. In recent years, more research work has been performed regarding the design and optimization of compressors, fans and pumps using numerical flow simulations. This is due to the increasing computing power. Furthermore, designs can be tested virtually and no production costs arise. Nonetheless, the total number of investigations in open literature concerning the volute geometry is small.

The efficiency losses inside a volute are comparable to those inside the compressor wheel. According to Ayder et al. [7], the overall performance of a volute is mainly determined by five geometry specifications:

- shape of the cross section
- area of the cross section
- radial location of the cross section
- location of the volute inlet
- tongue geometry.

The investigation of the individual parameters is not always possible since some depend on each other. The influence of these parameters onto the compressor performance is given in the following sections. The overview of literature used is shown in Table 2.1. It contains often cited experimental and numerical investigations of volutes in pumps and compressors from recent decades. The total number of research work about the volute is limited, though.

Table 2.1: Summary of publications regarding different volute geometry parameters.

Year	Authors	Turbomachine	Investigation
Cross-sectional volute shape			
1948	Brown and Bradshaw [21]	Compressor	Experiment
1978	Mishina and Gyobu [74]	Compressor	Experiment
2000	Reunanen [85]	Compressor	Both
2011	Yang et al. [110]	Pump	Simulation
2012	Kim et al. [56]	Pump	Simulation
2012	Mojaddam et al. [76]	Compressor	Simulation
2013	Abdelmadjid et al. [1]	Compressor	Simulation
2015	Chen et al. [24]	Compressor	Simulation
Area of cross-section			
1948	Brown and Bradshaw [21]	Compressor	Experiment
1978	Mishina and Gyobu [74]	Compressor	Experiment
1948	Bowerman and Acosta [18]	Pump	Experiment
2011	Yang et al. [110]	Pump	Simulation
2012	Kim et al. [56]	Pump	Simulation
2014	Mojaddam et al. [77]	Compressor	Simulation
Radial location of cross section			
1972	Stiefel [93]	Compressor	Experiment
1978	Mishina and Gyobu [74]	Compressor	Experiment
Location of volute inlet			
1944	Lendorff and Meienberg [63]	Compressor	Experiment
1975	Hübl [49]	Compressor	Experiment
2007	Hassan [42]	Compressor	Experiment
2013	Abdelmadjid et al. [1]	Compressor	Simulation
2015	Chen et al. [24]	Compressor	Simulation
Tongue of the volute			
1979	Lipski [66]	Pump	Experiment
1997	Dong et al. [31]	Pump	Experiment
2005	Xu and Müller [109]	Compressor	Experiment
2011	Mohtar et al. [75]	Compressor	Experiment
2014	Mojaddam et al. [77]	Compressor	Simulation

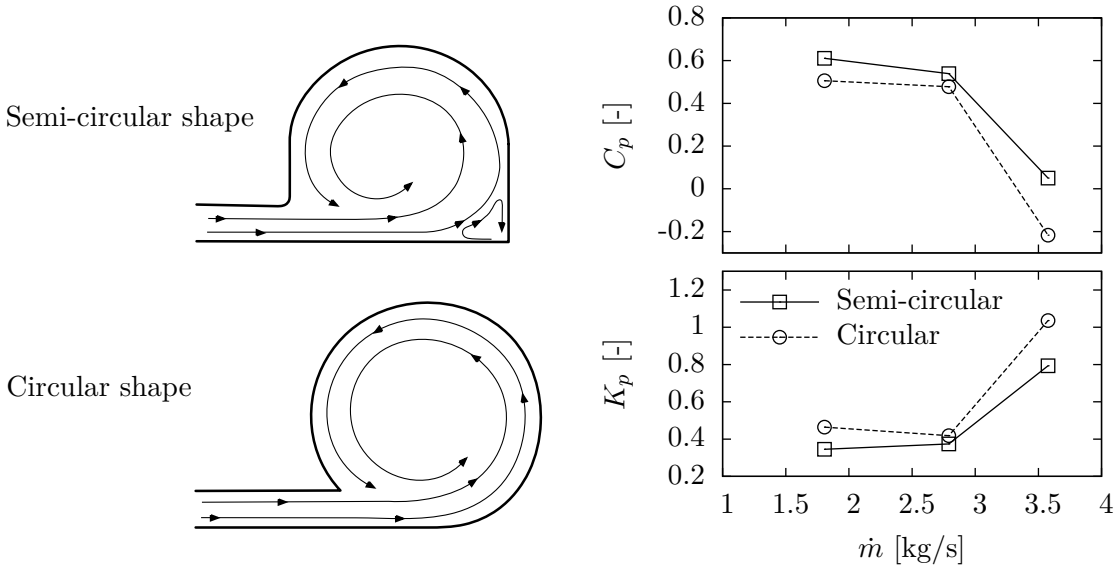

Figure 2.5: Volute cross section shapes (left) investigated by Reunanen et al. [85] and static pressure recovery coefficient C_p (right, top) and total pressure loss coefficient K_p (right, bottom) as a function of the mass flow rate.

2.3.1 Shape of the Cross Section

Brown and Bradshaw [21] used a centrifugal compressor with a vaneless diffuser to investigate five different cross-sectional volute shapes. The impeller outlet diameter is 286 mm at a design speed of 14 273 min^{-1}. The goal was a constant circumferential pressure distribution at design point. The different cross section geometries are horseshoe-shaped with different opening angles and symmetrical and tangential volute inlet. As a result, the authors claim a negligible influence of the shape on the performance of the compressor.

Mishina and Gyobu [74] tested seven different volute geometries using a compressor wheel with an trailing edge diameter of 250 mm at a rotational speed of 23 560 min^{-1}. The investigations show that circular-shaped volute geometries perform better compared to rectangular-shaped ones due to secondary vortices in the corners. Furthermore, an oversized cross section area does reduce the losses inside the volute. The effect of the shape onto the performance is reported to be less than 5 %.

Reunanen [85] experimentally and numerically investigated two different volutes: a semi-circular and a circular cross section shape with tangential inlet location and

the same cross-sectional area (see Figure 2.5). He measured the influence onto the performance of a compressor with impeller exit diameter of 618 mm. His results show that the shape of the volute has minor effect on the overall performance of the compressor. Despite the development of a secondary vortex in the rectangular bottom corner of the semi-circular volute, the circular one has a higher pressure loss and lower static pressure recovery. Reunanen states that a non-optimal tongue design is the reason for the differences. As a conclusion, the volute cross-sectional area, its circumferential variation and the tongue design are identified as more important factors compared to the cross-sectional volute shape.

Yang et al. [110] simulated a centrifugal pump with a impeller exit diameter of 280 mm at a design speed of 3000 min^{-1}. The investigated symmetrical volute shapes are circular, horseshoe shaped, trapezoid and rectangular. The results reveal that the circular design offered the best performance. At the same time, trapezoid and rectangular shapes yield similar characteristics. The differences between best and worst shape are about 2 % for efficiency and 3 % for pressure rise.

Kim et al. [56] performed numerical investigations of the impeller and volute of a centrifugal pump with a rotational speed of 600 min^{-1} and an exit diameter of 550 mm. The investigation was based on Stepanoffs assumption [92] to maintain a constant velocity in each cross section area. A circular and a bulb shaped volute with symmetrical inlet were analyzed. The results show a negligible impact of the volute shape.

A centrifugal compressor was investigated by Mojaddam et al. [76]. It had a rotor exit diameter of 76.2 mm with a design speed of 50 000 min^{-1} and a maximum isentropic efficiency of about 73 %. Three different cases for the volute cross section shape were defined using an ellipsoid shape with different length-to-height ratios. The shape with the largest height and the lowest radial dimensions yields an increased efficiency of up to 15 % compared to the baseline model with a circular shape.

Similar results were found by Abdelmadjid et al. [1]. They simulated a compressor with three different volute geometries: a circular cross section with tangential and symmetrical inlet location, and a semi-circular cross section with tangential inlet location (see Figure 2.6). The compressor wheel had an outlet diameter of 80 mm at a design speed of 100 000 min^{-1}. As a result, the cross section shape mainly affects

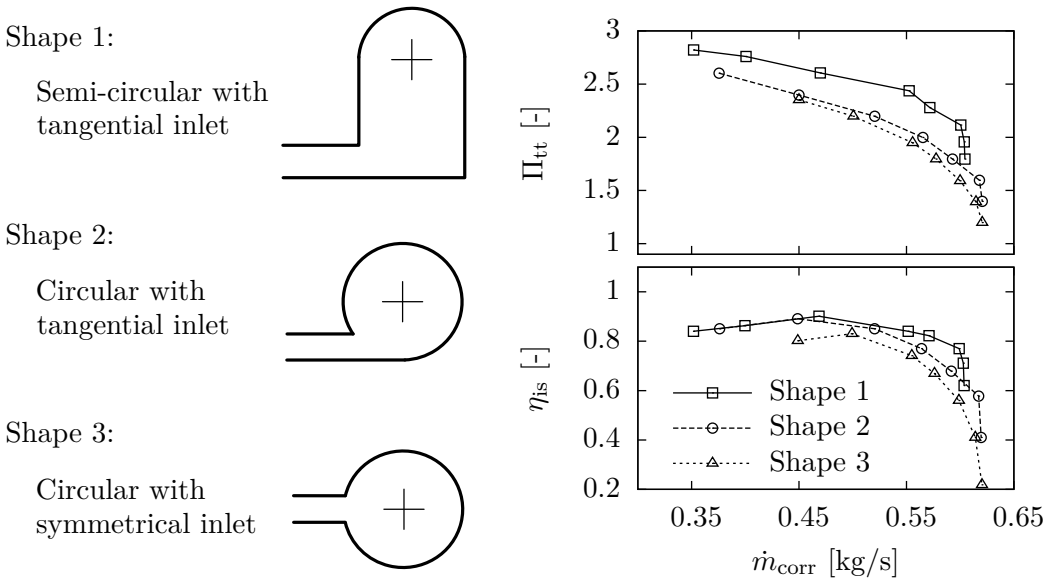

Figure 2.6: Different volute cross section shapes (left) and their total pressure ratio Π_{tt} (right, top) and isentropic efficiency η_{is} (right, bottom) as a function of the corrected mass flow rate $\dot{m}_{corr}$ according to Abdelmadjid et al. [1].

the operating range while the volute inlet location for the most part influences the peak efficiency. The rectangular semi-circular shape yields a significantly higher total pressure ratio as well as a better isentropic efficiency compared to the other geometries. Differences between the best and worst shape are up to 15 %. Unfortunately, no explanation is given for the advantageous results of a semi-circular volute shape.

Circular, rectangular and trapezoidal volute shapes with tangential and symmetrical inlets were investigated by Chen et al. [24]. They used a centrifugal compressor with a outlet impeller diameter of 122 mm. The results show, a circular volute shape offers a significantly lower total pressure loss compared to the other shapes. Chen argues that more homogeneous velocity profiles inside a circular volute lead to reduced shear stress losses. Unfortunately, the cross-sectional area distribution of the volute channel were not equal. This reduces comparability and introduces uncertainty of the results.

This literature overview shows the potential of compressor efficiency gains based on shape improvements. In particular, circular and semi-circular shaped volutes with tangential inlet offer a superior performance. Unfortunately, there is no comprehensive comparison of a large number of shapes. Investigations are often limited to a small number of different models.

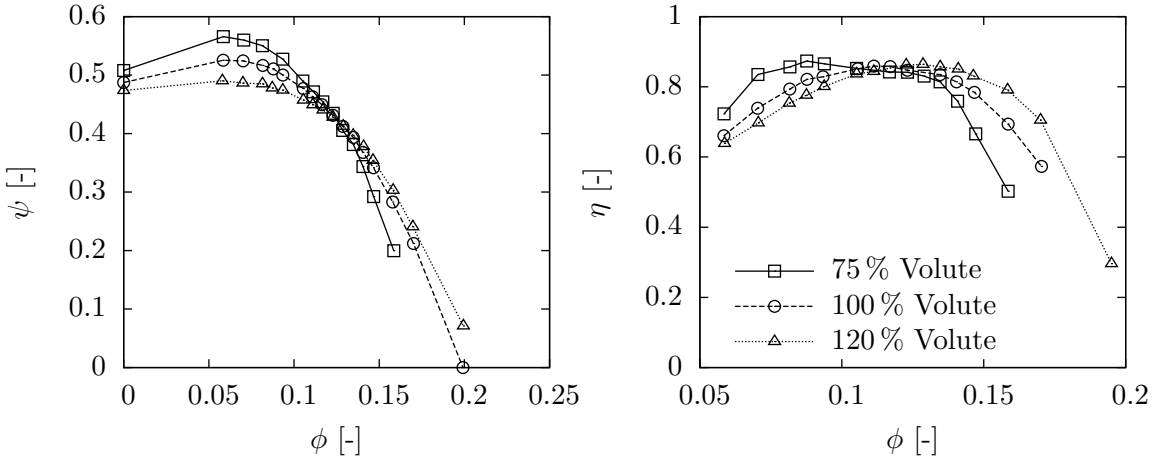

Figure 2.7: Pressure rise coefficient ψ (left) and efficiency η (right) as function of the flow coefficient ϕ for three different volute sizes according to Bowerman and Acosta [18].

2.3.2 Area of the Cross Section

The cross-sectional area greatly influences the performance of the compressor. Bowerman and Acosta [18] carried out an experimental study on three different volute sizes for a pump. The cross-sectional area was varied based on 75 %, 100 %, and 120 % of the design for the nominal flow of the impeller. The volute had a rectangular shape and the outer wall was relocated to increase the size. This way, the shape of the volute is constant and does not influence the investigations. Figure 2.7 shows both the pressure rise coefficient ψ and efficiency η as function of the flow coefficient ϕ defined as:

$$\psi = \frac{h_{\mathrm{tot}} g}{u_{\theta,2}^2} \ , \qquad \eta = \phi\psi \frac{\rho A_2 u_{\theta,2}^2 r_2}{|\underline{M}|} \ , \qquad \phi = \frac{\dot{V}}{A_2 u_{\theta,2}} \ , \tag{2.13}$$

with the total head of the pump h_{tot}, the gravitational acceleration g, the circumferential velocity $u_{\theta,2}$ and cross-sectional area A_2 and radius r_2 at impeller exit, the volumetric flow rate $\dot{V}$, and the torque $\underline{M}$. The results reveal that a larger volute cross-sectional area significantly decreases the maximum pressure rise coefficient at low flow rates but increases the maximum flow coefficient of the machine. At the same time, the maximum efficiency is reduced slightly and shifted to higher flow rates. Kim et al. [56] got similar results using numerical simulations of a centrifugal pump.

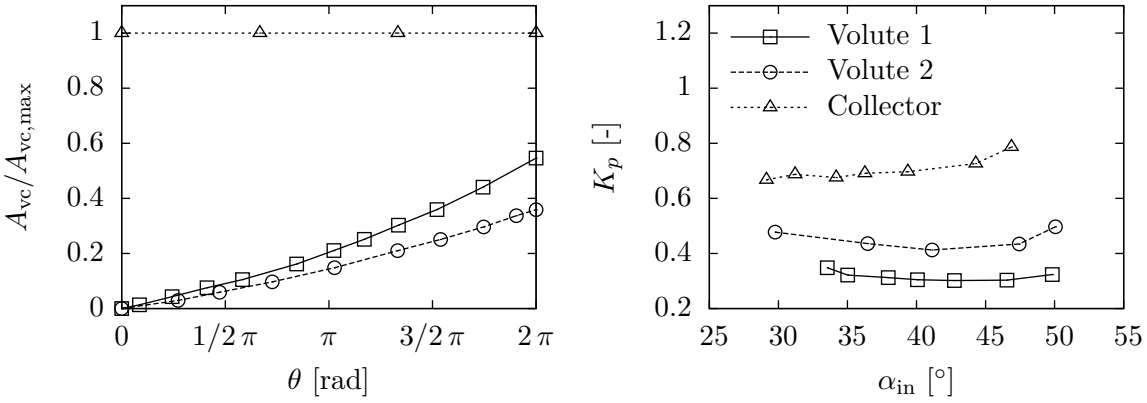

Figure 2.8: Relative circumferential area distribution of two different volutes and a collector (left) and their total pressure loss coefficient K_p (right) as a function of the inlet flow angle α_{in} (Mishina and Gyobu [74]).

These findings are in line with investigations of Yang et al. [110]. They investigated the influence of the volute cross-sectional area onto the pressure rise and efficiency of a centrifugal pump. The volute had a circular cross-sectional shape and the area was set to 100 %, 112 %, 129 %, and 150 % compared to the baseline model. The pressure rise shows similar characteristics compared to Bowerman and Acosta and the maximum efficiency decreases for rising volute area by up to 2 %. Furthermore, the efficiency maximum is shifted to higher flow rates and the operating range is extended.

Mishina and Gyobu [74] investigated the performance of a single-stage centrifugal compressor. The experiments included parameter studies of the cross-sectional shape, the radial position and area. The latter included two circular-shaped volute geometries where volute 1 offers a smaller volute outlet area A_{vc} at $\theta = 2\,\pi$ compared to volute 2 as shown in Figure 2.8 (left). Additionally, a collector with a very large constant area is used as reference. An increase in cross-sectional area of the volute channel leads to reduced total losses (see Figure 2.8, right). The reason is the lower flow velocity and therefore less shear stress losses. However, this is in contrast to using a collector, which offers the highest flow losses. This is due to excessive dissipation of momentum when the fluid enters the large collector. Unfortunately, no influence onto the overall performance of the compressor is presented.

Similar results were reported by Brown and Bradshaw [21]. Substituting a volute with a collector resulted in a drop in adiabatic efficiency between (3 – 12) % and a

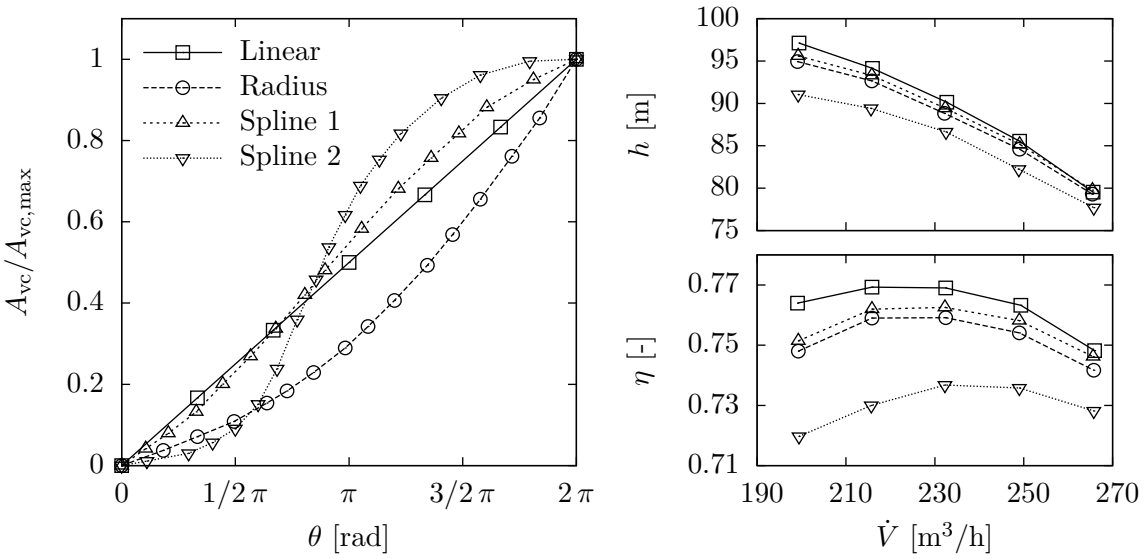

Figure 2.9: Different circumferential area distributions of the volute (left), and head h (right, top), and efficiency η (right, bottom) of the centrifugal compressor as a function of the flow rate $\dot{V}$ after Yang et al. [110].

shortened operating range. Hagelstein et al. [40] states, a collecting chamber with constant area results in pressure distortions travelling backwards into the vaneless diffuser and the impeller. In contrast, a volute with increasing area does produce a uniform pressure distribution at design conditions. However, pressure distortions at off-design can be of the same magnitude as the collector. In case of very small flow rates, the cross-section area of the volute is too large. Thus, the flow is decelerated at first increasing the static pressure followed by a sudden pressure drop at the tongue. At very high flow rates, the volute area is too small leading to a pressure decrease due to the acceleration of fluid in circumferential direction and a sudden pressure increase near the volute tongue.

Yang et al. [110] investigated four different area distributions A_{vc} as a function of the circumferential angle θ for a centrifugal pump: a linear distribution assuming constant swirl, a linear increase in radius of volute cross section center, and two S-shaped spline distributions (see Figure 2.9, left). All four cases offer the same maximum cross-sectional area $A_{vc,max}$ at the volute exit. The volute with a linear increase of area has the best pump head and efficiency as shown in Figure 2.9 (right). The worst performance is offered by the second spline. These findings are supported by the

results of Mojaddam and Hajilouy-Benisi [77]. A too small area at the beginning of the volute results in backflow and high flow velocities, which cause significant losses.

This section shows the importance of a correct design of the volute cross-sectional area for a given operating point. Furthermore, a simple linear increase of area in circumferential direction offers the best performance.

2.3.3 Radial Location of the Cross Section

The radial location of the volute channel has a large influence on the compressor performance. The investigations of Mishina and Gyobu [74] included the influence of the radial position of the volute. They concluded that a smaller centroid radius of the volute shape increases the losses of the volute. This can be attributed to the conservation of angular momentum. The tangential velocity in a swirling flow is inversely proportional to the radius. In case of an overhung volute, where the centroid radius may be smaller than the radial diffuser outlet, the tangential velocity in the volute channel can be higher compared to the diffuser. This way, the flow is first decelerated in the diffuser and then reaccelerated in the volute channel. According to Ayder et al. [7], this partly destroys the static pressure rise in the diffuser. Furthermore, the decreasing curvature radius of the inner wall favors flow separation.

Stiefel [93] carried out an experimental investigation of two volutes of a centrifugal compressor. Both volute geometries had a circular cross-sectional shape. However, the radial location was slightly different (see Figure 2.10). Stiefels results showed that a reduced centroid radius of the volute channel leads to an decrease of isentropic efficiency by 4 %. These results are often cited in literature. Unfortunately, the cross-sectional area of volute 1 is approximately 5 % larger compared to the second one. Therefore, the results are less conclusive.

The radial location of the volute cross section is barely investigated and publications in recent years are missing. Nevertheless, this parameter has a considerable influence on the performance of the volute. This shows the need for further investigations and the large potential for performance improvements.

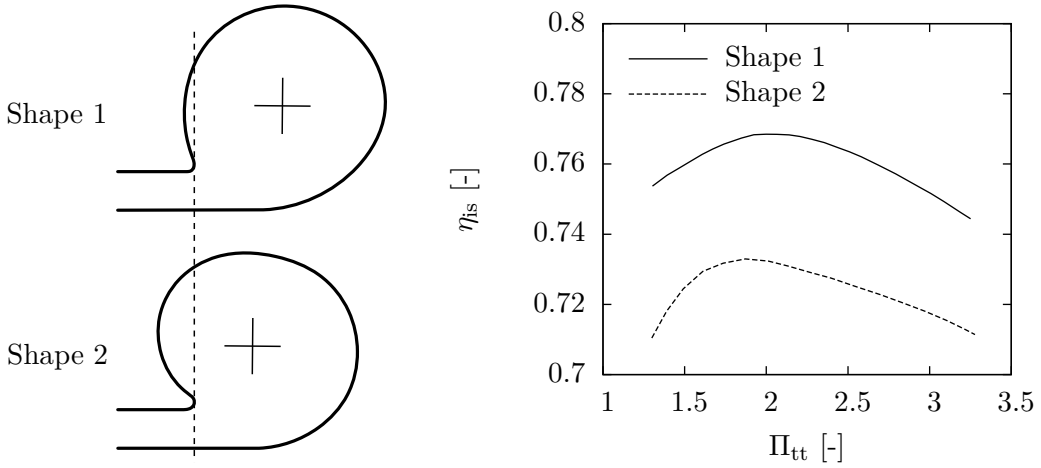

Figure 2.10: Influence of the radial position of the volute cross section onto the total pressure ratio Π_{tt} and the isentropic efficiency η_{is} by Stiefel [93].

2.3.4 Location of the Volute Inlet

First investigations about different volutes inlets were conducted by Lendorff and Meienberg [63]. They carried out a research study for two different volutes in a multi-stage centrifugal compressor. A circular shape with a symmetrical and a tangential inlet were used. The results showed that a tangential inlet yields a higher pressure rise and efficiency by up to 10 % throughout the complete operating range. However, the area of the cross-section was varied as well. Therefore, it is not clear if the improvement is a result of the volute inlet position alone. Hübl [49] achieved similar results using a single-stage centrifugal compressor (see Figure 2.11). Although the differences in specific work are only minor, the tangential inlet volute yields an improved efficiency by up to 2.5 %.

Hassan [42] experimentally analyzed the impact of different volute parameters onto the compressor performance. These parameters include volute area ratio and volute inlet location. The outcome of the work is that asymmetrical shapes offer a larger range of stable operations, higher-pressure coefficient, and mass flow rate compared to symmetrical shapes. These results are supported by the work of Abdelmadjid et al. [1], which comes to a similar conclusion (see Figure 2.6).

Chen et al. [24] argue that the reason for these differences can be found in the varying shear stress losses. Compared to the single vortex using a tangential inlet,

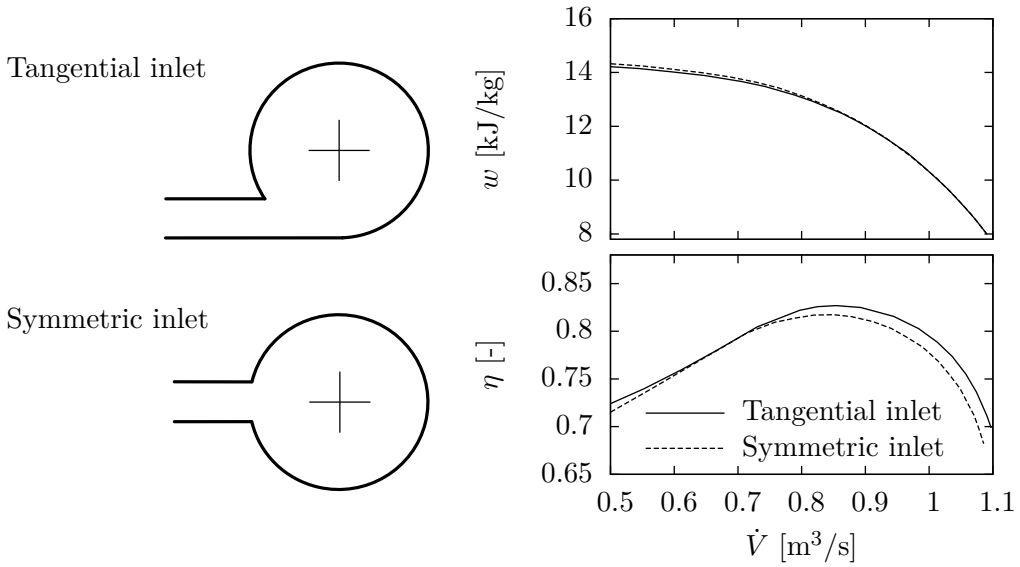

Figure 2.11: Two different volute inlet positions (left) and their influence onto the specific work (right, top) and the efficency (right, bottom) according to Hübl [49].

a symmetrical inlet produces a double vortex structure. This reduces the distance between the opposite flow directions and thus increases the radial velocity gradients close to the diffuser outlet. Both effects result in an increase of shear stress and therefore higher losses.

The presented publications show the superior performance of a tangential volute inlet compared to symmetrical ones. However, there are no investigations of other types, such as a slightly off-centered inlet. The question remains, whether there is a better inlet position, which has not been identified yet.

2.3.5 Tongue Geometry

The tongue geometry is mainly investigated in centrifugal pumps and fans due to the missing radial diffuser. In these cases, it strongly influences noise levels, see, e.g., Velarde-Suárez et al. [102] and Datong et al. [27]. In contrast to that centrifugal compressor comprise of a diffuser between the impeller and the tongue. Therefore, the effect of its geometry is less severe.

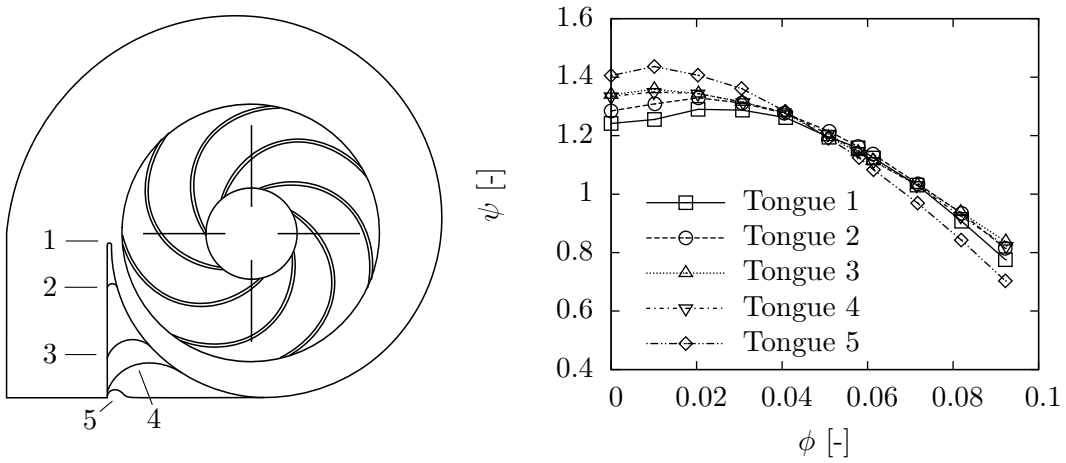

Figure 2.12: Five tongue shapes (left) and their effect onto the pressure coefficient ψ as a function of the flow coefficient ϕ of a centrifugal pump (Dong et al. [31]).

Lipski [66] analyzed a single stage centrifugal pump with adjustable tongue. He concluded, the pressure coefficient strongly depends on the length and angle of the tongue. A shorter tongue results in higher efficiency at off-design operating conditions, in particular at high flow rates. Furthermore, the force onto the tongue depends on the operating point and is zero at peak efficiency. Similar conclusions were drawn by Dong et al. [31]. They investigated a centrifugal pump with five different tongue geometries (see Figure 2.12). The results show that the pressure coefficient increases at high and low flow rates with shorter tongue. The design point is unchanged, though. Exception for this trend is tongue 5. At the same time, a decrease of noise is also reported due to the larger distance between impeller and tongue. These findings are in line with other research work, such as Worster [108].

Information about the tongue geometry in centrifugal compressors is more limited. Xu and Müller [109] showed that a round and short tongue provides an improved pressure coefficient at high flow rates. However, the best peak efficiency is gained using a sharp tongue. These results are in contrast to observations by Mohtar et al. [75]. They revealed a retracted and round volute tongue does increase the compression ratio at all flow rates, in particular at higher rotational speeds. Furthermore, the peak efficiency is increased and the surge line is not shifted. The authors explain this with a more uniform pressure distribution at the tongue and in circumferential direction which leads to a better performance.

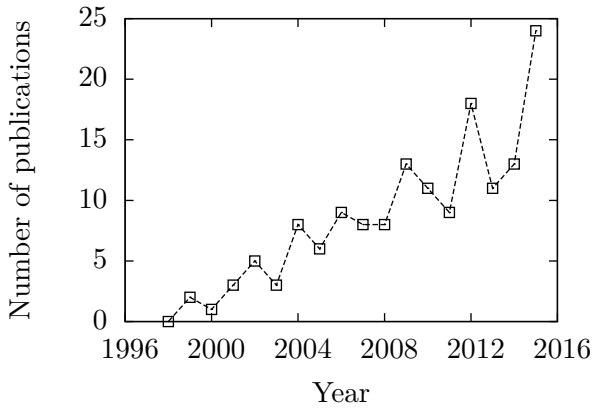

Part of compressor	Number of publications
Blades	126
Casing	12
Diffuser	9
Volute	3

Figure 2.13: Number of publications regarding the numerical optimization of compressors using CFD per year (left) and per compressor part (right) according to Scopus [34].

2.4 Optimization in Turbomachinery Application

Due to the increase in computational power, mathematical optimization is more and more utilized in the design process for turbomachinery application. Figure 2.13 (left) shows the number of publications per year listed in Scopus [34] dealing with optimization of compressors using CFD. Since the beginning of the last decade, the number of research work on this topic is steadily increasing. This is the result of the increasing demand for high performance turbo machines with better efficiencies and lower environmental impact. Due to the complexity of modern propulsion systems, these improvements cannot be achieved through investigation of a limited number of arbitrarily selected cases any more. For this reason, optimization based on mathematical models and numerical simulations has to be employed. Although the given overview consists of only Scopus cited publications, the trend is nevertheless noticeable and the total number of research work on this topic in both academia and industry is going to be significantly higher.

Despite an increase in CFD-based optimization, the vast amount of research work is unilaterally focused on the improvement of the compressor wheel and blade design (see Figure 2.13 right). According to Scopus [34], well above 80 % of the investigated publications are related to this part of the compressor. One reason is the much simpler geometry and mesh generation for the impeller. Blade geometries can be created

Table 2.2: Experimental results of reference and optimized volute of Baloni et al. [9].

Performance parameter	Reference volute	Optimized volute
Flow coefficient ϕ	0.245	0.266
Pressure coefficient ψ	0.69	0.74
Efficiency η	46.7 %	54.1 %

easily using specialized tools like ANSYS® BladeGen and ANSYS® TurboGrid. Furthermore, parametrization of the cross-sectional shape can be achieved using splines in combination with extrusion in pitchwise direction. This allows for fast geometry and mesh generation, which is essential for automatic optimization. Additionally, simplifications such as two-dimensional or rotationally symmetric simulations can be used. This reduces the mesh size and computational cost to quickly assess blade performance in axial and radial machines.

By contrast, only a small fraction of optimization work has been performed on the volute geometry, yet. The automated volute geometry generation and meshing is very difficult due to the complex shape. Furthermore, no geometrical simplifications can be made and the complete volute has to be simulated. This makes it more time consuming compared to blade or impeller investigations. For these reasons, the number of research work on the field of volute optimization is very sparse, restricted to simplified geometric variations, and only offers limited geometric freedom.

Baloni et al. [9] investigated the volute design using the analysis of variance (ANOVA) approach. The work is based on the numerical simulation of a centrifugal blower with an exit diameter of 425 mm and a design speed of 2900 min^{-1}. The flow coefficient and pressure coefficient of the reference model are 0.245 and 0.69, respectively. Three geometric parameters are defined as design variables: blower volute width, tongue angle, and radial position of the volute. The objective function is composed of the variation of static pressure at impeller outlet, losses inside the volute and total pressure at volute outlet. The simulations are performed using a steady-state approach. The numerically optimized geometry is validated using test bench measurements.

The improvements of the optimized volute geometry are shown in Table 2.2. The increase in efficiency is significant with about 7.4 %. However, the baseline efficiency

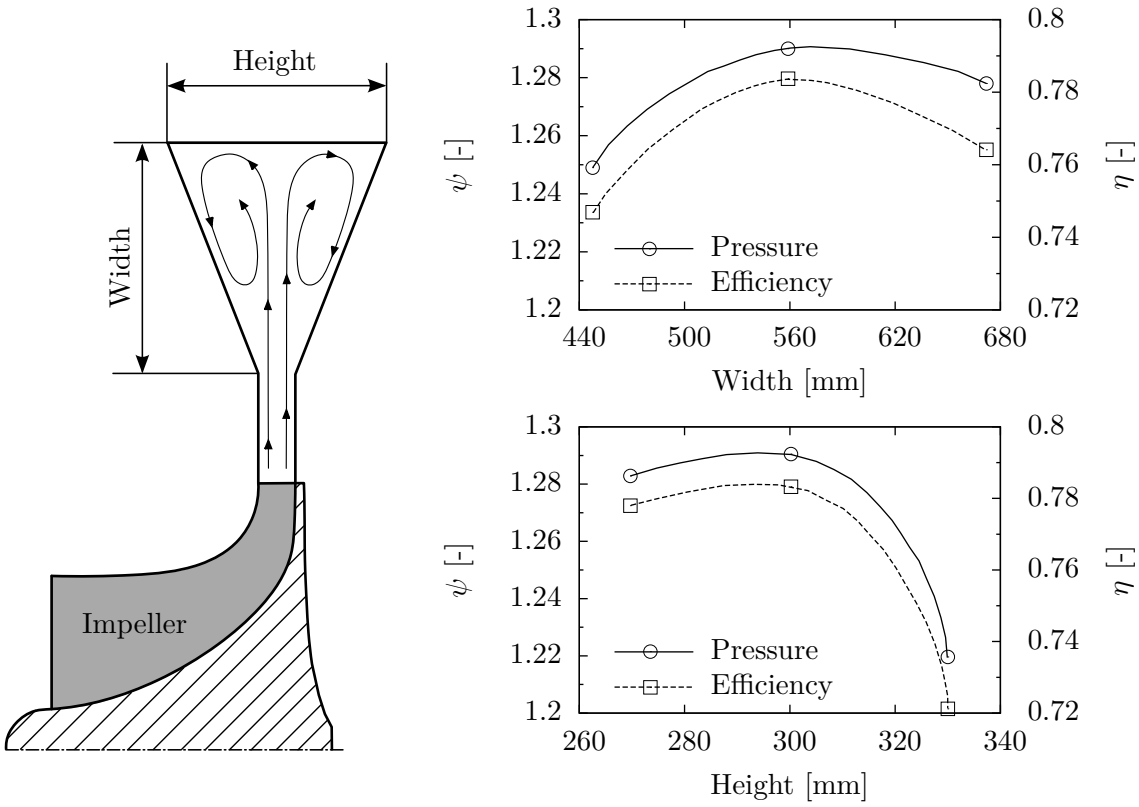

Figure 2.14: Volute cross section shape and geometric parameters (left) and blower performance for varying width at reference height of 300 mm (top right) and varying height at reference width of 560 mm (bottom right) according to Jang et al. [54].

is quite low with 46.7 %. Therefore, improvements are more feasible. The researchers suggest a blower width of 1.5 times the impeller width for an optimum performance. Furthermore, the tongue angle should be 26° for minimizing static pressure variations at the impeller outlet and 24° for reducing the total pressure at the volute outlet.

Jang et al. [54] numerically analyzed a centrifugal blower with a flow coefficient ϕ of 0.139, a pressure coefficient ψ of 1.29, and an efficiency η of 78.3 % at design point. The impeller has an exit diameter of 1625 mm at a design speed of 1780 min^{-1}. The volute has a trapezoidal shape with a symmetrical inlet (see Figure 2.14). The height and width are used as design parameters with reference values of 300 mm and 560 mm, respectively. The pressure rise and isentropic efficiency are defined as objective functions. The experimental points are determined using design of experiments (DOE)

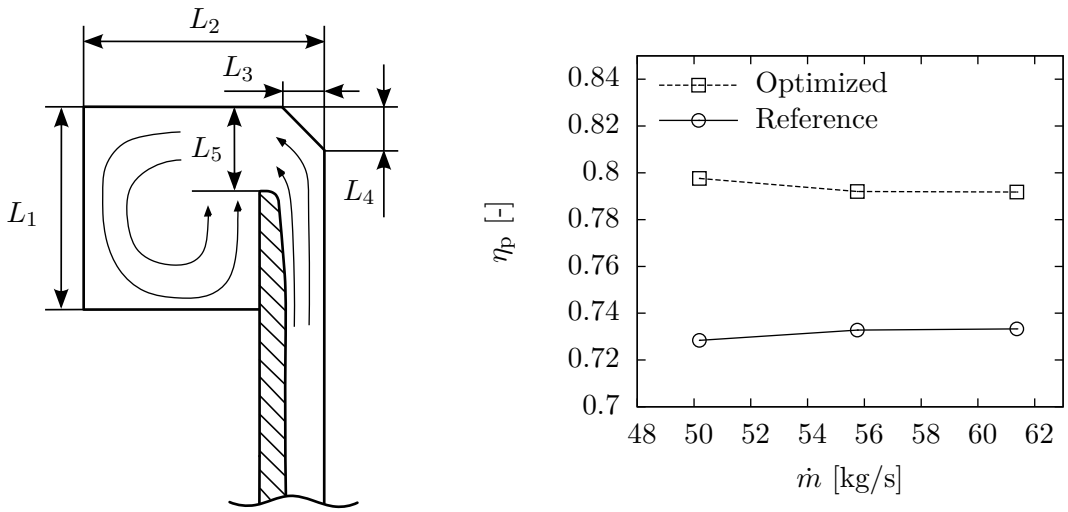

Figure 2.15: Five geometric parameters of volute shape (left) and polytropic efficiency η_p of the reference and optimized volute geometry (right) as a function of the mass flow rate $\dot{m}$ according to Huang et al. [48].

and the objective function in each point is evaluated using a steady-state simulation. The blower pressure coefficient and efficiency of the optimized model are increased by 1.6 % and 0.4 % respectively compared to the reference model. The total variation for different width and heights is approximately 6 % for the efficiency. The main reason for these differences are identified to be secondary flow in the corners.

Huang et al. [48] optimized a volute with rectangular cross-sectional shape for a centrifugal compressor. The volute shape consists of five different geometric parameters $L_{1...5}$ (see Figure 2.15, left). These were defined close to the volute inlet and outlet. Linear interpolation is employed for the shapes in between. In total, seven different design parameters are chosen. A constrained optimization using response surfaces is used for the improvement of the geometry. The objective function is to maximize the minimal value among the volute static pressure coefficient at three different flow rates: 90 %, 100 %, and 110 % of design flow rate.

The simulations are performed using a simplified model of the volute only. Thus, the inlet and compressor wheel are not modeled. The averaged volute inlet boundary conditions are taken from full-stage simulations of the complete compressor. Matlab is used for the optimization process with 35 initial variations. After 120 iteratons the optimization process converges. As a result, the efficiency of the volute is increased by

about 6 % (see Figure 2.15, right) and the total pressure loss coefficient is reduced by about 0.04. However, this leads just to a minor increase of polytropic stage efficiency of 0.4 %. The reason for this improvement are reported to be the corner cut-off at L_3 and L_4, which decreases losses due to secondary vortices.

2.5 Summary

This chapter discusses the basic working principle of a volute and the importance of its design with respect to the performance and operating range of a centrifugal compressor. Five different geometric specifications are identified and their influence onto the pressure ratio and efficiency are discussed in detail. However, several scientific issues remain open due to the limited number of publications:

- Is there a better volute inlet position compared to tangential and symmetrical?
- What is the best radial position of the volute channel?
- Which effect does the shape of the volute have onto the compressor performance?

This thesis tries to answer these problems by performing a numerical optimization of the volute channel of a centrifugal compressor. Despite the significance of the volute geometry, research work regarding the numerical optimization of this part of a centrifugal compressor is very limited. Furthermore, the conducted optimization studies are very limited in terms of geometric freedom of the volute. Therefore, there is large potential for performance and efficiency gains for the volute geometry in turbomachines using optimization in combination with computational fluid dynamics.

3 Numerical Model

The OpenFOAM version 2.4.0 [79] offers more than 80 solvers for different applications such as incompressible and compressible flow, heat transfer, multiphase flow and combustion. However, the open source CFD library is not widely used for thermal turbomachinery applications. One reason for this is the lack of a solver for a wide range of Mach number. For instance, the flow velocity in a turbocharger ranges from $\mathrm{Ma} \ll 1$ in the ported shroud up to $\mathrm{Ma} \approx 1$ at the impeller exit. A solver would have to resolve these different flow conditions.

Pressure-based compressible solvers included in OpenFOAM, such as `rhoSimpleFoam`, are based on the SIMPLE algorithm for the pressure-velocity coupling (Patankar [80]). They utilize the internal energy or enthalpy as variable for the energy equation, but do not include mechanical work $\nabla \cdot (\underline{\underline{\tau}} \cdot \underline{u})$. For this reason, these solvers cannot predicted losses correctly. Furthermore, the pressure-based approach does not allow accurate shock capturing in its current implementation. Therefore, it is not feasible for transonic and supersonic simulations.

On the other hand, one density-based solver is implemented in OpenFOAM called `rhoCentralFoam`. It is based on the central-upwind scheme of Kurganov et al. [60] and is capable of capturing discontinuities such as shocks as well as correctly predict losses due to the implementation of a total energy equation. However, it is solely a transient solver not designed for fast steady-state solutions. Additionally, the flux calculation scheme does not include preconditioning. Therefore, it is not suited for subsonic and incompressible simulations due to convergence difficulties. Finally, no method is implemented which allows transformation in a rotating frame of reference. Due to these drawbacks, this solver can also not be used for turbomachinery simulations.

Therefore, a new numerical model has to be developed and implemented which satisfies the following requirements: fast steady-state and transient simulations, accurate shock

capturing, correct prediction of losses, and suitable for all Mach numbers. The result is a density-based solver for turbomachinery applications, which features the simulation of steady-state as well as transient, turbulent, and compressible flow at arbitrary Mach numbers. The development of this model is presented in the following chapter.

3.1 Density-Based Solver

3.1.1 Governing Equations

The governing equations for the laminar flow of a Newtonian fluid in a rotating frame of reference with the angular velocity $\underline{\omega}$ is given as follows:

$$\frac{\partial}{\partial t}\iiint \underline{W}\mathrm{d}V + \iint [\underline{F}_{\mathrm{inv}} - \underline{F}_{\mathrm{vis}}] \cdot \mathrm{d}\underline{A} = \underline{S}\,, \tag{3.1}$$

with the conserved variables $\underline{W} = (\rho, \rho\underline{u}, \rho E)^T$ for an arbitrary control volume V and the differential surface area $\mathrm{d}\underline{A}$. The convective fluxes consist of a inviscid $\underline{F}_{\mathrm{inv}}$ and viscous part $\underline{F}_{\mathrm{vis}}$, respectively. These are defined as:

$$\underline{F}_{\mathrm{inv}} = \begin{Bmatrix} (\underline{u} - \underline{u}_{\mathrm{rot}})\rho \\ (\underline{u} - \underline{u}_{\mathrm{rot}})\underline{u}\rho + p\underline{n} \\ (\underline{u} - \underline{u}_{\mathrm{rot}})(\rho E + p) + p\underline{u}_{\mathrm{rot}}) \end{Bmatrix}, \qquad \underline{F}_{\mathrm{vis}} = \begin{Bmatrix} 0 \\ \underline{\underline{\tau}} \\ \underline{\underline{\tau}} \cdot \underline{u} - \underline{q} \end{Bmatrix}, \tag{3.2}$$

where ρ denotes the density, $\underline{u}$ the absolute fluid velocity, $\underline{u}_{\mathrm{rot}}$ the circumferential velocity, the face normal vector $\underline{n}$, and p the pressure. The specific total energy is calculated as:

$$E = e + \frac{1}{2}|\underline{u}|^2\,, \tag{3.3}$$

with the specific internal energy e. The viscous stress tensor is formulated as:

$$\underline{\underline{\tau}} = \mu\left[\nabla\underline{u} + (\nabla\underline{u})^T - \left(\frac{2}{3}\nabla\cdot\underline{u}\right)\underline{\underline{I}}\right]\,, \tag{3.4}$$

with the identity matrix $\underline{\underline{I}}$ and the dynamic viscosity μ.

The heat flux density $\underline{q}$ is defined by Fourier's law:

$$\underline{q} = -\lambda \nabla T \ , \tag{3.5}$$

with the temperature T and the thermal conductivity λ. The additional source term in the governing equation $\underline{S}$ are as following:

$$\underline{S} = \begin{pmatrix} 0 \\ -\rho \left(\underline{\omega} \times \underline{u} \right) \\ 0 \end{pmatrix} \ . \tag{3.6}$$

This term accounts for the Coriolis force. The circumferential velocity $\underline{u}_{\mathrm{rot}}$ and the relative velocity $\underline{u}_{\mathrm{rel}}$ in the rotating frame of reference are calculated as following:

$$\underline{u}_{\mathrm{rot}} = \underline{\omega} \times \underline{r} \ , \qquad \underline{u}_{\mathrm{rel}} = \underline{u} - \underline{u}_{\mathrm{rot}} \ , \tag{3.7}$$

with the angular velocity $\underline{\omega}$ and the radius $\underline{r}$ with respect to the axis of rotation. The fluid is considered as calorically perfect gas:

$$p = \rho R_i T \ , \qquad e = c_v T, \qquad \gamma = \frac{c_p}{c_v} \ , \qquad a = \frac{\mu}{\mathrm{Pr}\, \rho} \ , \tag{3.8}$$

with the specific heat capacity at constant pressure and volume, c_p and c_v, respectively, the specific gas constant for air $R_i = 287.06\,\mathrm{J/(kg\,K)}$, the ratio of specific heats γ, and the thermal diffusivity a. The dynamic viscosity is computed using Sutherland's law [95]:

$$\mu = \frac{C_1\, T^{3/2}}{T + C_2} \ , \tag{3.9}$$

with the constants

$$C_1 = 1.458 \cdot 10^{-6}\, \frac{\mathrm{kg}}{\mathrm{m\,s}\sqrt{\mathrm{K}}} \ , \qquad C_2 = 110.4\,\mathrm{K} \ . \tag{3.10}$$

The thermal conductivity λ is calculated using a constant Prandtl number for air $\mathrm{Pr} = 0.71$ at standard conditions as following:

$$\lambda = \frac{\mu c_p}{\mathrm{Pr}} \ . \tag{3.11}$$

3.1.2 Flux Calculation

The viscous fluxes $\underline{F}_{\text{vis}}$ are discretized using a linear second order discretization. However, second order central schemes cannot be used for the inviscid terms $\underline{F}_{\text{inv}}$. These methods would introduce spurious oscillations due to shocks or discontinuities at higher Mach numbers. Therefore, the inviscid fluxes are evaluated using the Simple Low-dissipation AUSM (SLAU) scheme introduced by Shima and Kitamura [57, 89]. This scheme features low dissipation at low speeds while keeping robustness and non-oscillating nature at high Mach number flows. It is based on the Advection Upstream Splitting Method (AUSM) by Liou and Steffen [65]. The formulation of the face fluxes is as following:

$$\underline{F}_{\text{inv}} = \frac{\dot{m} + |\dot{m}|}{2}\underline{\Psi}^{f+} + \frac{\dot{m} - |\dot{m}|}{2}\underline{\Psi}^{f-} + \tilde{p}\underline{N} \ , \tag{3.12}$$

based on the reconstruction of the primitive variables $(p, \underline{u}, T)^T$ on either side of the face with:

$$\underline{\Psi} = (1, \underline{u}, H)^T \ , \tag{3.13}$$

where $\underline{\Psi}^{f+}$ represents the reconstruction of the face variables from the owner cell P to the neighbor cell N and $\underline{\Psi}^{f-}$ from the neighbor cell to the owner cell. The additional variables are denoted as the face mass flux $\dot{m}$, the pressure flux $\tilde{p}$, the normal vector

$$\underline{N} = (0, \underline{n}, 0)^T \ , \tag{3.14}$$

and the total enthalpy H:

$$H = E + p/\rho \ . \tag{3.15}$$

Mass Flux

The face mass flux is defined as:

$$\dot{m} = \frac{1}{2}\left[\rho^{f+}\left(u_n^{f+} + |\bar{u}_n|^{f+}\right) + \rho^{f-}\left(u_n^{f-} + |\bar{u}_n|^{f-}\right) - \frac{\chi}{\bar{c}}\left(p^{f+} - p^{f-}\right)\right] \ , \tag{3.16}$$

with the speed of sound at the cell interface

$$\bar{c} = \frac{1}{2}\left(c^{f+} + c^{f-}\right) \ , \tag{3.17}$$

the relative velocity normal to the face $u_n^{f\pm} = (\underline{u}^{f\pm} - \underline{u}_{\mathrm{rot}}) \cdot \underline{n}$, the weighted face normal velocity

$$|\bar{u}_n|^{f\pm} = (1-g)|\bar{u}_n| + g\,|u_n^{f\pm}| \ , \tag{3.18}$$

the density-averaged face normal velocity

$$|\bar{u}_n| = \frac{\rho^{f+}|u_n^{f+}| + \rho^{f-}|u_n^{f-}|}{\rho^{f+} + \rho^{f-}} \ , \tag{3.19}$$

and the blending function

$$g = -\max(\min(\mathrm{Ma}^{f+}, 0), -1) \cdot \min(\max(\mathrm{Ma}^{f-}, 0), 1) \ . \tag{3.20}$$

The function χ is calculated as following:

$$\chi = \left(1 - \widehat{\mathrm{Ma}}\right)^2 \ , \tag{3.21}$$

with

$$\widehat{\mathrm{Ma}} = \min\left(1, \frac{1}{\bar{c}}\sqrt{\frac{|u_n^{f+}|^2 + |u_n^{f-}|^2}{2}}\right) \ . \tag{3.22}$$

Pressure Flux

The pressure flux is based on the SLAU scheme from Kitamura and Shima [57]

$$\begin{aligned}\tilde{p} = {} & \frac{p^{f+} + p^{f-}}{2} + \frac{\zeta^{f+} - \zeta^{f-}}{2}(p^{f+} - p^{f-}) \\ & + \frac{1}{2}\sqrt{\frac{|u_n^{f+}|^2 + |u_n^{f-}|^2}{2}}\left(\zeta^{f+} + \zeta^{f-} - 1\right)\left(\rho^{f+} + \rho^{f-}\right)\bar{c} \ ,\end{aligned} \tag{3.23}$$

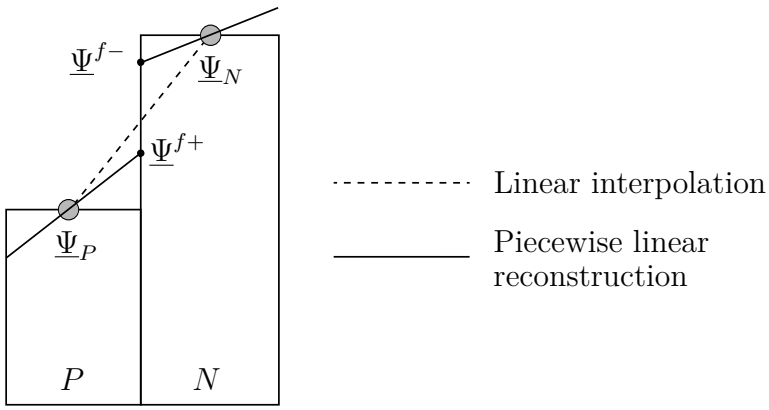

Figure 3.1: Piecewise linear reconstruction of face values between node P and N.

with the function

$$\zeta^{f\pm} = \begin{cases} \frac{1}{2}\left(1 \pm \operatorname{sgn}\left(\mathrm{Ma}^{f\pm}\right)\right) , & \text{if } |\mathrm{Ma}^{f\pm}| \geq 1 \\ \frac{1}{4}\left(\mathrm{Ma}^{f\pm} \pm 1\right)^2 \left(2 \mp \mathrm{Ma}^{f\pm}\right) , & \text{otherwise} \end{cases} . \tag{3.24}$$

The signum function has to be used for the interfacial Mach number in $\zeta^{f\pm}$ since is calculated based on the relative velocity normal to the face $u_n^{f\pm}$, which can be negative:

$$\mathrm{Ma}^{f\pm} = \frac{u_n^{f\pm}}{\bar{c}} . \tag{3.25}$$

The SLAU scheme does not need a freestream Mach number or cutoff Mach number compared to other flux calculation schemes, such as AUSM$^+$-up by Liou [64]. This is advantageous in cases with a highly nonuniform flow field or a wide range of Mach numbers, such as turbomachinery applications.

Variable Reconstruction

In order to provide second order spatial accuracy, monotonic piecewise linear slopes are used for the reconstruction of the cell to the face values (see Figure 3.1). The slope limiters with total variation diminishing (TVD) property have to be used for compressible flows. TVD schemes were introduced by Harten [41] and suppress unphysical oscillations and maintain monotonicity. They blend between first order and second order accuracy depending on local gradients of the flow field. The primitive

variables are reconstructed from the cell centers to the face centers. This results in two face values depending on which is the owner P and neighbor cell N:

$$\underline{\Psi}^{f+} = \underline{\Psi}_P + \frac{1}{2}\phi(r)\left(\underline{\Psi}_N - \underline{\Psi}_P\right) \ , \tag{3.26}$$

$$\underline{\Psi}^{f-} = \underline{\Psi}_N + \frac{1}{2}\phi(r)\left(\underline{\Psi}_P - \underline{\Psi}_N\right) \ , \tag{3.27}$$

with the slope limiter $\phi(r)$. This function is defined as following for the symmetric van Leer [62] limiter:

$$\phi(r) = \frac{r + |r|}{1 + r} \ , \tag{3.28}$$

where r is the ratio of successive gradients. For example, in case of $\underline{\Psi}^{f+}$, r is calculated from the variables of cell P to cell N

$$r = 2\frac{(\underline{x}_N - \underline{x}_P) \cdot \nabla\underline{\Psi}_P}{\underline{\Psi}_N - \underline{\Psi}_P} - 1 \ , \tag{3.29}$$

with the cell center coordinates $\underline{x}$. The gradient $\nabla\underline{\Psi}_P$ is calculated using the central differencing scheme at point P. A value of $\phi = 0$ corresponds to an first order upwind and $\phi = 1$ to a second order linear interpolation.

Implicit Residual Smoothing

The stability range of the time-stepping scheme can be improved by implicitly smoothing the residuals $\underline{R}$. This method was introduced by Jameson et al. [52, 53] for solving the steady-state Euler equations. The residuals represent the discrete approximation of the convective fluxes and the source terms:

$$\underline{R} = \iint [\underline{F}_{\text{inv}} - \underline{F}_{\text{vis}}] \cdot \mathrm{d}\underline{A} - \underline{S} \ . \tag{3.30}$$

They tend toward zero for a converged time-independent solution. The original residuals are replaced by the smoothed residuals $\bar{\underline{R}}$ by solving the implicit equation

$$\bar{\underline{R}} = \underline{R} + \epsilon\nabla^2\bar{\underline{R}} \ , \tag{3.31}$$

with the smoothing coefficient ϵ and the Laplacian smoothing operator ∇^2. The following form of implicit residual smoothing is implemented for unstructured grids according to Mavriplis et al. [69]:

$$\underline{\bar{R}}_i^m = \frac{\underline{R}_i + \sum \epsilon_j \underline{\bar{R}}_j^{m-1}}{1 + \sum \epsilon_j} \ , \tag{3.32}$$

with the cell index i, the sum over the neighboring cells j, the smoothing iteration m, and the unsmoothed initial residual $\underline{R}_i$. The smoothing coefficient ϵ is set to 0.5, which allows to double the time step. The iteration process is stopped, when the relative error of the residuals is less than 1 % or the maximum number of iterations is reached.

3.1.3 Preconditioning

Density-based algorithms, such as presented in the previous section, suffer from convergence difficulties at low Mach numbers. When the magnitude of the flow velocity becomes small in comparison to the acoustic speed, the convective terms of the time-dependent equations become stiff and the convergence rate is very slow [25].

For this reason, flux-preconditioning is employed to be able to simulate a wide range of Mach numbers including low Reynolds number flows. The preconditioning matrix $\underline{\underline{\Gamma}}$ of Weiss and Smith [105] is introduced as following for conserved variables (see Turkel [101])

$$\underline{\underline{\Gamma}} = \underline{\underline{I}} + \frac{(1 - \mathrm{Ma}_{\mathrm{ref}}^2)(\gamma - 1)}{c^2} \cdot \begin{pmatrix} \beta & -\underline{u}^T & 1 \\ \underline{u}\beta & -\underline{u}\,\underline{u}^T & -\underline{u} \\ H\beta & -(H\underline{u})^T & H \end{pmatrix} \ , \tag{3.33}$$

with the identity matrix $\underline{\underline{I}}$ and

$$\beta = \frac{1}{2}|\underline{u}|^2 \ . \tag{3.34}$$

The convective terms in the governing equations are multiplied with this matrix:

$$\frac{\partial}{\partial t}\iiint \underline{W}\mathrm{d}V + \underline{\underline{\Gamma}}\iint[\underline{F}_{\mathrm{inv}} - \underline{F}_{\mathrm{vis}}]\cdot\mathrm{d}\underline{A} = \underline{S}\ . \tag{3.35}$$

This has the effect of re-scaling the acoustic speed of the system to mitigate the numerical stiffness encountered at low Mach numbers and incompressible flow.

The reference Mach number $\mathrm{Ma}_{\mathrm{ref}}$ is introduced to avoid singularities in regions where the local Mach number approaches zero (e.g. stagnation points):

$$\mathrm{Ma}_{\mathrm{ref}}^2 = \begin{cases} \varepsilon^2 & \text{if} \quad \mathrm{Ma} < \varepsilon \\ \mathrm{Ma}^2 & \text{if} \quad \varepsilon < \mathrm{Ma} < 1 \\ 1 & \text{if} \quad \mathrm{Ma} > 1 \end{cases}, \tag{3.36}$$

where ε is a small number ($\sim 10^{-5}$).

3.1.4 Time-Marching Scheme

An explicit low storage time-stepping scheme is used to discretize the time derivative in Eqn. (3.1). The solution is advanced from time t to time $t + \Delta t$ with a 5-stage Runge-Kutta scheme. It starts with the results from the last time step t:

$$\underline{W}^{(0)} = \underline{W}(t)\ . \tag{3.37}$$

Each stage is calculated based on the first stage $\underline{W}^{(0)}$ and the residuals from the current stage $\underline{W}^{(i)}$:

$$\underline{W}^{(i+1)} = \underline{W}^{(0)} - \alpha_i \Delta t \underline{R}\left(\underline{W}^{(i)}\right)\ , \tag{3.38}$$

with the stage counter i, the stage coefficient α_i for the i-th stage, the solution for the i-th stage $\underline{W}^{(i)}$ and the residuals $\underline{R}$. Finally, the solution for the next time step $t + \Delta t$ is the 5th stage of the Runge-Kutta scheme:

$$\underline{W}(t + \Delta t) = \underline{W}^{(5)} = \underline{W}^{(0)} - \alpha_5 \Delta t \underline{R}\left(\underline{W}^{(4)}\right)\ . \tag{3.39}$$

The scheme is called low storage since only the results of the last time step and the current Runge-Kutta stage have to be stored. According to Blazek [12], the best coefficients for a 5-stage Runge-Kutta scheme with second order spatial discretization are defined as:

$$\alpha_1 = 0.0695 \ , \quad \alpha_2 = 0.1602 \ , \quad \alpha_3 = 0.2898 \ , \quad \alpha_4 = 0.5060 \ , \quad \alpha_5 = 1.0 \ .$$

This results in a maximum stable Courant number of 1.15.

Local Time Stepping

The convergence of the steady-state solution can be increased by using the maximal permissible time step in each cell based on a local stability criteria. For the stability criteria, both the inviscid and viscous character of the Navier-Stokes equations has to be considered. Therefore, the local time step is calculated according to Arnone et al. [4]:

$$\Delta t = \mathrm{Co} \frac{\Delta t_{\mathrm{inv}} \cdot \Delta t_{\mathrm{vis}}}{\Delta t_{\mathrm{inv}} + \Delta t_{\mathrm{vis}}} \ , \tag{3.40}$$

with the Courant number Co and the inviscid and viscous time step in each cell Δt_{inv} and Δt_{vis}, respectively. These are calculated as follows:

$$\Delta t_{\mathrm{inv}} = \frac{\Delta x}{|\underline{u}| + c} \ , \qquad \Delta t_{\mathrm{vis}} = \frac{\Delta x^2 \rho}{\mu_{\mathrm{eff}}} \ , \tag{3.41}$$

with the effective dynamic viscosity $\mu_{\mathrm{eff}} = \mu + \mu_{\mathrm{t}}$ and the turbulent viscosity μ_{t}. Different definitions for the characteristic cell length Δx exist in literature. In this work, the ratio of each cell volume to its maximum cell face area is used defined by Borm [15], which yields a minimum length of the cell:

$$\Delta x = \frac{V}{A_{\mathrm{max}}} \ . \tag{3.42}$$

Dual Time Stepping

Acceleration techniques like local time stepping, residual smoothing and preconditioning can be used to quickly reach steady-state solutions. However, these methods also

destroy the temporal accuracy of the solution. For this reason, dual time stepping is employed to be able to solve time-dependent problems. This method was first introduced by Merkle and Athavale [73] and extensively used for compressible flows (for example Jameson [51]). Alongside the physical time t, a pseudo time τ is introduced in the governing equation:

$$\underbrace{\frac{\partial}{\partial t}\iiint \underline{W}\mathrm{d}V}_{\text{Physical time derivative}} + \underbrace{\frac{\partial}{\partial \tau}\iiint \underline{W}\mathrm{d}V}_{\text{Pseudo time derivative}} + \underline{\underline{\Gamma}}\iint [\underline{F}_{\text{inv}} - \underline{F}_{\text{vis}}] \cdot \mathrm{d}\underline{A} = \underline{S} \ . \tag{3.43}$$

In case of $\tau \to \infty$, the pseudo time derivative vanishes and the original governing equation is recovered. The physical time dependent term is discretized using a second order three-point backwards differencing scheme while the pseudo time is discretized using the second order Runge-Kutta scheme. The semi-discrete formulation of the governing equations is as follows

$$\underline{W}^{i+1}\left(\frac{1}{\alpha_i \Delta\tau} + \frac{3}{2}\frac{1}{\Delta t}\right) = \left[\frac{1}{\alpha_i \Delta\tau}\underline{W}^{j} + \frac{4}{2}\frac{1}{\Delta t}\underline{W}^{n} - \frac{1}{2}\frac{1}{\Delta t}\underline{W}^{n-1}\right] - \underline{R}\left(\underline{W}^{i}\right) \tag{3.44}$$

with the physical time index n, the pseudo time index j, and Runge-Kutta stage counter i. At first, the inner iterations are performed until the Runge-Kutta scheme is completed at $i_{\max} = 5$. This concludes the current pseudo time step and the next one $j + 1$ starts with solving the inner iterations again. New values for $\underline{W}^{i+1}$ are computed using the old pseudo step $\underline{W}^{j}$ and the residuals at the corresponding inner iteration $\underline{R}(\underline{W}^{i})$. During these iterations, the physical time index n stays constant. In this way, the physical time derivatives act like an additional source term for the pseudo time iterations. This procedure is repeated until the pseudo time derivative reaches zero which indicates a converged pseudo time step solution. At this point, the next physical time step $n + 1$ is started.

The physical time step is only limited by the desired temporal accuracy, while the pseudo time step is limited by the Courant number stability condition. Figure 3.2 shows the flow chart of the numerical model. In case of steady-state simulations, the dual time stepping scheme is omitted.

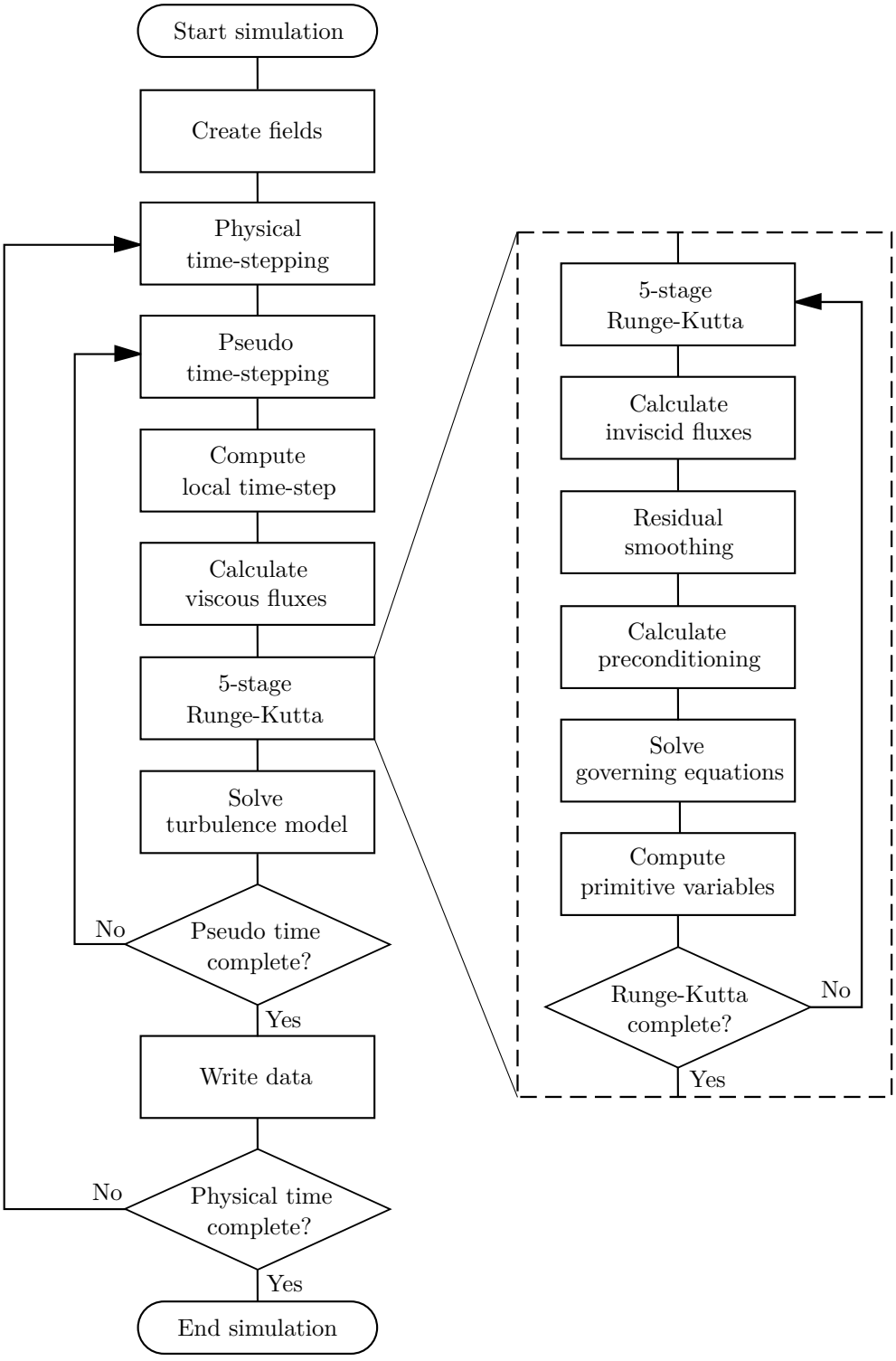

Figure 3.2: Flow chart of the proposed numerical model.

3.2 Turbulence Modeling

The turbulence of the flow is modeled using the compressible version of the Reynolds-Averaged Navier Stokes (RANS) shear-stress transport (SST) $k-\omega$ turbulence model. It was originally developed by Menter [70] as a linear eddy viscosity model based on the Bousinesq assumption for the Reynolds stress tensor:

$$\underline{\underline{\tau}}_{RS} = \mu_t \left[\nabla \underline{u} + (\nabla \underline{u})^T - \left(\frac{2}{3} \nabla \cdot \underline{u} \right) \underline{\underline{I}} \right] - \frac{2}{3} \rho k \underline{\underline{I}} \ , \tag{3.45}$$

with the turbulent dynamic viscosity μ_t. The third term in brackets is zero for incompressible flows and the last term is often ignored for non-supersonic speed flows. Density-based (Favre) average is used for the primitive variables (not shown here).

The SST $k-\omega$ model uses a blending function F_1 to combine the standard $k-\epsilon$ model from Launder and Spalding [61] in the free-stream region and the revised version of the $k-\omega$ model from Wilcox [106] in the near-wall flow. This way, advantages of both models can be combined including accurate modeling of the near-wall flow, prediction of flow separation under adverse pressure gradients as well as a high robustness and computational cheapness. Furthermore, many modifications exist incorporating effects such as surface roughness, curvature, and transition.

The implemented model was presented by Menter and Esch [71] and consists of two governing equations for the turbulent kinetic energy k and the specific dissipation ω:

$$\frac{\partial(\rho k)}{\partial t} + \frac{\partial(\rho u_j k)}{\partial x_j} = \widehat{P}_k - \beta^* \rho \omega k + \frac{\partial}{\partial x_j} \left[(\mu + \sigma_k \mu_t) \frac{\partial k}{\partial x_j} \right] \ , \tag{3.46}$$

$$\begin{aligned} \frac{\partial \rho \omega}{\partial t} + \frac{\rho u_j \omega}{\partial x_j} = {} & \frac{\gamma}{\nu_t} P_\omega - \beta \rho \omega^2 + \frac{\partial}{\partial x_j} \left[(\mu + \sigma_\omega \mu_t) \frac{\partial \omega}{\partial x_j} \right] \\ & + 2(1 - F_1) \frac{\rho \sigma_{\omega 2}}{\omega} \frac{\partial k}{\partial x_j} \frac{\partial \omega}{\partial x_j} \ , \end{aligned} \tag{3.47}$$

with the definition of the turbulent viscosity and turbulent thermal diffusivity:

$$\nu_t = \frac{\mu_t}{\rho} \ , \qquad \mu_t = \frac{\rho a_1 k}{\max(a_1 \omega, S F_2 F_3)} \ , \qquad a_t = \frac{\mu_t}{\mathrm{Pr}_t \rho} \ , \tag{3.48}$$

and the turbulent Prandtl number Pr_t. The magnitude of strain rate tensor S is

calculated as following:

$$S = \sqrt{2S_{ij}S_{ij}} \,, \qquad S_{ij} = \frac{1}{2}\left(\frac{\partial u_i}{\partial x_j} + \frac{\partial u_j}{\partial x_i}\right) \,. \tag{3.49}$$

The blending function F_1 is formulated as following:

$$F_1 = \tanh\left\{\left\{\min\left[\max\left(\frac{\sqrt{k}}{\beta^*\omega y}, \frac{500\nu}{y^2\omega}\right), \frac{4\sigma_{\omega 2}\rho k}{CD_{k\omega}y^2}\right]\right\}^4\right\} \,, \tag{3.50}$$

where y denotes the distance to the nearest wall and ν the kinematic viscosity. This function is zero in the free stream of the flow and one in the boundary layer.

The second blending function F_2 behaves like F_1 and is defined as:

$$F_2 = \tanh\left\{\left(\max\left[\frac{2\sqrt{k}}{\beta^*\omega y}, \frac{500\nu}{y^2\omega}\right]\right)^2\right\} . \tag{3.51}$$

The function F_3 was designed by Hellsten [43] to prevent the limitation in equation (3.48) to be activated in the roughness layer of rough-wall flows:

$$F_3 = 1 - \tanh\left[\left(\min\left[\frac{150\nu}{\omega y^2}, 10\right]\right)^4\right] \,. \tag{3.52}$$

This function is disabled in case of smooth walls. A production limiter is used to prevent the build-up of turbulence in stagnation regions

$$\widehat{P}_k = \min\left(P_k, 10\beta^*\rho k\omega\right) \,, \quad P_\omega = \min\left(P_k, \frac{c_1}{a_1}\beta^*\omega \cdot \max\left[a_1\omega, b_1F_2F_3S\right]\right) \tag{3.53}$$

with the turbulent production

$$P_k = \tau_{ij}\frac{\partial u_i}{\partial x_j} \,. \tag{3.54}$$

The positive portion of the cross-diffusion term $CD_{k\omega}$ is calculated as follows

$$CD_{k\omega} = \max\left(\frac{2\rho}{\sigma_{\omega 2}\omega}\frac{\partial k}{\partial u_j}\frac{\partial \omega}{\partial x_j}; CD_{k\omega,\min}\right) \,. \tag{3.55}$$

The coefficients for the model are a linear combination of the corresponding values of

the $k-\omega$ and $k-\epsilon$ turbulence model

$$\phi = \phi_1 F_1 + \phi_2(1 - F_1) \ , \tag{3.56}$$

with the coefficients being taken from an updated form of the SST model by Menter et al. [72]:

$$\begin{aligned} \sigma_{k1} &= 0.85 \ , & \sigma_{k2} &= 1.0 \ , & \sigma_{\omega 1} &= 0.5 \ , & \sigma_{\omega 2} &= 0.856 \ , \\ \beta_1 &= 0.075 \ , & \beta_2 &= 0.0828 \ , & \gamma_1 &= 5/9 \ , & \gamma_2 &= 0.44 \ , \\ a_1 &= 0.31 \ , & b_1 &= 1.0 \ , & c_1 &= 10.0 \ , & \mathrm{Pr}_t &= 1.0 \ , \\ CD_{k\omega,\min} &= 10^{-10} \ , & \beta^* &= 0.09 \ . \end{aligned} \tag{3.57}$$

Rotation and Curvature Correction

In order to account for the effects of rotation and curvature (RC) on the flow, the production term P_k in the k and ω equation gets multiplied by the function f_{r1}. This function was developed by Smirnov and Menter [90] and has the following form:

$$f_{r1} = \max\left[\min\left(f_{\mathrm{rot}}, 1.25\right), 0\right] \ , \tag{3.58}$$

with

$$f_{\mathrm{rot}} = (1 + c_{r1})\frac{2r^*}{1 + r^*}[1 - c_{r3}\tan^{-1}(c_{r2}\hat{r})] - c_{r1} \ . \tag{3.59}$$

The value of f_{r1} is larger than one for concave curvatures which results in enhanced production rate and less than one for convex curvatures leading to decreased production rate in the turbulent equations. Both r^* and $\hat{r}$ depend on the strain rate tensor S_{ij}, the rotation rate tensor W_{ij}, and the angular velocity of the rotating frame of reference $\underline{\omega}$:

$$r^* = \frac{S}{W} \ , \tag{3.60}$$

with the magnitude of the rotation rate tensor

$$W = \sqrt{2W_{ij}W_{ij}} \ , \qquad W_{ij} = \frac{1}{2}\left(\frac{\partial u_i}{\partial x_j} - \frac{\partial u_j}{\partial x_i} + 2\varepsilon_{mji}\,\omega_m\right) \ , \tag{3.61}$$

and

$$\hat{r} = \frac{2W_{ik}S_{jk}}{WD^3}\left(\frac{\mathrm{D}S_{ij}}{\mathrm{D}t} + \left(\varepsilon_{imn}S_{jn} + \varepsilon_{jmn}S_{in}\right)\omega_m\right) , \tag{3.62}$$

with the Levi-Civita symbol ε_{ijk},

$$D^2 = \max(S^2, 0.09\omega^2) , \tag{3.63}$$

and the Lagrangian derivative of the strain rate tensor $\mathrm{D}S_{ij}/\mathrm{D}t$. Note that the equations above are written in Einstein summation convention. The constants for the SST $k-\omega$ RC turbulence model are as following:

$$c_{r1} = 1.0 , \qquad c_{r2} = 2.0 , \qquad c_{r3} = 1.0 . \tag{3.64}$$

3.3 Boundary Conditions

The boundary conditions for the numerical model are based on the primitive variables $(p, \boldsymbol{u}, T)^T$ rather than the conserved variables. The advantage is that the primitive variables are provided by the experiments and can directly be used as boundary conditions for the simulations.

Inlet

Turbomachinery simulation typically define total field values for pressure and temperature at the inlet boundary since detailed velocity profiles are difficult to measure. These boundary conditions are defined for a compressible flow as following:

$$p_{\mathrm{tot}} = p\left(1 + \frac{\gamma-1}{2}\mathrm{Ma}^2\right)^{\frac{\gamma}{\gamma-1}} , \qquad T_{\mathrm{tot}} = T\left(1 + \frac{\gamma-1}{2}\mathrm{Ma}^2\right) . \tag{3.65}$$

The turbulent kinetic energy and the specific dissipation are estimated by:

$$k = \frac{3}{2}I_t^2|\underline{u}| , \qquad \omega = \frac{k^{1/2}}{C_\mu^{1/4}L_{\mathrm{mix}}} , \tag{3.66}$$

with the constant $C_\mu = 0.09$, the turbulent intensity I_t and the mixing length L_{mix}, which is defined as:

$$L_{\text{mix}} = 0.07\, d \ , \tag{3.67}$$

with the pipe diameter d.

Outlet

Either a fixed static pressure or a mass flow outlet can be defined. The latter can be achieved by changing the static pressure during each iteration until the target mass flow is reached:

$$\Delta p = \frac{(\dot{m} - \dot{m}_{\text{tar}})^2}{2\bar{\rho}^2 A^2} \ , \tag{3.68}$$

with the change in pressure Δp with respect to the previous time step, the actual mass flow rate at the current iteration $\dot{m}$, the target mass flow rate $\dot{m}_{\text{tar}}$, the average density $\bar{\rho}$ and area of the outlet patch A, respectively. This boundary condition can be stabilized defining upper and lower boundaries for the resulting static pressure. Other variables $\underline{\Phi}$ at the outlet are treated as zero gradient normal to the patch:

$$0 = \underline{n} \cdot \nabla \underline{\Phi} \ . \tag{3.69}$$

Wall

Walls are defined as no-slip and adiabatic. This results in the following conditions:

$$0 = \underline{n} \cdot \nabla p \ , \qquad \underline{u} = (0,0,0)^T \ , \qquad 0 = \underline{n} \cdot \nabla T \ . \tag{3.70}$$

The effect of the turbulent boundary layer is modeled using an all-y^+ wall function. It is based on Spaldings law of the wall [91], which covers the laminar sublayer, transition region and turbulent core (see Figure 3.3):

$$y^+ = u^+ + e^{-\kappa B}\left[e^{\kappa u^+} - 1 - \kappa u^+ - \frac{(\kappa u^+)^2}{2} - \frac{(\kappa u^+)^3}{6}\right] \tag{3.71}$$

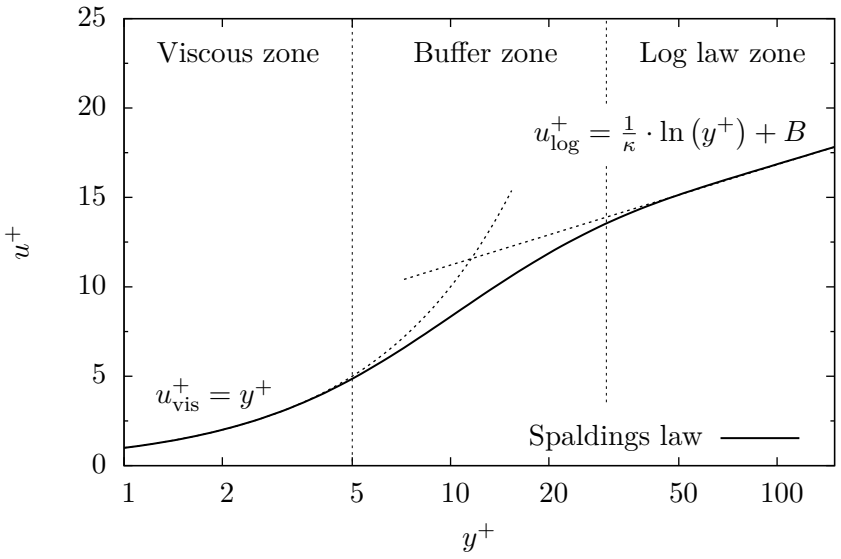

Figure 3.3: Theoretical dimensionless velocity profile in the near-wall region.

with $\kappa = 0.41$ and $B = 5.0$. The non-dimensional wall distance y^+ and velocity u^+ are defined as

$$y^+ = \frac{y u_\tau \rho}{\mu} \,, \qquad\qquad u^+ = \frac{u_\parallel}{u_\tau} \tag{3.72}$$

where y denotes the distance to the nearest wall, $u_\parallel$ the velocity magnitude parallel to the wall and u_τ the friction velocity

$$u_\tau = \sqrt{\frac{\tau_{\text{wall}}}{\rho}} \tag{3.73}$$

with the wall shear stress τ_{wall}. This wall function has the advantage of being valid in the complete boundary layer. Furthermore, it reduces the requirements for the near-wall mesh and increases the accuracy in case of a dimensionless near-wall distance below 30. This is in particular the case when compared to a standard wall function, which is only valid in the logarithmic region of the boundary layer.

Turbulent Quantities

The specific dissipation for a smooth and rough wall is formulated as follows

$$\omega_{\text{wall}} = \sqrt{\omega_{\text{vis}}^2 + \omega_{\text{log}}^2} \tag{3.74}$$

blending between the viscous sublayer ω_{vis} and the logarithmic region ω_{log} where

$$\omega_{\text{vis}} = \frac{6\mu}{\rho\beta_1 y^2} \ , \qquad \omega_{\text{log}} = \frac{k^{1/2}}{C_\mu^{1/4}\kappa y} \ . \tag{3.75}$$

The wall normal gradient of the turbulent kinetic energy is set to zero

$$0 = \underline{n} \cdot \nabla k \ . \tag{3.76}$$

4 Validation

Two different test cases are used to assess the accuracy of the developed numerical model: (1) The performance at low subsonic speeds is evaluated using the laminar flow around a circular cylinder. This case is suitable to evaluate the accuracy at very low speeds for steady-state and unsteady flows at Reynolds numbers of $5 - 100$ due to a large number of reference publications. Almost constant density and overrated dissipation make it challenging for density-based solver. (2) The well documented Radiver centrifugal compressor investigated by Ziegler et al. [112, 113] is chosen to investigate the performance at high speeds in a rotating frame of reference. The correct prediction of mechanical losses and turbulence modeling under adverse pressure gradients as well as strong curvature make this validation case challenging.

4.1 Laminar Flow around a Circular Cylinder

4.1.1 Numerical Model

The two-dimensional incompressible flow around a circular cylinder is simulated to investigate the solver performance at very low Mach numbers. Numerous experimental and numerical investigations can be found in literature (e.g. [17, 28, 36, 81, 96]). Therefore, a large database of reference results can be used. The cylinder has a diameter of $d = 1\,\mathrm{m}$ and is placed inside a cylindrical domain with an outer diameter of $75 \times d$ (see Figure 4.1). This way, the influence of the boundary conditions can be minimized. The farfield is defined as atmosphere with ambient conditions set to $10^5\,\mathrm{Pa}$ and $300\,\mathrm{K}$. A mesh dependency study not shown here revealed that a block-structured hexahedral grid with 120×240 elements in radial and circumferential directions, respectively offers the best compromise between accuracy and computational cost.

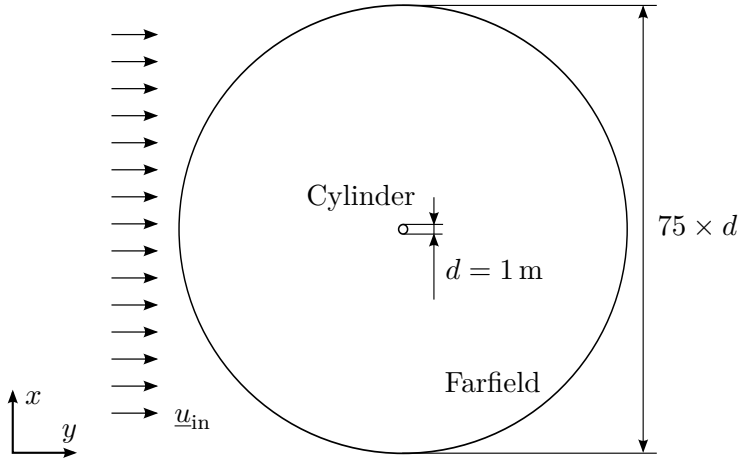

Figure 4.1: Computational domain of the circular cylinder flow.

This results in a total of 28,800 cells. The flow is assumed to be laminar. Transient simulations are carried out due to the development of an unsteady von Kármán vortex street at Reynolds number above 40. The time step is set to $\Delta t = 2 \cdot 10^{-3}\,\mathrm{s}$ which results in a maximum Courant number of 2.0.

Reynolds number, Mach number, and Strouhal number are used to characterize the case. These dimensionless quantities are calculated as follows:

$$\mathrm{Re} = \frac{|\underline{u}_{\mathrm{in}}|d}{\nu}\,, \qquad \mathrm{Ma} = \frac{|\underline{u}_{\mathrm{in}}|}{c}\,, \qquad \mathrm{St} = \frac{fd}{|\underline{u}_{\mathrm{in}}|}\,, \tag{4.1}$$

with the magnitude of inlet velocity $|\underline{u}_{\mathrm{in}}|$, the kinematic viscosity ν, and the vortex shedding frequency f. Based on the chosen values for Re and Ma, the inlet velocity and viscosity can be determined. The drag coefficient is defined as:

$$C_{\mathrm{D}} = \frac{2\,|\underline{F}_{\mathrm{D}}|}{\rho|\underline{u}_{\mathrm{in}}|^2 A}\,, \tag{4.2}$$

where $\underline{F}_{\mathrm{D}}$ denotes the drag force onto the cylinder consisting of shear stress and pressure contributions, and A the projected cross sectional area. Furthermore, the separation angle δ_s and the dimensionless wake length L_w/d are used to compare the numerical model with reference solutions. These characteristics are explained in Figure 4.2.

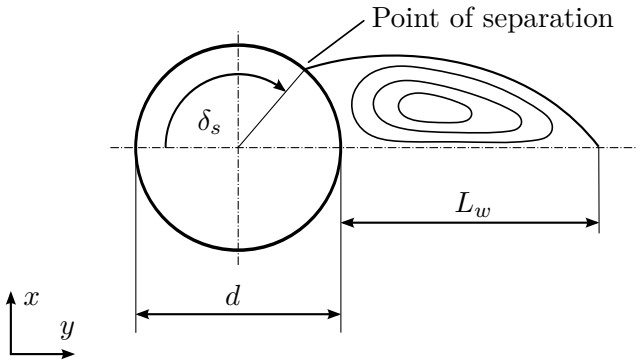

Figure 4.2: Definition of separation angle δ_s and dimensionless wake length L_w/d after Chatterjee et al. [22].

Table 4.1: Drag coefficient C_D, separation angle δ_s, and dimensionless wake length L_w/d of the flow around a circular cylinder for $\mathrm{Re} = 40$.

Publication	C_D	δ_s	L_w/d	Simulation
Bouchon et al. [17]	1.50	126.6°	2.26	incompressible
Gautier et al. [36]	1.49	126.4°	2.24	incompressible
Patil and Lakshmisha [81]	1.56	127.3°	2.14	incompressible
Taira and Colonius [96]	1.54	126.3°	2.30	incompressible
Present solution	1.52	126.2°	2.18	compressible

4.1.2 Results

The correct prediction of the drag coefficient at different Reynolds numbers is investigated in the first part. Therefore, the inlet Mach number is fixed at 0.05, which results in $\underline{u}_\mathrm{in} = 17.36\,\mathrm{m/s}$. The kinematic viscosity is varied to achieve Reynolds numbers from 5 up to 100 and coefficients are averaged over time. Figure 4.3 (left) shows the drag coefficient as a function of the Reynolds number. The simulations are compared against experimental data of Tritton [97]. The numerical results agree very well for the complete range of Reynolds numbers. A detailed analysis for $\mathrm{Re} = 40$ is presented in Table 4.1. The drag coefficient and the dimensionless wake length are well within the range of other research groups. However, the separation angle is at the lower end of the reference results.

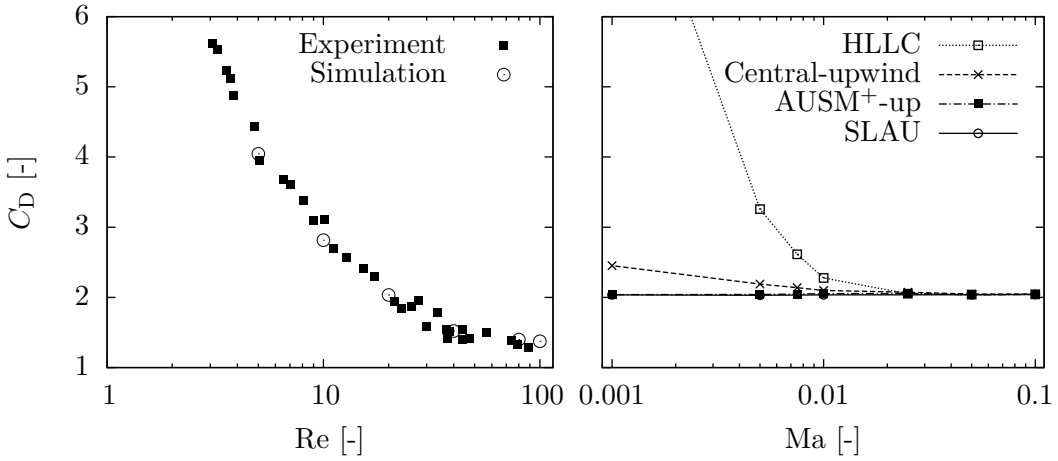

Figure 4.3: Drag coefficient as a function of the Reynolds number compared to the experimental data of Triton [97] (left) and as a function of the Mach number at Re = 20 for different flux calculation methods (right).

One advantage of the SLAU flux calculation algorithm is the low dissipation at all Mach numbers. This behavior is investigated by choosing a constant Reynolds number of 20 and varying the inlet Mach number between $0.001 - 0.1$. The drag coefficient as a function of the inlet Mach number is shown in Figure 4.3 (right) for different flux calculation schemes:

- Harten-Lax-van Leer-Contact (HLLC) methods from Luo et. al [67],
- central-upwind schemes of Kurganov et. al [60],
- AUSM$^+$-up scheme by Liou [64],
- SLAU method by Kitamura and Shima [57] (proposed model) .

The HLLC scheme shows a significant influence of the flow velocity onto the results. At low speeds, the dissipation leads to an overprediction of the flow losses and drag coefficient. The central-upwind method shows a better performance. Still, the coefficient is overestimated by up to 20 %. In comparison to that the SLAU method and the AUSM$^+$-up show a very similar performance and correctly predict a value of $C_D \approx 2.04$ for all Mach numbers. Compared to AUSM-up$^+$, the SLAU evaluation has the advantage of not depending on a user-defined characteristic cut-off Mach number. In cases with a wide range of flow phenomenons, such a characteristic value

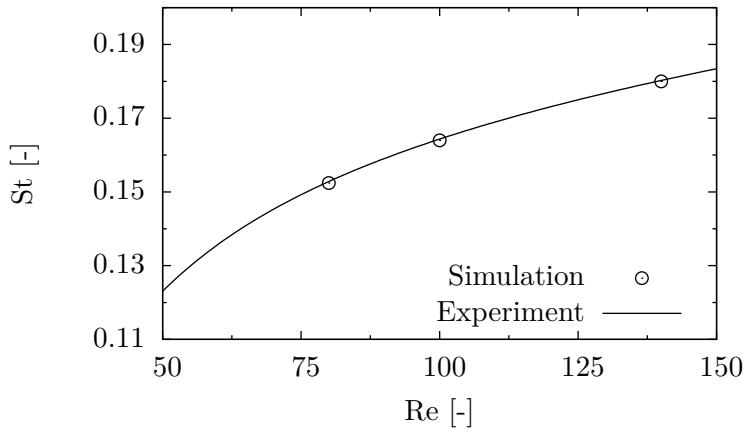

Figure 4.4: Strouhal number as a function of the Reynolds number for numerical and experimental results of Williamson [107] for Ma = 0.05.

cannot easily be determined. Therefore, the SLAU scheme is chosen for the present turbomachinery investigations.

At higher Reynolds numbers, the flow around a circular cylinder becomes unsteady and periodic. This is also referred to as von Karman vortex street. The Mach number is set to 0.05 with a Reynolds number of 80, 100 and 140. The Strouhal number characterizes the oscillating pattern using the flow shedding frequency f. This characteristic parameter is plotted against the Reynolds number in Figure 4.4. The Strouhal-Reynolds number relationship was experimentally discovered by Williamson [107] and is given by

$$\mathrm{St} = -\frac{3.3265}{\mathrm{Re}} + 0.1816 + 1.600 \cdot 10^{-4}\,\mathrm{Re}\ . \tag{4.3}$$

The simulated Strouhal number coincides very well with the reference data showing the very good temporal accuracy of dual time stepping.

Figure 4.5 shows the L_2 norm $\|\rho\|_2$ of the density with and without preconditioning for Ma = 0.1 and Re = 20. Preconditioning significantly increases the convergence rate and decreases the average residual by one order of magnitude. Disabling preconditioning yields in pressure waves travelling through the domain which leads to peaks in the residuals. This shows, flux preconditioning effectively removes the convergence problems at low Mach numbers. At the same time, preconditioning and convergence acceleration methods have no negative influence on the spatial accuracy of the solver.

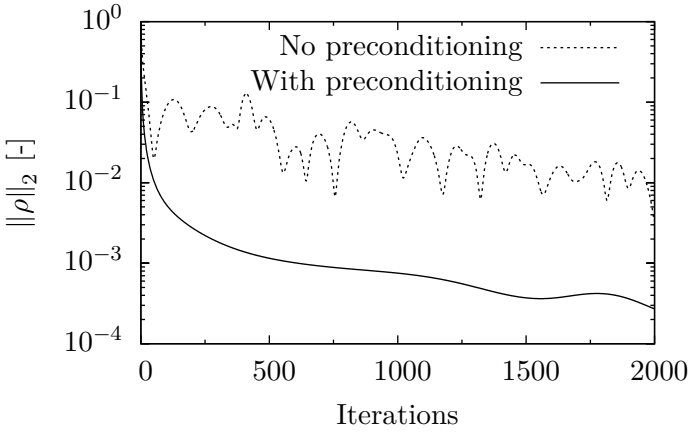

Figure 4.5: L_2 norm of density $\|\rho\|_2$ with and without preconditioning for Ma = 0.1 and Re = 20.

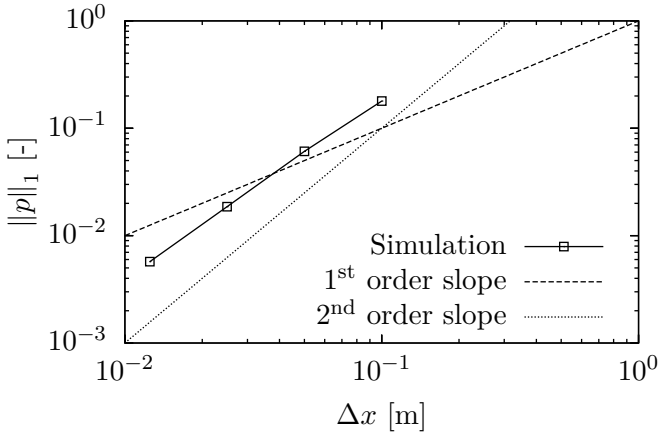

Figure 4.6: L_1 norm of surface pressure $\|p\|_1$ as a function of the base cell size Δx for Ma = 0.1 and Re = 20.

The L_1 norm of the cylinder surface pressure $\|p\|_1$ is plotted in Figure 4.6 at the same flow conditions. Comparing the simulation results with the idealized slopes shows that the proposed model offers a second order spatial accuracy. The reference mesh had a resolution of 480×960 cells in radial and circumferential direction.

The results of the two-dimensional, subsonic flow around a cylinder show that the proposed numerical model is capable of accurately computing steady-state and unsteady flows at very low Mach numbers. Local flow variables like the separation angle and integral values like the drag coefficient are predicted very well.

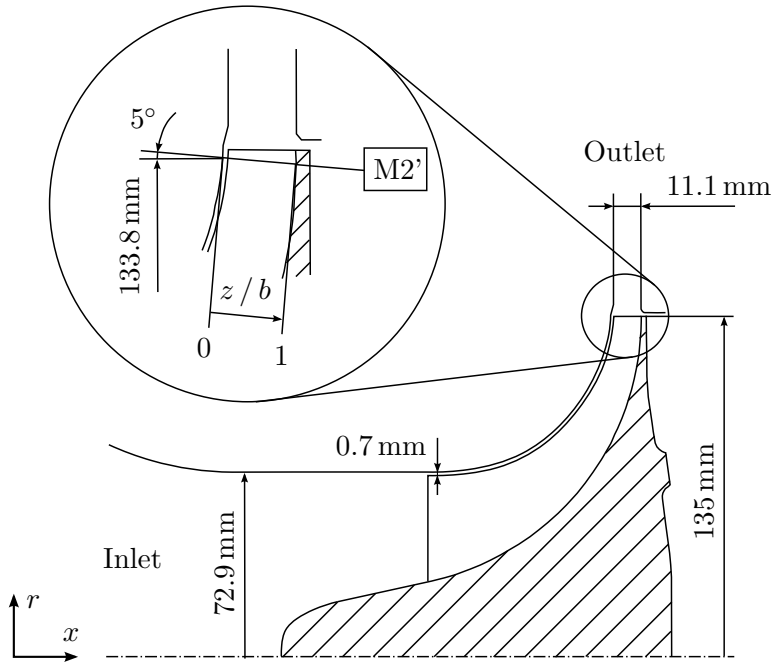

Figure 4.7: Meridional cross section of the Radiver compressor and the definition of the measurement plane M2' after Ziegler et al. [112, 113].

4.2 Radiver High-Speed Centrifugal Compressor

4.2.1 Numerical Model

The Radiver high-speed centrifugal compressor stage is the second validation case. It was experimentally investigated by Ziegler et al. [112, 113] at the Institute of Jet Propulsion and Turbomachinery at RWTH Aachen, Germany. The experiments were performed to gain insight on the impeller-diffuser interaction under consideration of different radial gaps and diffuser vane angles. The authors used steady probe measurements at the impeller exit and diffuser exit to investigate integral flow losses for different diffuser geometries and operating points. Furthermore, laser-2-focus velocimeter measurements were performed to analyze the unsteady and time-averaged flow field between the impeller exit region and the diffuser throat. The geometry and experimental results were published for CFD code validation. Therefore, the Radiver test case is very well suited for numerical code validation (for example Boncinelli and Arnone [14], Moroz et al. [78], Borm and Kau [16]).

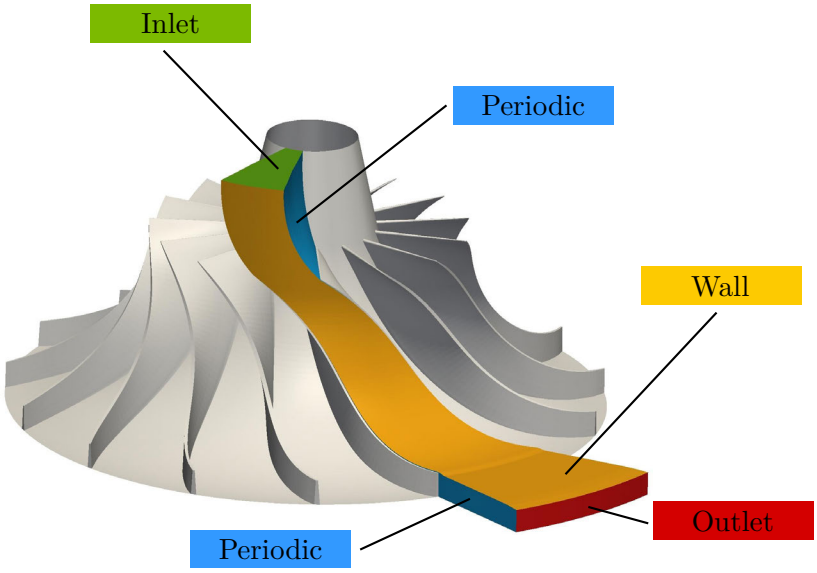

Figure 4.8: Computational domain of the Radiver centrifugal compressor.

The experimental setup for the validation consists of an impeller and a vaneless diffuser. The impeller has 15 blades with a back sweep of 38° and an impeller exit radius of 135 mm. The tip clearance is 0.7 mm and the vaneless diffuser has a constant height of 11.1 mm. Figure 4.7 shows the meridional cross section of the compressor. Laser-2-focus measurements at plane M2' are used for validation. The plane is located close to the impeller exit at a radius of 133.8 mm and is inclined by about 5° against the axis of rotation. The centrifugal compressor operates at high subsonic speeds. The absolute Mach number at the impeller exit is 0.94 at the design speed of $n = 35\,000\,\mathrm{min}^{-1}$. This results in a circumferential velocity of 498 m/s. The total pressure ratio at design point is 4.07 at a mass flow rate of 2.5 kg/s and an isentropic efficiency of 83.4 %.

One single blade passage is modeled for the simulation due to symmetry reasons (see Figure 4.8). The spinner of the compressor wheel is not considered. The inlet is located 45 mm upstream of the leading edge of the impeller and the outlet 55 mm downstream of the trailing edge. A block-structured hexahedral mesh is used for the impeller with $60 \times 80 \times 100$ cells in spanwise, pitchwise and meridional direction, respectively. The tip gap is resolved using 10×10 cells. This results in a total cell count of 0.93×10^6 with an average y^+ value of 24 for the impeller. The grid resolution is higher than comparable publications such as Boncinelli and Arnone [14], and Borm and Kau [16]. For this reason, a grid dependency study is omitted.

Table 4.2: Boundary conditions for the Radiver centrifugal compressor.

Inlet	p_{tot}	59.6 kPa
	T_{tot}	295 K
	I_t	3 %
	L_t	7 mm
Outlet	p	(124 – 134) kPa
	others	zero Gradient

The total pressure and total temperature of 59,600 Pa and 295 K are defined at the inlet according to the experiment. The static outlet pressure is varied to achieve different mass flow rates. Zero gradient boundary conditions are used for other primitive variables at the outlet. The walls are defined as no-slip and adiabatic, and surface roughness is neglected. The turbulent intensity at the inlet is set to 3 % with a turbulent length scale of 7 mm. The rotational velocity of the compressor wheel is 28,160 min^{-1}, which corresponds to 80 % of design speed. The boundary conditions are summarized in Tab. 4.2. In order to investigate the influence of rotation and curvature, the SST $k-\omega$ with and without rotation and curvature correction (SST-RC) are compared. The discretization of the turbulent convective terms is second order.

For a better comparison, ANSYS® Fluent, Release 15.0 has been used as a second reference software since it is a well known and thoroughly validated commercial CFD code. In contrast to the setup in OpenFOAM, Fluent uses a coupled pressure-based solver. Nevertheless, the settings are similar to the presented numerical model in OpenFOAM. The spatial discretization is second order and the SST $k-\omega$ turbulence model is employed. Sutherland's law is used for the temperature dependent viscosity. Furthermore, the mesh and the boundary conditions are identical to the OpenFOAM case. Convergence is monitored by plotting mass flow rate and isentropic efficiency for each iteration.

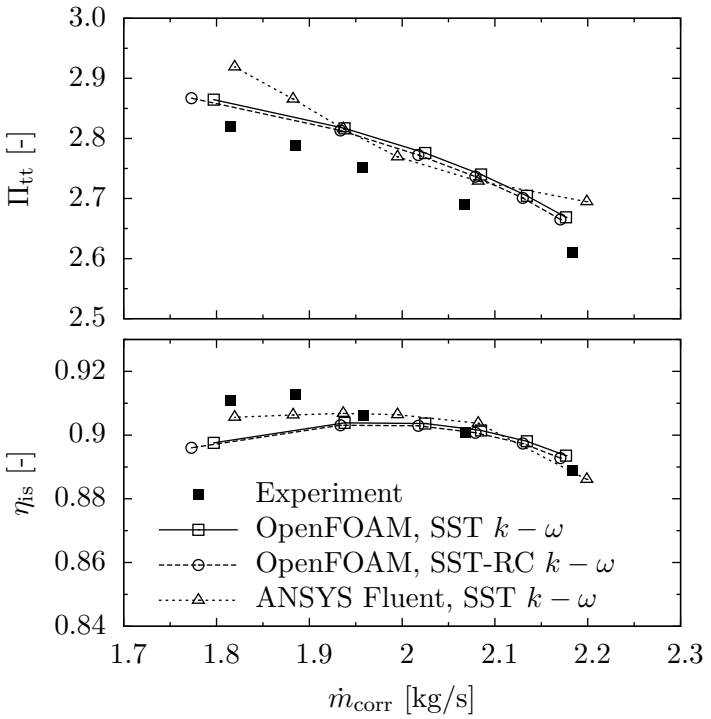

Figure 4.9: Performance curves for OpenFOAM and ANSYS® Fluent compared to the experimental results of Ziegler [112, 113].

4.2.2 Results

Figure 4.9 compares the total pressure ratio (top) and the isentropic efficiency (bottom) of the experiment and the two CFD codes. Both OpenFOAM models predict Π_{tt} well and show an overestimation of less than 3 %. In contrast, Fluent reveals an overprediction of up to 5 % and the slopes differ compared to the experiment. The influence of the rotation and curvature correction onto the performance map is only minor. The absolute value as well as the slopes of the isentropic efficiency are estimated accurately with maximum deviations of 1 %. In this case, Fluent offers a better performance in particular at low mass flow rates. One reason for the differences between simulation and experiment is the fillet radius, which was neglected in the simulations. This increases the modelled flow cross section area in the impeller and results in higher mass flow rates. Furthermore, the turbulent inlet quantities were estimated based on values in literature since no experimental values are available. Moreover, the spinner of the compressor wheel was also neglected in the simulations.

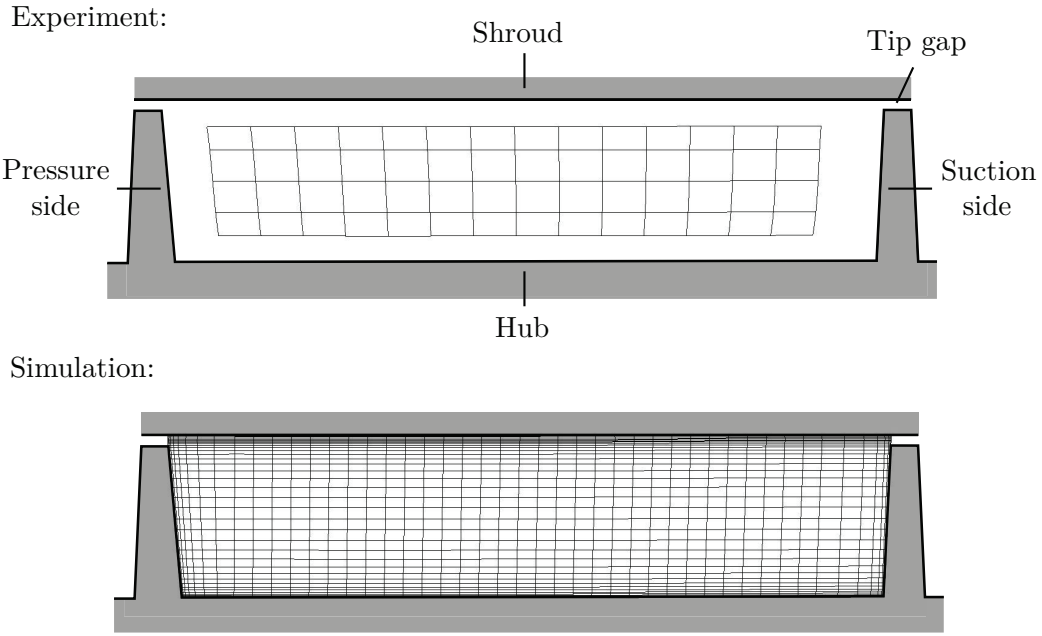

Figure 4.10: Comparison of the resolution for the Laser-2-focus velocimeter (top) and the simulation (bottom, every other line shown) at measurement plane M2' and definition of blade channel nomenclature.

Laser-2-focus velocimeter at plan M2' were used to obtain the velocity profile at 75 measurement positions close to the trailing edge of the compressor wheel. Figure 4.10 compares the spatial resolution of the experiment and the simulation and defines the nomenclature for the blade channel. The experiment has a low resolution and covers only the core of the flow inside the impeller. The near-wall flow and the tip gap are not resolved. In contrast, the grid of the numerical simulation is significantly finer. These differences has to be considered when comparing the experimental and numerical results.

Figure 4.11 shows the magnitude of the absolute velocity at the measurement plane M2' close to the trailing edge of the compressor wheel. The typical jet-wake pattern is clearly visible. A jet flow with high kinetic energy is developed from the tip gap at the suction side of the compressor wheel. At the same time, a region with low momentum fluid is located in the center close to the hub. This behavior was discovered by Eckardt [32] for the first time. The CFD codes compute these pattern correctly. The maximum velocity magnitude and the location of the jet coincide well with the measurements. However, both angle and length of the jet are slightly underestimated.

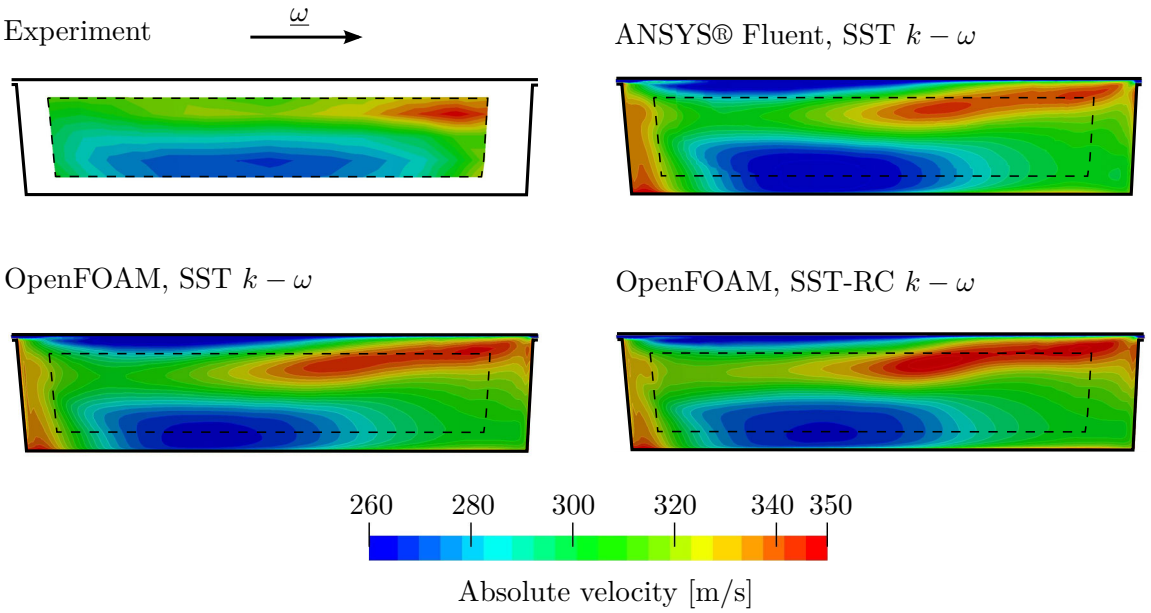

Figure 4.11: Absolute velocity at measurement plane M2'.

The location of the wake region is predicted correctly as well. The differences between both numerical solvers and the turbulence models are negligible. Unfortunately, comparisons close to the wall cannot be made.

The turbulent intensity I_t in plane M2' is shown in Figure 4.12. The maximum is located close to the shroud due to large velocity gradients between the jet flow and the casing. This leads to an increased production of turbulent kinetic energy and therefore to a higher turbulent intensity. All models correctly predict this behavior. However, the intensity is overpredicted in the core of the flow, in particular by the SST $k - \omega$ model in both codes. This effect is less severe using the rotation and curvature correction model. In general, the differences between ANSYS® Fluent and OpenFOAM are minor.

According to Tucker [100], the differences between the simulations and the experiment can be related to the RANS turbulence modeling and the corresponding inlet conditions. Turbomachinery simulation are very challenging for this type of models due to various effects such as strong curvature of the blades, adverse pressure gradients, surface roughness, flow separation with unsteady behavior, and large velocity gradients normal to the direction of flow. These flow phenomena can be tackled to some degree by using extensions to standard turbulence models, such as rotation and curvature correction,

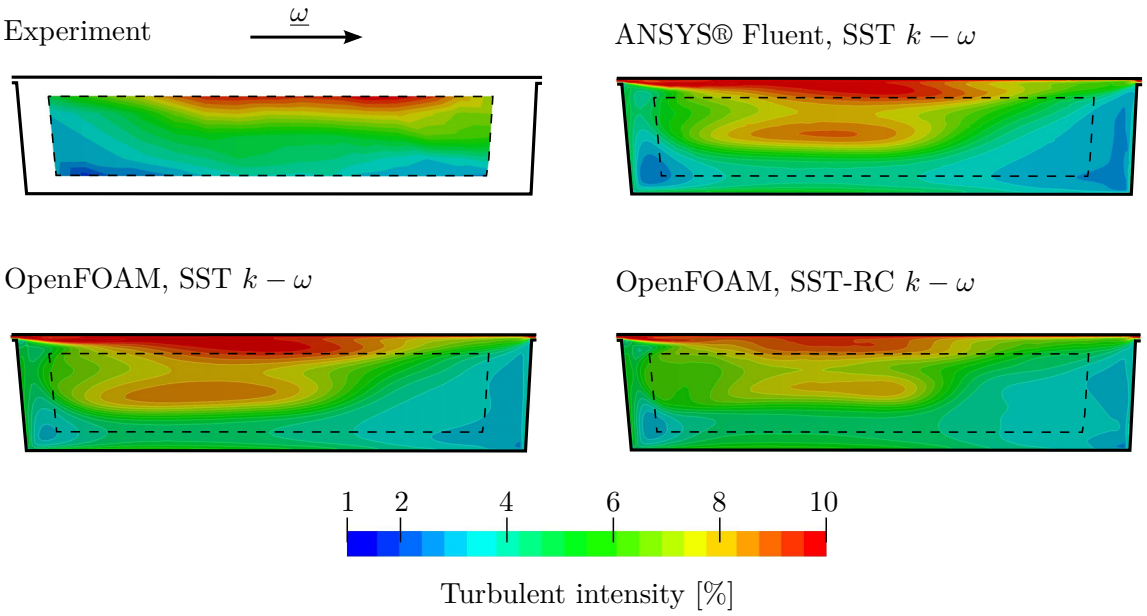

Figure 4.12: Turbulent intensity at measurement plane M2'.

or transition. Furthermore, more advanced turbulence models, such as LES/hybrid approaches, as summarized by Tucker [98, 99] can be employed. Nevertheless, the two-equation eddy viscosity models offer a good compromise between accuracy and computational cost. Furthermore, as Denton [29] stated steady RANS models can still be used to predict trends rather than absolute values. For this reason, the RANS approach is very well suited for optimization problems due to the large number of simulations and limited computational resources.

The results of the Radiver test case show that developed numerical model in OpenFOAM is capable of simulating flows in high-speed subsonic centrifugal compressors. Its accuracy compared to experimental data is on par with the commercial CFD code ANSYS® Fluent. Both turbulence models show a similar performance. However, the SST $k-\omega$ model with rotation and curvature correction is slightly more accurate. For this reason, it is also used for the investigations of the turbocharger and the optimization of the volute geometry.

5 Simulation of a Centrifugal Compressor

This chapter introduces the centrifugal compressor which is used for the genetic optimization. Its geometry and numerical model are presented. Simulations are performed to investigate grid dependency and the influence of the compressor wheel position. The computed performance map is compared with test bench measurements and reasons for deviations are discussed. Furthermore, the influence of a simplified model is investigated and its applicability for the optimization.

5.1 Compressor Performance and Geometry

The centrifugal compressor is part of a turbocharger from the project *innoSTREAM*. It was designed for passenger cars and light commercial vehicles. Figure 5.1 shows the basic design of the machine. The objective of this project was the development and design of a lighter, yet stable and reliable turbocharger with thinner housing components made of modern materials such as TRIP (Transformation Induced Plasticity) steels. They undergo a transformation process during plastic deformation and straining, resulting in an enhanced strength and ductility. However, these superior material properties are highly temperature dependent [104]. For this reason, these materials can only be applied to the compressor side of the turbocharger since exhaust gas temperatures on the turbine side exceed 850 K. In order to assess the applicability of such materials, it is vital to obtain detailed information about the flow field and temperature distribution inside the centrifugal compressor.

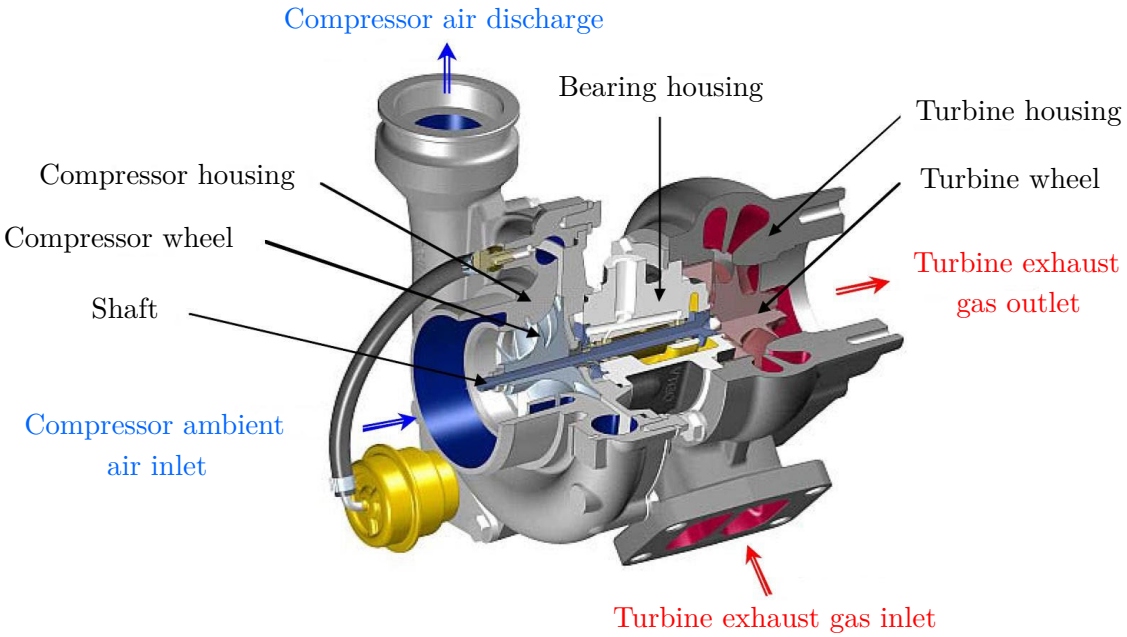

Figure 5.1: Cross-sectional view of the turbocharger.

For this reason, the focus of the investigations is on the compressor side of the turbocharger. Industrial test bench measurements were performed to characterize the performance of the compressor side (see Figure 5.2). The design point is at a rotational speed of $n = 100\,000\,\mathrm{min}^{-1}$, which is equivalent to a circumferential velocity of 340 m/s at the trailing edge of the impeller. This corresponds to a corrected mass flow rate of 0.13 kg/s of air, a total pressure ratio of 2.05 and an isentropic efficiency of 73.6 %. The maximal achievable total pressure ratio is 3.07 at $\dot{m}_{\mathrm{corr}} = 0.20\,\mathrm{kg/s}$ and $\eta_{\mathrm{is}} = 71.4\,\%$.

The impeller geometry is shown in Figure 5.3. It consists of 7 blade sets, each containing one main blade and one splitter blade with a back sweep angle of 28° at the trailing edge. The impeller inlet hub and shroud radius is 8 mm and 23 mm, respectively. The radius of the impeller exit is 32.5 mm. The tip clearance is constant at 0.3 mm. The vaneless diffuser has a tapering span with a minimum height of 4 mm. The inlet shroud is ported which extends the operational range of the compressor by shifting the surge line to lower flow rates. The ported shroud consists of three channels with supporting legs in between each channel. The air can recirculate through a slot back to the inlet region in order to suppress surge.

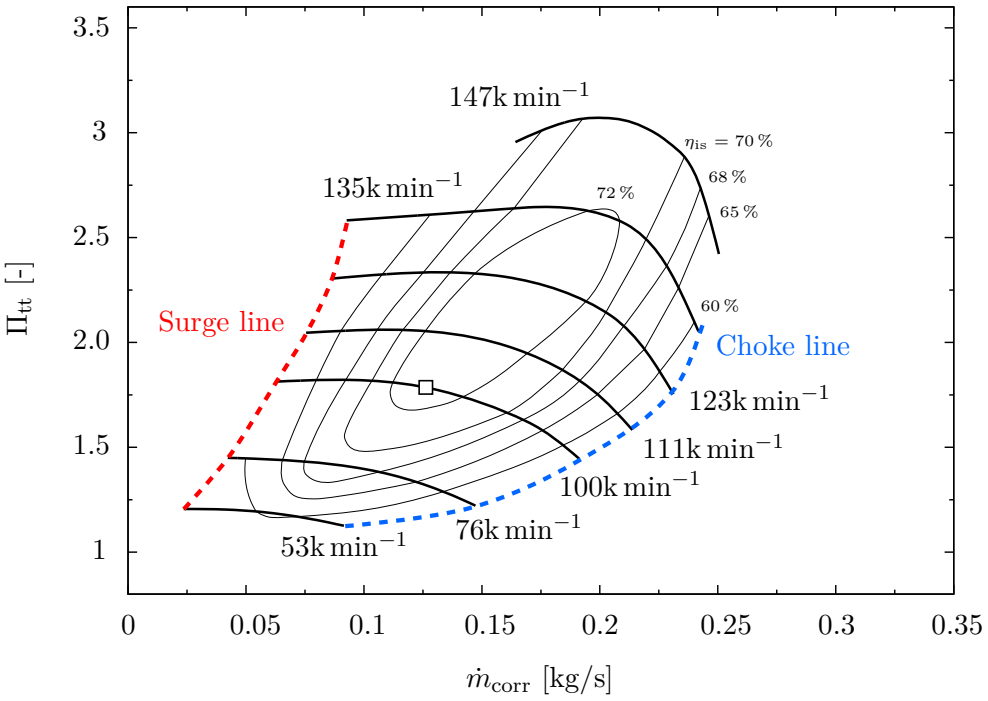

Figure 5.2: Measured performance map of the centrifugal compressor with the design point (□).

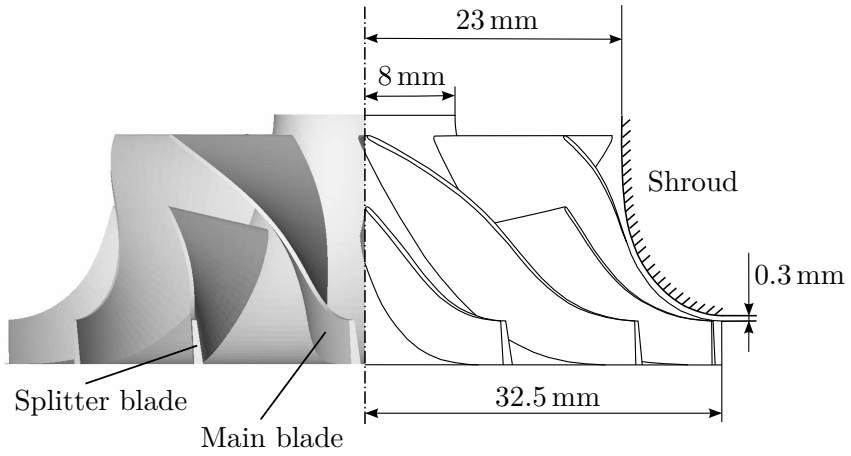

Figure 5.3: Geometry of the compressor wheel.

The compressor wheel is made of G-TiAl6V4, a titanium cast alloy. It has a very good ratio between strength and density and also a good cast capability (see Hesse [45] for detailed material properties). The low density of $4.45\,\mathrm{g/cm^3}$ makes it ideal for the compressor wheel since the moment of inertia is lower compared to steel. This is in particular important at varying loads. Industrial standard for manufacturing compressor wheels is milling. This enables a large freedom in geometry and offers a very good finishing. According to Jasni and Lajis [55], the equivalent sand grain roughness of a TiAl alloy processed by a milling machine is less than $k_s < 1\,\mu\mathrm{m}$. For this reason, the surface roughness of the compressor wheel can be neglected in the simulations.

The baseline compressor housing consists of EN-GJSA-XNiSiCr35-5-2, an austenic cast iron with spheroidal grafite form. This material is often used in high temperature environments such as exhaust manifolds and turbocharger housings. This is due to the high temperature strength and low thermal expansion (see e.g. Berns and Theisen [11] for detailed material properties). The surface roughness of the housing depends on the production method. Since no roughness measurements were conducted, it is assumed that die casting is used for manufacturing larger quantities. DIN 4766 [30] states a surface roughness of $R_z = (1 - 10)\,\mu\mathrm{m}$ for die casting. Although withdrawn, this DIN standard still provides a valuable guideline for the expected roughness. Using the following correlation of Adams et al. [3]:

$$k_s = 0.978\,R_z\ , \tag{5.1}$$

one can calculate the equivalent sand grain roughness. Based on the dimensionless equivalent sand grain roughness k_s^+ and the definitions of flow regimes after to Schlichting and Gersten [86], the roughness has a neglectable influence on the volute flow.

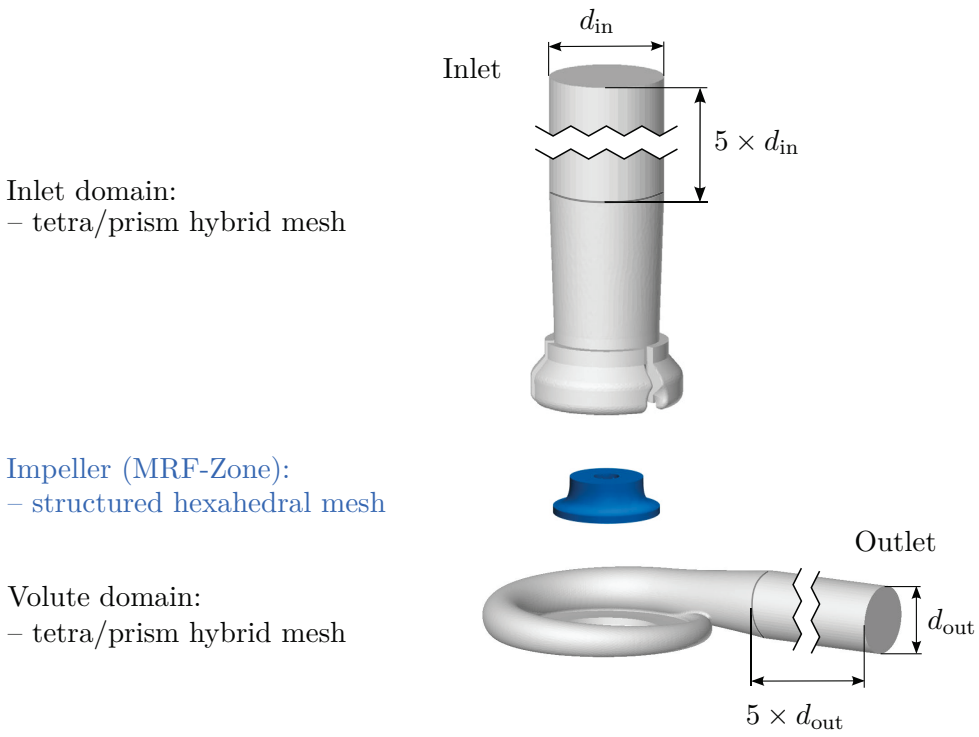

Figure 5.4: Computational domain of the centrifugal compressor.

5.2 Numerical Model

5.2.1 Geometry and Mesh

The computational domain is divided into three regions (see Figure 5.4). The inlet and volute domain are meshed using a tetrahedral/prism hybrid mesh. The reason for this is the complex geometry which makes it difficult to use block-structured meshes. Furthermore, local mesh refinement is easily feasible. The impeller is meshed using a block structured hexahedral mesh. This results in a lower cell count and higher accuracy. The mesh is locally refined at crucial regions, such as leading edge of the impeller blades (see Figure 5.5), the tip clearance and the tongue of the volute. All three domains are connected using arbitrary mesh interfaces. These allow the use of non-conformal grids at the interfaces and reduce the meshing expense. A direct interpolation is used at these boundaries between all domains. This way, pressure distortions upstream the vaneless diffuser are transported downstream. Therefore, a better prediction of the flow inside the volute can be made. This is in contrast to

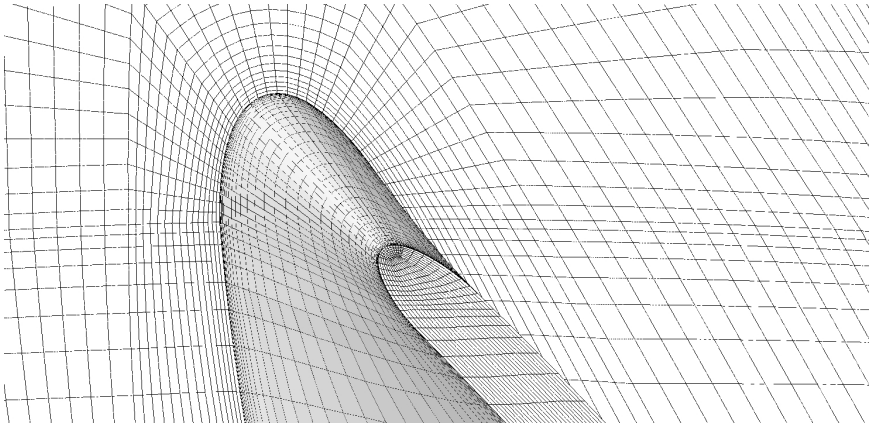

Figure 5.5: Surface mesh resolution at the leading edge of the splitter blade for the finest mesh.

Table 5.1: Cell count for the grid dependency study and average non-dimensional wall distance $\bar{y}^+$ for the near-wall cells.

Mesh region	Cell count $\times 10^6$				$\bar{y}^+$
	Coarse	Normal	Fine	Very fine	
Inlet	0.49	0.72	0.96	1.50	24
Impeller	1.00	1.50	2.00	3.00	16
Volute	0.52	0.76	0.99	1.48	24
$\sum$	2.01	2.98	3.95	5.98	

a mixing plane approach, where fluctuations are dampened due to circumferential averaging at the interfaces. However, this approach would require less computational resources.

Four different meshes where used in order to investigate the mesh dependency of the numerical model (see Table 5.1). The mesh size is between $(2.01 - 5.98) \times 10^6$ cells. About 50 % of all cells are located inside the compressor wheel part due to the complexity of the flow. The average dimensionless near-wall distance $\bar{y}^+$ is nearly constant for each mesh with 24 for the inlet and volute region and 16 for the impeller.

The turbocharger inlet and outlet have a diameter of 65 mm and 42 mm, respectively. The inlet pipe upstream the ported shroud and the outlet pipe downstream the volute are extended using an extrusion mesh in order to reduce the influence of the inflow

Table 5.2: Inlet and outlet boundary conditions.

Inlet	p_{tot}	101.3 kPa
	T_{tot}	297 K
	I_t	10 %
	L_t	5 mm
Outlet	p	varying
	others	zero gradient

and outflow boundary conditions onto the main flow. Due to this extrusion, the inlet and outlet boundary patches match with the measurement positions of the text bench. This increases the comparability between simulation and experiment. Some geometry simplifications are made to reduce the complexity of the meshing process and obtain accurate results in a reasonable time frame. Firstly, the fillet radius between the blades and the hub of the compressor wheel is neglected. This increases the simulated flow cross-sectional area in the impeller by about 2 %. Secondly, the gap between the compressor wheel and the diffuser is ignored. For that reason, the influence of the backside cavity of the impeller cannot be modeled.

5.2.2 Boundary Conditions and Initialization

The boundary conditions are chosen to approximate the test bench measurements. The total pressure at the inlet is set to 101.3 kPa with a total temperature of 297 K. The turbulent intensity is estimated to be 10 % with a turbulent length scale of 5 mm. This corresponds to a fully developed turbulent flow. At the outlet, a target mass flow is defined which depends on the operating point of the compressor. Other variables at the outlet are treated as zero gradient. The walls are defined as no-slip, adiabatic, and surface roughness is neglected. The boundary conditions are summarized in Table 5.2.

Three different rotational speeds n are analyzed: 53 000 min^{-1}, 100 000 min^{-1}, and 123 000 min^{-1}. For stability reasons, the models are initialized at rest with a total pressure ratio of one. During the first 100 iterations, the angular velocity of the

impeller is gradually increased to their designated values. This significantly increases the stability of the simulations.

The Multiple Reference Frame (MRF) model is used to account for the rotation of the compressor wheel. For this approach, the domain is divided into inertial and rotating regions. In the rotating region, additional terms in the governing equations model the influence of the moving rotor. The MRF model does not account for the relative motion of a moving zone with respect to adjacent zones, e.g. the mesh remains fixed in space for the computations.

Steady-state simulations are run until a converged solution is achieved. Thereby, the numerical results can give an accurate performance prediction for the design point and the choke limit. This way a major part of the performance map can be investigated. Oscillations in the flow patterns indicate an unstable operating point. This is particularly the case for low mass flow rates in combination with high pressure ratios, where rotating stall leads to temporal fluctuations of the mass flow. This could finally lead to a complete breakdown of the compressor operation, called surge (see Schobeiri [87]). These unstable fluctuations cannot be resolved with the steady-state approach in this model and are therefore not part of this simulation. The solution convergence is evaluated by calculating the total pressure ratio and isentropic efficiency at each iteration. Convergence is achieved, when the monitored quantities reach a constant value. In case of unsteady behavior or oscillations, the flow field is averaged over the iterations and the mean field is used for postprocessing.

5.3 Results

5.3.1 Grid Dependency Study

The influence of the different grid resolutions is shown in Figure 5.6. The total pressure ratio as well as the isentropic efficiency are plotted for a cell count of $(2.01 - 5.98) \times 10^6$. The simulation represent the measured total pressure ratio well and the slopes are met very well. The reference values are overestimated by approximately 5 %. The influence of the cell count is minor. However, the coarse and normal mesh show slightly lower pressure ratios at high and low flow rates compared to the fine and very fine

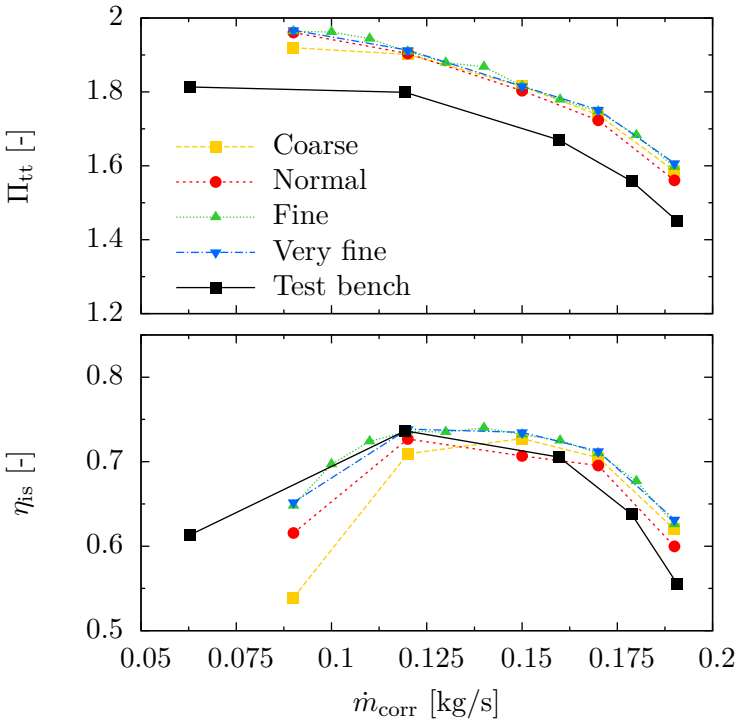

Figure 5.6: Total pressure ratio and isentropic efficiency for different mesh sizes at $n = 100\,000\,\mathrm{min}^{-1}$.

mesh. Similar results can be seen at the isentropic efficiency. The coarse and normal meshes show a significant drop in efficiency and strongly underpredict the test bench measurements. One can suspect that the coarse grids cannot resolve the complex flow inside the compressor sufficiently leading to additional losses. Again, the fine and very fine mesh offer similar results. This indicates that a mesh resolution of 4×10^6 cells is sufficient for an almost mesh independent solution. Therefore, the fine grid is used for further investigations of the compressor. It offers the best compromise between accuracy and computational cost.

5.3.2 Effect of the Rotor Position

Depending on the geometry of the radial diffuser and the volute, the position of the rotor with respect to the tongue could influence the results of the simulation. The reason is that steady-state simulations with MRF approach model a compressor wheel fixed in space. Therefore, an unfavorable orientation could possibly lead to erroneous

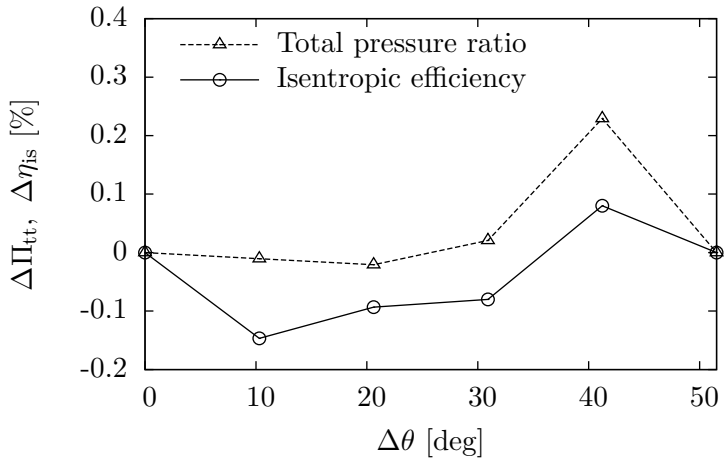

Figure 5.7: Influence of relative rotor position $\Delta\theta$ onto the total pressure ratio and isentropic efficiency at design conditions.

results. This could be the case when a jet from a blade channel impacts the tongue and causes an exaggerated flow separation in the exit diffuser. In order to investigate this effect, the compressor is simulated using four additional relative blade positions: 10.28°, 20.57°, 30.86°, and 41.14° with regard to the orientation of the baseline model. An angle of 51.42° would result in the original geometry due to rotational symmetry.

The relative change of the Π_{tt} and η_{is} at design conditions as a function of the rotor position can be seen in Figure 5.7. The highest influence can be found in the total pressure ratio at an angle of 41.14°. Based on a difference between experiment and simulation of up to 5 %, this effect is negligible with a relative error of less than 0.25 %. The Mach number contour plots at the center of the radial diffuser height (Figure 5.8) show the development of the jets downstream the compressor wheel and inside the volute channel. Although different blade positions result in shifted jet locations, the flow field inside the volute and the axial diffuser is barely effected. This shows that the rotor position has a minor effect in the numerical model. This is due to the large diameter ratio of the radial diffuser between impeller exit and volute inlet. This smooths the local flow field fluctuation of the jets resulting in more homogeneous flow conditions at the volute inlet.

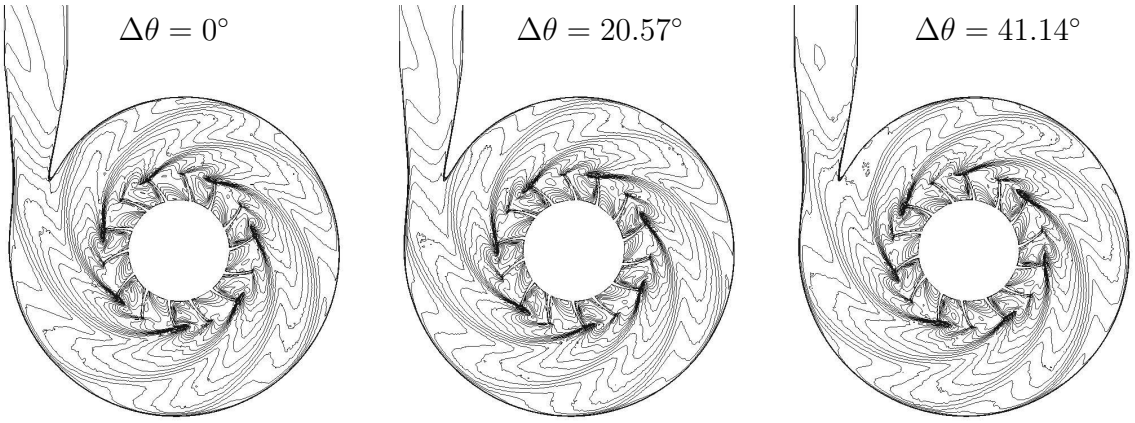

Figure 5.8: Mach number contour plots for different impeller positions at design conditions.

5.3.3 Validation with Experimental Results

The total pressure ratio for the turbocharger for three different rotational speeds using the proposed numerical model in OpenFOAM is presented in Figure 5.9 (top). In general, all simulation results show a good accordance to the test bench measurements. Similar to the Radiver centrifugal compressor test case, the total pressure ratio is overpredicted for all operating conditions. The difference is small at lower angular velocities with less than 3 % at $n = 53\,000\,\mathrm{min}^{-1}$. However, the total pressure ratio at the higher speeds is overestimated by up to 6 %. Nevertheless, the trends of the performance map is computed very well and the choke limit is predicted correctly. Figure 5.9 (bottom) shows the isentropic efficiency as a function of the mass flow rate for four different rotational speeds. The isentropic efficiency is computed well for rotational speeds close to design point. However, the curves are shifted slightly to higher flow rates. The highest efficiency is predicted to be at 0.15 kg/s rather than 0.12 kg/s as measured in the experiments.

The simulations are repeated for $n = 100\,000\,\mathrm{min}^{-1}$ with the commercial CFD code ANSYS Fluent. The numerical setup is similar to the one presented in section 4.2. This way, the accuracy of the proposed numerical model can be assessed better. The performance map in Figure 5.9 shows that ANSYS Fluent offers an identical total pressure ratio compared to the OpenFOAM model. However, the isentropic efficiency is higher by about 2 %. Nevertheless, the slopes are very similar as well. This indicates

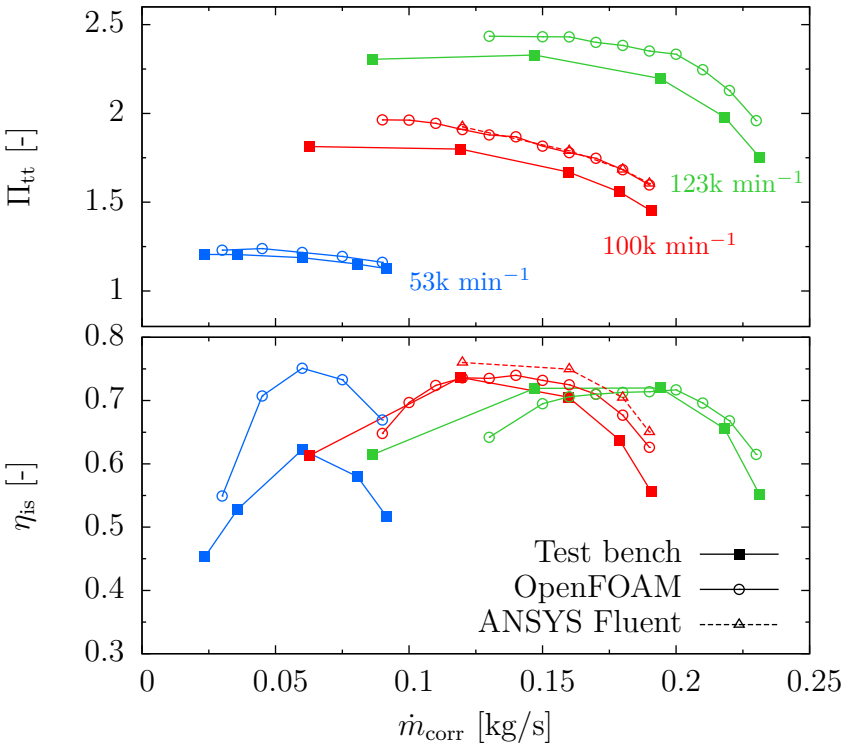

Figure 5.9: Total pressure ratio Π_{tt} and isentropic efficiency η_{is} for the OpenFOAM and ANSYS Fluent simulations and test bench measurements.

the good accuracy of the density-based solver, which is on par with current commercial solvers.

Sources for the differences between experiment and simulation are diverse such as geometry and modeling simplifications. The fillet radius between the blade and the hub is neglected. This increases the effective cross-sectional area and thus allows higher flow rates. According to Sun et at. [94], the flow in the impeller backside cavity causes additional losses in efficiency and total pressure ratio of about 1 %. This effect is also not captured in the simulations. Another source of error is the lack of real mesh movement. That implies, blade passage effects are not resolved.

The isentropic efficiency for low speeds is significantly overestimated. According to Bohn et al. [13], this can be attributed to the heat transfer from the turbine side of the turbocharger. This heat transfer is mainly composed of heat radiation from the hot surface and heat conduction via the housing and the shaft that connects the turbine and

the compressor wheel (see Verstraete et al. [103]). This additional heat input increases the compressor air outlet temperature and reduces the efficiency. The main reason for these differences is the definition of the walls as adiabatic. This suppresses the heat transfer to the surroundings, implying a higher ambient temperature. Therefore, the computed outlet gas is hotter than the experimental data leading to a lower isentropic efficiency.

A similar effect is noticeable at high angular velocities, where fluid temperatures reach up to 475 K. In these cases, the heat transfer to the environment and inside the housing material results in a lower outlet temperature compared to the simulation model and therefore higher efficiencies. The numerical results could be improved by including the conjugate heat transfer to the housing, the environment and the turbine side. Unfortunately, no geometry and thermal boundary conditions are available for the turbine side of the turbochargers. For this reason, these more sophisticated simulations cannot be conducted.

Operating points close to the surge cannot be resolved using the presented model. Hellstrom et al. [44] characterized the flow near stall as dominated by highly unsteady flow separation at the rotor as well as reversed in the inlet region and ported shroud. These effects cannot be resolved using a steady-state simulation. Furthermore, Baris and Mendonca [10] argue that wall-function RANS-based simulation fails to predict flow separation, which is characteristic for low mass flow regimes. In addition, the numerical model suffers from the turbulence modeling, which has been discussed in the Radiver centrifugal compressor test case.

5.3.4 Influence of a Simplified Model

Considering the high computational cost of an optimization, a simplified numerical model could reduce the required time for the simulations. In order to investigate this potential benefit, a model of the volute only is created. This way, the inlet and the compressor wheel are not taken into account and the cell count is reduced by approximately 75 %. However, effects upstream the volute are not captured in this simulation. The inlet of the model is located at the impeller exit. Mass-weighted averaged values are defined at this position for the total pressure and total temperature

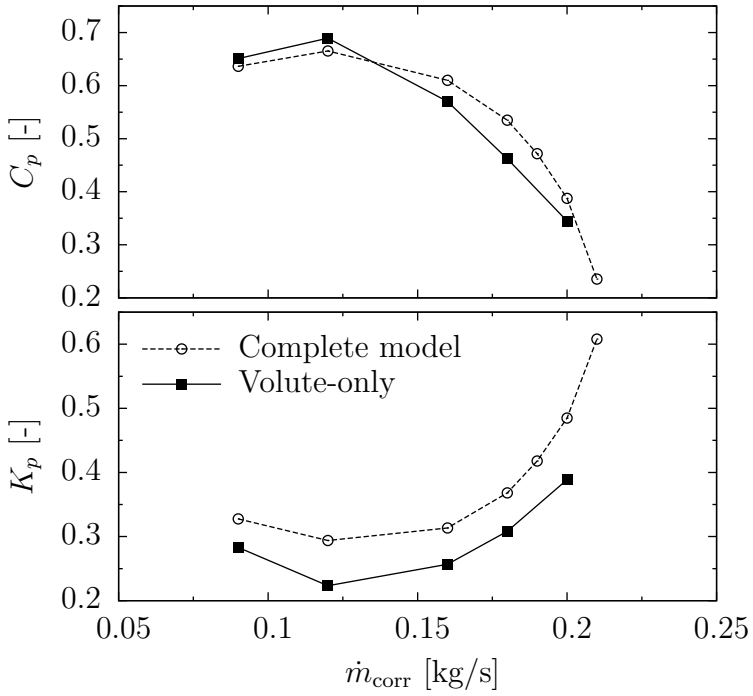

Figure 5.10: Static pressure recovery C_p and total pressure loss coefficient K_p of the volute for the complete and the volute-only model at $n = 100\,000\,\mathrm{min}^{-1}$.

as well as for the turbulent quantities. Furthermore, the velocity angle is set. The static pressure is varied at the outlet to reach the designated flow rates. These boundary conditions are extracted from the complete compressor model. Total pressure ratio and isentropic efficiency cannot be used for comparing the volute flow of both models. Therefore, the static pressure recovery and the total pressure loss coefficient are considered instead.

Figure 5.10 shows these coefficients as a function of the corrected mass flow rate at $n = 100\,000\,\mathrm{min}^{-1}$. Unfortunately, no measurements are available at the impeller exit. For this reason, no experimental data is available for comparison. The location of highest pressure recovery and lowest pressure losses for both models coincide well with the global maximum isentropic efficiency. At higher mass flow rates, the velocity increases and therefore the losses due to friction. At low flow rates, Hagelstein et al. [39] and Gu et al. [38] state that flow separation in the volute or the axial exit diffuser lead to higher losses.

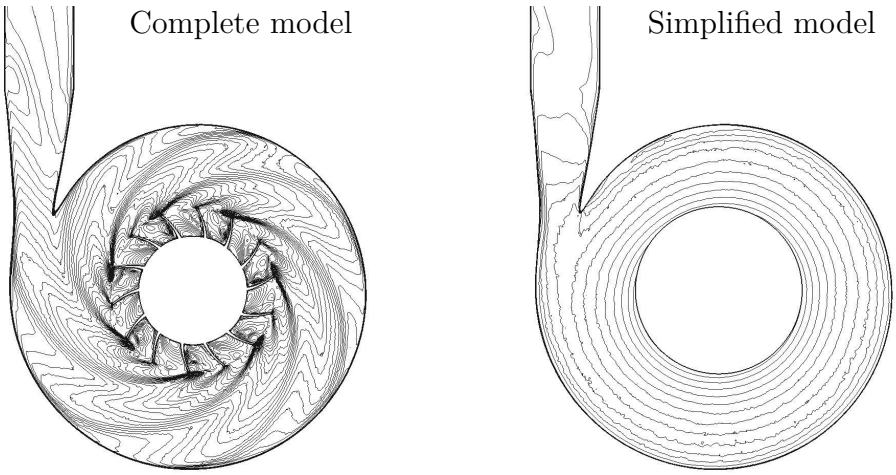

Figure 5.11: Comparison of Mach number contour plots at midspan diffuser of the complete model (left) and the simplified numerical model (right) at design point.

Comparing both models reveals significant differences between the complete compressor model and the simplified volute-only model. Firstly, the total pressure loss coefficient is significantly underestimated by the volute-only model. This indicates that losses inside the vaneless diffuser and the volute are not resolved properly. Secondly, the slopes do not match for the static pressure recovery coefficient. The main reason for these differences are the circumferential averaged boundary conditions at the impeller exit, which simplify the inlet flow into the volute and suppress any impeller-volute interaction. This effect is shown at design point in Figure 5.11. Jets formed by the blade channels are not resolved in the simplified model. Furthermore, separation at the shroud downstream the impeller is avoided due to averaging, which results in a lower pressure loss.

These findings can be compared to a study conducted by Chen and Li [23]. They performed a design of experiment to develop a more compact volute housing. Their conclusion is that a volute-only simulation is significantly faster. However, it can only be used to predict the general trend rather than absolute values and detailed flow fields. Due to these limitations, the volute-only model is discarded and the complete compressor model is used for the optimization. This way, the local flow field can be predicted correctly and more comprehensive results can be obtained.

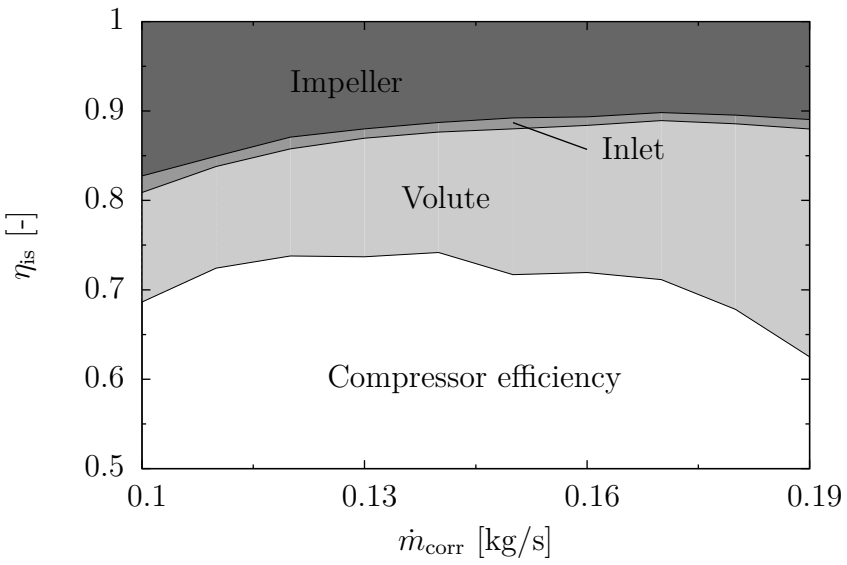

Figure 5.12: Reduction in isentropic efficiency for each component of the centrifugal compressor at $n = 100\,000\,\mathrm{min}^{-1}$.

5.3.5 Efficiency of each Compressor Part

The losses inside the compressor are comprised of three parts: losses inside the compressor wheel, inlet including ported shroud, and volute. These individual contributions are shown in Figure 5.12 based on the compressor efficiency at a rotational speed of $100\,000\,\mathrm{min}^{-1}$. The complete compressor efficiency is slightly above 70 % at large portions of the performance curve and falls to 62 % at higher mass flow rates. Losses inside the inlet are constant at about (1 – 2) % of the total losses. This contribution is negligible compared to the compressor wheel and the volute. At low flow rates, the efficiency reduction inside the impeller dominates with a share of about 18 %. This amount is reduced down to 10 % at higher flow rates. In contrast, the losses inside the volute prevail at high flow rates with values of about 66 % of all losses inside the compressor.

These numbers indicate that efficiency reduction inside the volute is of the same order of magnitude as in the compressor wheel. Therefore, an optimization of the volute and the consequent reduction of losses is a viable and promising way to increase the overall compressor efficiency.

6 Genetic Optimization of the Volute Shape

The volute of the centrifugal compressor from the previous chapter is used as a case study for a genetic optimization. This chapter presents the C++ program for the automated generation of the volute geometry, the meshing process, and the genetic algorithm for the geometry optimization. The results of this optimization are shown and the improvements compared to the baseline model are discussed with respect to the geometry changes and the flow physics inside the volute.

6.1 Automated Volute Geometry Generation

One essential requisite for a numerical optimization is the automated geometry and mesh generation. This is due to the large number of function evaluations and thus numerical simulations necessary for genetic optimization. In particular, the geometry creation is challenging in case of a volute. In contrast to blades which can be parametrized easily, the creation of a volute geometry is much more complex. This is due to the non-symmetrical and fully three-dimensional character. Its size and shape depends on the cross-sectional area A_{vc} and the circumferential angle θ. Furthermore, tongue is very difficult to model. This part results from the intersection between the volute and the axial diffuser and has to be calculated for each volute geometry individually.

For these reasons, a design program for the automated generation of the volute geometry is developed. It is written in the object-oriented programming language C++. The settings and geometry input parameters are controlled using text files,

which makes it suitable for scripting. Furthermore, the tool can be coupled easily with simulation software and the creation of the geometry is completely automated and does not require any additional user intervention. Thus, it is ideal for parameter studies, uncertainty quantification and optimization.

Due to the elaborate shape of the volute, simple polynomial functions are not sufficient for the design. Likewise, the linear combination of basic geometric shapes does not give the variety needed for an optimization and cannot represent typical industrial designs. For this reason, B-splines are employed to represent and parameterize the radial diffuser downstream the compressor wheel and the volute surface. These curves offer a large range of geometric freedom while making use of only a few parameters.

6.1.1 Mathematical Definition of B-Splines

A basis spline (B-spline) is a piecewise polynomial function of degree k in a variable t (see Patrikalakis and Macaw [82]). Such a curve $\underline{C}(t)$ is defined as linear combination of $n+1$ control points $\underline{p}$ and a B-spline basis function $N_{i,k}(t)$ given by:

$$\underline{C}(t) = \sum_{i=0}^{n} \underline{p}_i N_{i,k}(t) \ , \qquad t_{k-1} \leq t < t_{n+1} \ . \tag{6.1}$$

The basis function is defined on a knot vector containing $m+1$ elements in nondecreasing order $\underline{T} = (t_0, t_1, \ldots, t_m)$ with $t_i \in [0,1]$. The function only depends on k and the elements of the knot vector are given by recurrence relations:

$$N_{i,1}(t) = \begin{cases} 1 & \text{if } t_i \leq t < t_{i+1} \\ 0 & \text{otherwise} \end{cases} \ , \tag{6.2}$$

for $k = 1$, and else:

$$N_{i,k}(t) = \frac{t - t_i}{t_{i+k-1} - t_i} N_{i,k-1}(t) + \frac{t_{i+k} - t}{t_{i+k} - t_{i+1}} N_{i+1,k-1}(t) \ . \tag{6.3}$$

This results in a polynomial of degree k on each interval $t_i < t < t_{i+1}$. The degree of the spline must be at least one, which results in a linear curve and cannot be greater than $n+1$. Figure 6.1 shows the influence of the degree onto the spline. A higher

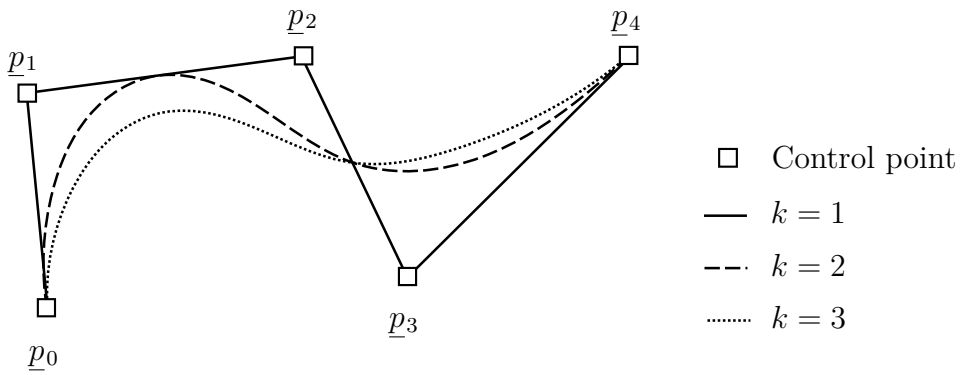

Figure 6.1: Different B-spline curves based on the degree k using five control points.

degree results in a smoother spline while increasing the average distance between the curve and the control points.

If the first and last control point should be on the B-spline, the first and last $k + 1$ knots have to be equal. The relation between the number of control points, knots, and degree of a spline is given as $m = n + k + 1$. As an example, the curve of degree three in Figure 6.1 with five control points has to have nine knots in total with

$$\underline{T} = (0, 0, 0, 0, 0.5, 1, 1, 1, 1) \ . \tag{6.4}$$

B-splines cannot represent some simple curves such as circles and ellipses. To form these shapes, a generalization of B-splines is necessary, such as non-uniform rational basis spline (NURBS). However, NURBS require a weighting factor for each control point. This additional parameter increases the variation for each curve. As a consequence, the parameter space of all possible geometry combinations would grow significantly resulting in higher computational cost for the optimization. Therefore, the volute generation is limited to B-splines to keep the number of possible parameters manageable.

6.1.2 Geometry Generation and Meshing

The geometry downstream the compressor wheel consists of three parts: the radial diffuser, the volute, and the axial diffuser. The basic layout can be seen in Figure 6.2 including the definition of the volute channel and the position of the volute inlet and

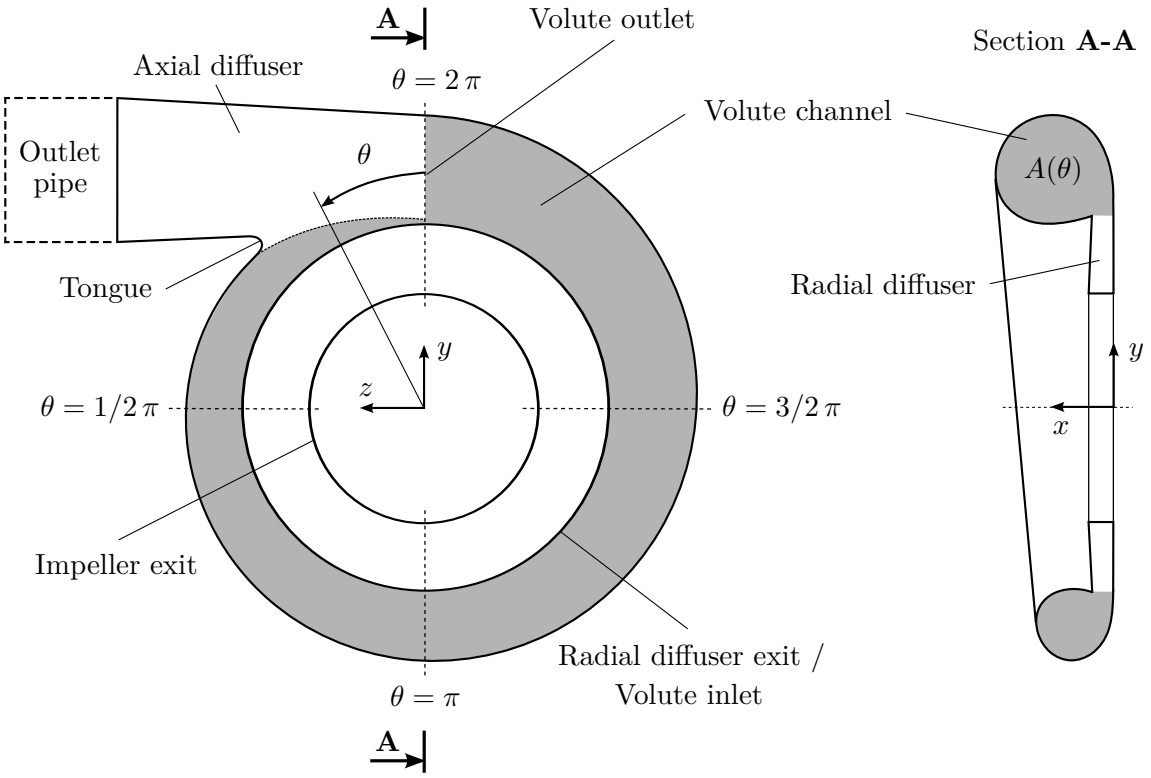

Figure 6.2: Definition of the volute geometry in top-down view (left) and section view through **A-A** (right).

outlet. An important variable to describe the model is the circumferential angle θ. It starts at the position with the lowest volute cross section area and reaches 2π at the volute outlet in counterclockwise direction. Eleven parameters in total can be varied to design the geometry of the three parts (see. Tab. 6.1). Some of them are simple scalars, such as the axial diffuser length, others can be defined via B-splines, such as the volute cross-section area distribution. Using these parameters for the volute generation, one can modify each of the five geometric specifications, which impact the volute performance as introduced in section 2.3: shape, area and radial location of the volute channel, location of the volute inlet, and tongue geometry.

However, an optimization including all five specifications is much too complex to solve. Therefore, this optimization is focused on the influence of the shape of the volute, the radial location of the volute channel, and the inlet location. These three can be investigated by modifying the B-spline for the volute cross-sectional shape. The cross-sectional area and the tongue geometry are kept constant and are adopted from

Table 6.1: User-definable geometric parameters for the volute generation.

Part	Parameter	Type
Radial diffuser	Impeller exit height	Scalar
	Impeller exit radius	Scalar
	Lower radial diffuser shape	B-spline
	Upper radial diffuser shape	B-spline
	Radial diffuser exit height	Scalar
	Radial diffuser exit radius	Scalar
Volute	Volute cross-sectional shape	B-spline
	Volute area distribution	B-spline
Axial diffuser	Diffuser length	Scalar
	Diffuser outlet area	Scalar
	Tongue fillet radius	Scalar

the baseline compressor model. In the following, the settings for the different geometry parameters are explained and the geometry generation process is illustrated.

The radial diffuser downstream the compressor wheel is geometrically defined by the impeller exit radius and height. In case of the centrifugal compressor under investigation, this is 32.5 mm and 4.3 mm, respectively. The lower and upper radial diffuser wall are shaped using B-splines. This way, the geometry is not limited to planar walls. However, the radial diffuser for the optimization is simplified with plane, tapered walls. The radial diffuser exit radius and height is set to 55 mm and 4 mm, respectively.

The cross-sectional shape of the volute is represented by B-splines. Eight control points are used in combination with a third degree spline to represent the cross-sectional shape of the volute (see Figure 6.3 (left) for three examples). By altering the coordinates of these points, the shape of the spline and as a result the volute surface changes. Therefore, a wide range of different geometries can be assembled due to the flexibility of B-splines. More complex shapes could be achieved by adding control points to the spline. However, their number is a trade-off between the geometric freedom of possible shapes and the number of adjustable parameters for the optimization. The

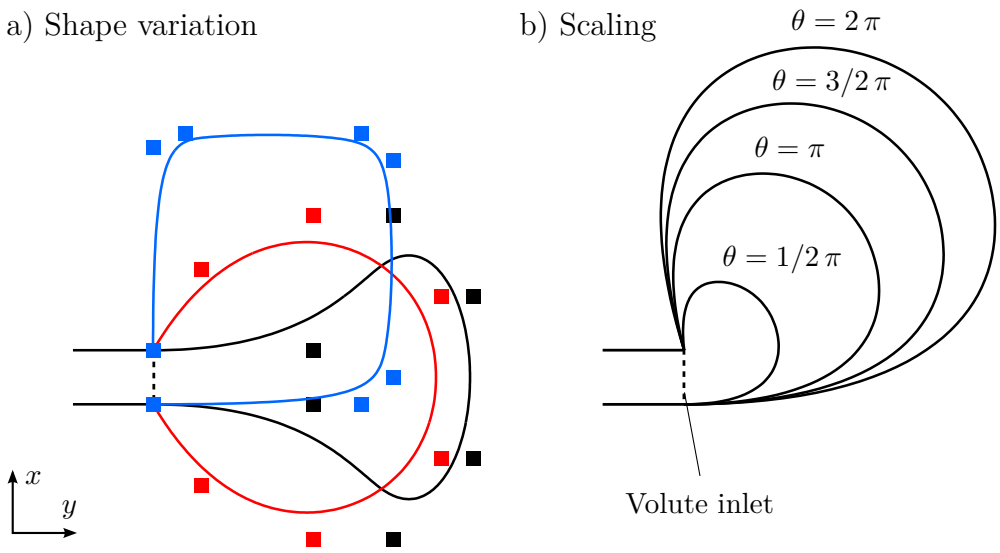

Figure 6.3: Three different volute shapes represented by B-splines using eight control points (left) and scaling of the volute shape cross-sectional areas as a function of the azimuthal angle θ (right).

more control points, the more complex and computational expensive the optimization will be. For this reason, eight control points is a good compromise.

The cross-sectional area of the volute channel is a function of the circumferential angle θ. This function is defined by a spline. Therefore, non-linear area distributions can be modeled. In order to match a specific cross-sectional area, the volute shape is scaled based on θ as shown in Figure 6.3 (right). In order to change the size, the control points are shifted towards the volute inlet. This way, the basic geometrical shape is preserved while adjusting the size of the volute channel. Based on the existing compressor model, the circumferential volute area distribution is simplified as linear with a volute exit area of $735\,\mathrm{mm}^2$.

The third part of the volute is the axial diffuser defined by its length of 80 mm and opening angle of 7°. It connects the volute outlet with the outlet pipe. There is a smooth transition between the volute outlet and the circular outlet pipe to avoid separation and pressure loss due to a discontinuous surface. The tongue of the volute is formed using a fillet with a radius of 4 mm.

The developed automated generation of the volute can be summarized in four steps, which are shown in Figure 6.4. (1) At first, the geometrical parameters are read

(1) Initial spline generation at $\theta = 2\,\pi$

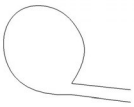

(2) Duplicated and rotated splines

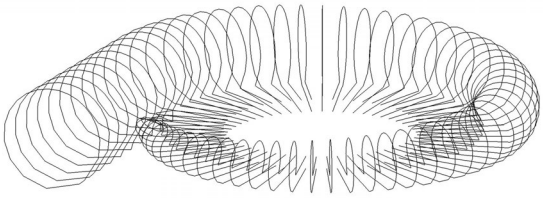

(3) Surface mesh with sharp tongue

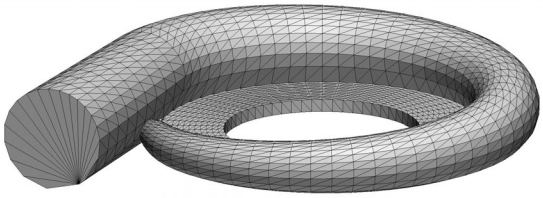

(4) Smooth surface with rounded tongue

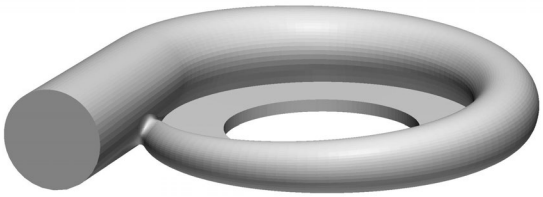

Figure 6.4: Steps of volute geometry generation after reading the parameters. The surface mesh and spline representation are simplified for better illustration.

from the settings files. This includes information about the geometry, the splines (e.g. control points, degree), and the spatial resolution of the surfaces. Then, the splines for the upper and lower wall of the radial diffuser and the volute cross-section are created at $\theta = 2\,\pi$. In order to avoid invalid volute shapes, a check for self-intersection is performed. (2) The volute splines are duplicated, rotated in circumferential direction with respect to the rotation axis of the compressor wheel and their size is adjusted to match the volute cross-section area. Additionally, the axial diffuser is extruded from the volute exit shape and morphed in axial direction to form a circular diffuser exit. (3) Based on this, a surface mesh is created for each part of the volute. (4) The tongue is generated by calculating the intersection between volute and axial diffuser surface and forming a smooth fillet. Finally, the surfaces are written in STL format (stereo lithography) to the hard drive for further preprocessing. The complete process takes less than one minute, which makes it ideal for generating large numbers of geometries.

The open-source meshing tool `snappyHexMesh` is used for the volume mesh generation of the volute. Figure 6.5 shows a cross-sectional view of a sample geometry. This program automatically creates an unstructured hexahedral mesh based on the STL

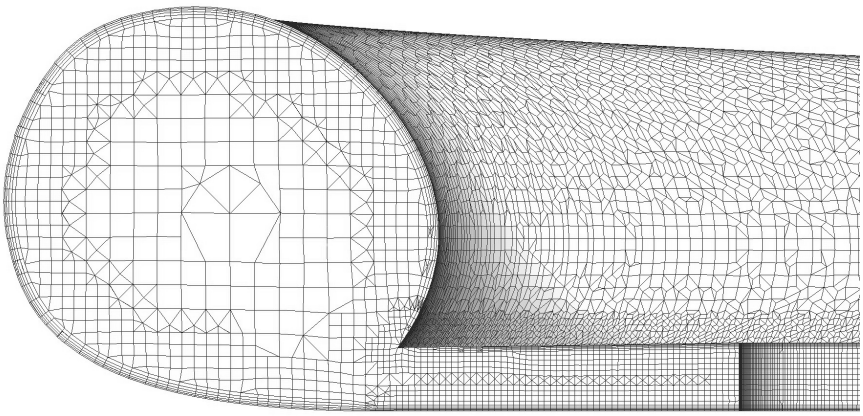

Figure 6.5: Slice of the unstructured hexahedral-dominant mesh with prism layers automatically generated using `snappyHexMesh` at the volute exit.

surfaces as input geometries. For this reason, it interacts very well with the automated geometry generation since no user input is necessary after the initial setup. In order to ensure a proper surface mesh, files containing the definition of the cutting edges are created during the geometry creating process. This geometry information is used to create a high-quality mesh around sharp corners and edges. Five prism cells are used to model the boundary layer at the walls with an growth ratio of 1.2 between the layers. The average y^+ value is about 24. Finally, an extrusion mesh is added to form the outlet pipe. Its length is five times the pipe diameter to match the measurement position of the reference model. The total cell count for the volute mesh is approximately 1 million, which is in line with the mesh dependency study of the complete turbocharger in section 5.3.1. However, the total element number of the volute may vary slightly due to different shapes.

6.2 Genetic Optimization

Genetic optimization is a numerical optimization approach utilizing genetic algorithms (also known as evolutionary algorithms) to minimize or maximize a function object $f(\underline{x})$ with $\underline{x} \in \mathbb{R}$ (see Gill et al. [37]). These algorithms are based on Darwin's theory of survival of the fittest [26]. In this formulation,

$$\underline{x} = (x_1, x_2, \ldots, x_n) \ , \tag{6.5}$$

is a n-dimensional vector of design parameters or design variables. These are bound to constraints, which define the valid values for the elements of $\underline{x}$. The constraints can have different types, such as

- lower $\underline{x}_L$ and upper $\underline{x}_U$ bounds of $\underline{x}$,
- nonlinear equality constraints $\underline{h}(\underline{x}) = \underline{h}_{\text{tar}}$ with a target value $\underline{h}_{\text{tar}}$,
- nonlinear inequality constraints $\underline{g}(\underline{x})$ with lower $\underline{g}_L$ and upper $\underline{g}_U$ bounds of $\underline{g}$.

The size of all possible values for $\underline{x}$ is called design space or parameter space. If a specific design satisfies all constraints, it is marked as feasible; otherwise, as infeasible. This results in the following mathematical model for an optimization:

$$\begin{aligned} \text{minimize:} \quad & f(\underline{x}) \\ & \underline{x} \in \mathbb{R} \\ \text{subject to:} \quad & \underline{x}_L \leq \underline{x} \leq \underline{x}_U \\ & \underline{h}(\underline{x}) = \underline{h}_{\text{tar}} \\ & \underline{g}_L \leq \underline{g}(\underline{x}) \leq \underline{g}_U \ . \end{aligned} \tag{6.6}$$

Genetic algorithms offer the advantage of a global search. Therefore, they use the complete parameter space to find the optimized solution and are less likely to get stuck in local extrema. Unlike gradient-based methods, function objective derivatives are not needed during the genetic optimization process which results in more robustness and better parallel performance. However, genetic algorithms suffer from slower convergence rates and require more function evaluations and thus computational power to find the optimal solution.

The analysis of the volute geometry is performed using the open-source software toolkit **D**esign **A**nalysis **K**it for **O**ptimization and **T**erascale **A**pplications (**Dakota**) (see Adams et al. [2]). This toolkit includes a genetic algorithm library COLINY (Common Optimization Library Interface), which is employed in the optimization. This algorithm consists of six different steps: Initialization, analyze and rank, selection, crossover, mutation, and termination. The flow chart of the algorithm is shown in Figure 6.6.

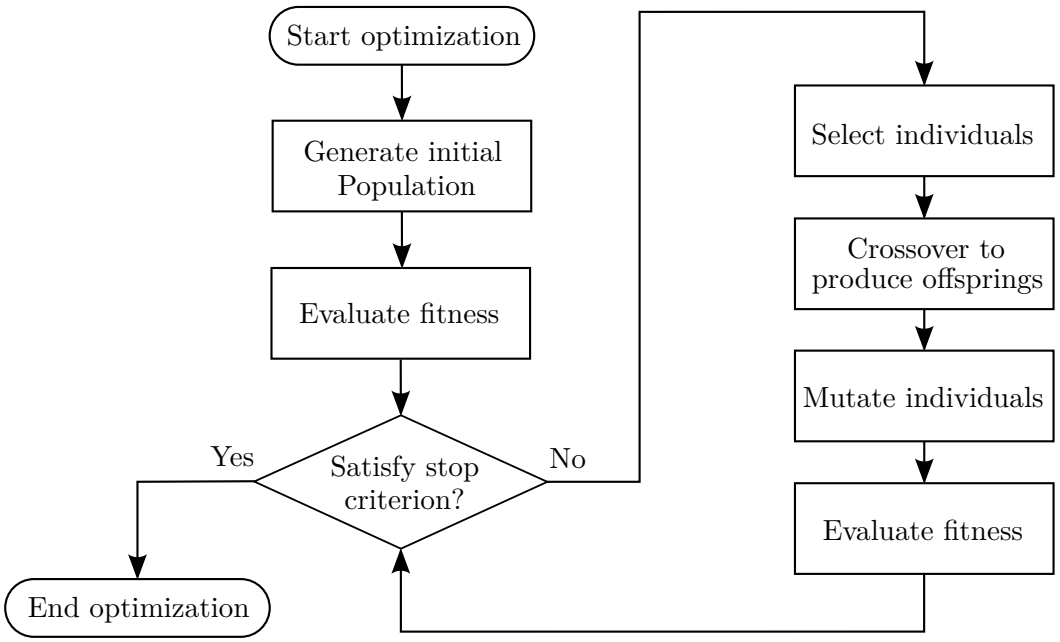

Figure 6.6: Basic steps of a genetic algorithm.

Initialization The optimization starts with an initial set of individuals. Each consists of a unique combination of design parameters called genome. The population of each iteration is called generation. Its size should be approximately five times the number of design parameters to reduce the chance of premature convergence to a local extrema. A diverse initial population increases the chance to find a good solution.

Analyse and Rank In each generation, the fitness of each individual in the population is evaluated and ranked. The fitness usually corresponds to the function object $f(\underline{x})$ which is determined from a CFD simulation of the corresponding individual. A merit function is used to scale the probability of selection based on the relative fitness within the current generation. Therefore, fitter individuals are more likely to be selected for the next generation.

Selection A new generation is created by choosing a certain number of best individuals from the existing generation. The rest of the generation is filled up with randomly chosen previous individuals utilizing the calculated merit function. Thus, at the same time favorable solutions and genetic diversity are maintained.

Crossover A proportion of the new population is selected to reproduce offsprings. Parent individuals are chosen randomly based on their fitness, where better solutions are favored. The child is created randomly along the multidimensional vector connecting the two parents and thus possesses the genome of both. The rate of crossover specifies the probability of a crossover operation being performed and therefore the number of offsprings. Crossover is used to vary and improve the genetic code from one generation to the next.

Mutation Mutation randomly alters a number of individuals by adding a Gaussian random amount to one or more of its design parameters. This amount is controlled by the mutation scale relative to the design parameter. The mutation probability specifies the chance of mutation for each individual. This genetic operator is used to maintain diversity from one generation to the next and to prevent the individuals from becoming to similar.

Termination The genetic optimization is continued until a solution has been found which satisfies a set of criteria, e.g. a maximum number of generation is reached, or until the solution fitness converges to a certain value and successive iterations no longer produce better results.

6.3 Numerical Optimization Setup

The workflow diagram of the numerical optimization is shown in Figure 6.7. It is separated in four parts: (1) Genetic optimization, (2) pre-processing, (3) numerical simulation, and (4) post-processing.

In the first step (1), the genetic algorithm creates a new generation consisting of 50 individuals. This number is a compromise between genetic diversity, and avoidance of premature convergence on the one hand and computational cost of the optimization on the other. The initial population consists of a wide range of volute shapes used in industry and randomly generated ones to create a large diversity at the beginning of the optimization. Figure 6.8 shows a sample of different geometries for the first population consisting of asymmetric (1 – 4) and symmetric shapes (5 – 7).

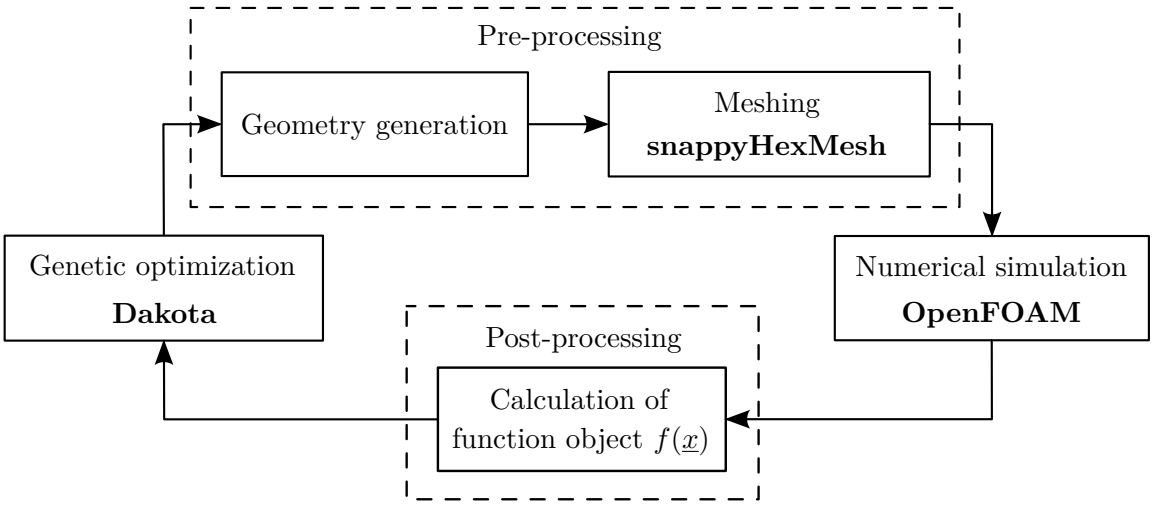

Figure 6.7: Workflow diagram of the genetic optimization.

The goal of the optimization is to maximize the objective function $f(\underline{x})$. It is defined as the algebraic average of the isentropic efficiency $\bar{\eta}_{\text{is}}$ of the centrifugal compressor at different mass flow rates. These flow rates are set to 0.12 kg/s, 0.15 kg/s, 0.17 kg/s, and 0.19 kg/s at a design speed of 100 000 min^{-1}. Thus, the volute is optimized for the design speed including several operating points rather than a single operating point. Since turbomachines rarely operate at design conditions, this approach is more comprehensive but also more time consuming. Even though the total pressure rise is an important characteristic of the compressor, it is not considered in the function object calculation. This decision is based on a statement of Baloni and Channiwala [8] that the volute takes no part in the energy transfer onto the fluid. Therefore, all considerations in volute design deal with loses. For this reason, a single objective optimization is assumed to be sufficient since a rise in isentropic efficiency also results in an increase total pressure. However, this assumption has to be verified during the optimization.

The setting for the genetic algorithm is as following. During the selection step, the ten best individuals are chosen to be passed to the next generation. The chance of a cross-over for a new individual is 80 % which results in approximately 40 offsprings per generation. The mutation rate is 30 % with a Gaussian deviation of 4 % based on the absolute value of the design parameter. Failed geometries or simulations result in a function object of zero and thus the removal from the genetic pool.

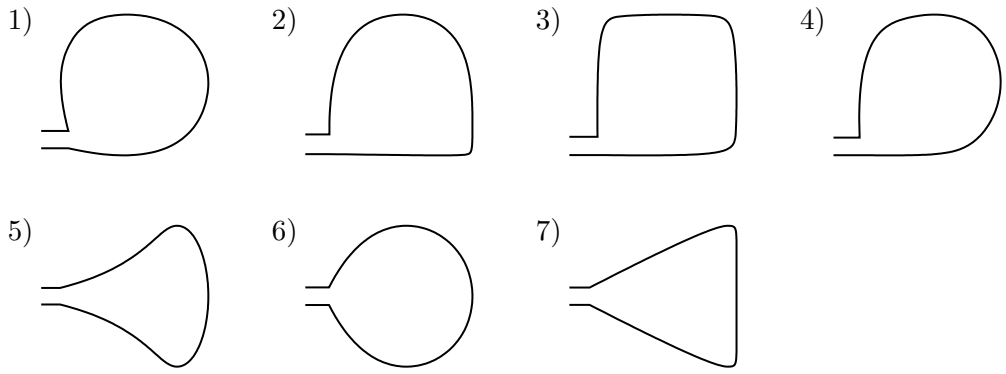

Figure 6.8: Selection of different volute cross-sectional shapes for the initial population of the genetic optimization. Other shapes are a random combination of these base geometries.

Each individual consists of a unique combination of design parameters. These parameters consists of the x and y coordinates of the eight control points of the spline, which represents the cross-sectional shape of the volute. The first and last control point are fixed. As a result, there are twelve parameters per individual volute shape. Upper and lower bounds are used for each parameter to restrict the design space and avoid infeasible designs. These constraints are shown in Figure 6.9 for the upper three control points (the lower points are omitted due to symmetry reasons). In order to maintain producibility, the angle between the volute spline and the radial diffuser is limited to $\upsilon \geq 45°$.

In the second step of the optimization process (2) is dedicated to the pre-processing. The coordinates of the control points for the volute spline generation are passed to the geometry generation tool, which creates the STL-surfaces of the volute. These surfaces are used by `snappyHexMesh` to create an unstructured hexahedral grid for the simulation as presented in section 6.1.2. After passing a mesh quality test, the grid is merged with the inlet and impeller part shown in section 5.2.1 to complete the model of the centrifugal compressor.

The numerical simulations in the third step (3) are performed on the high performance computing (HPC) cluster at the University Computer Center in Freiberg. It consists of 144 nodes with Intel Xeon X5670 processors at a clock speed of 2.93 GHz and 24 GB RAM per node. This results in 1728 CPU cores and a peak performance of

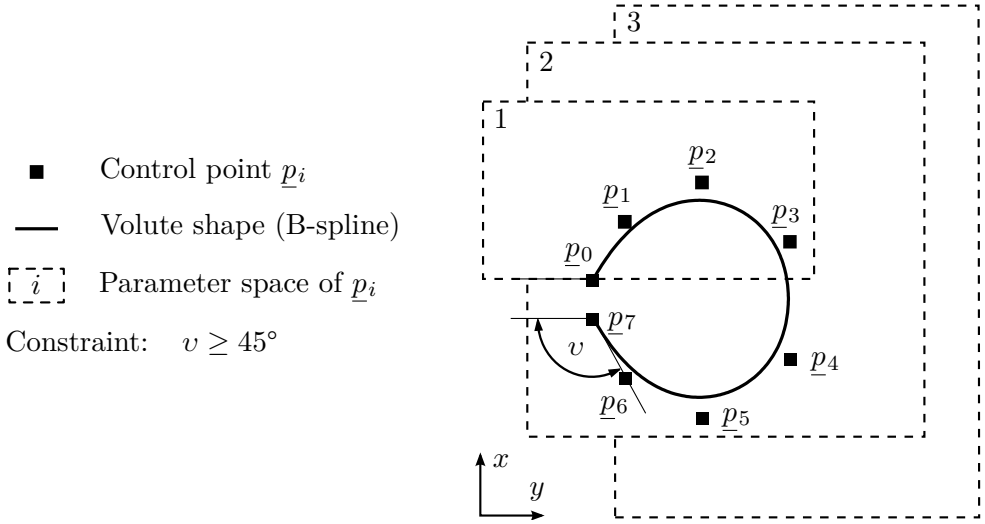

Figure 6.9: Parameter space for the three control points $\underline{p}_{1-3}$ for the volute shape. The lower three points $\underline{p}_{4-6}$ are omitted due to symmetry.

20.25 TFlops/s. OpenFOAM is employed for the simulations. The numerical settings and boundary conditions are identical to the turbocharger simulation in the previous chapter. Four simulations (one for each mass flow rate) are performed per volute geometry. In order to speed up the simulations, the results of previous individuals are mapped to the new ones as initial solution.

In the last step (4), the simulation results are evaluated and the average isentropic efficiency $\bar{\eta}_{\mathrm{is}}$ is calculated for each volute shape. The result is passed to the genetic algorithm. Once all individuals of one generation are evaluated, a new generation is created.

6.4 Results

6.4.1 General Findings

The geometry optimization is run until 40 generations are investigated. This results in 2000 individual volute shapes. One simulation for a single operating point of one volute geometry takes approximately 10 h on 32 CPU cores including geometry generation and meshing. Extrapolating this onto the complete genetic optimization,

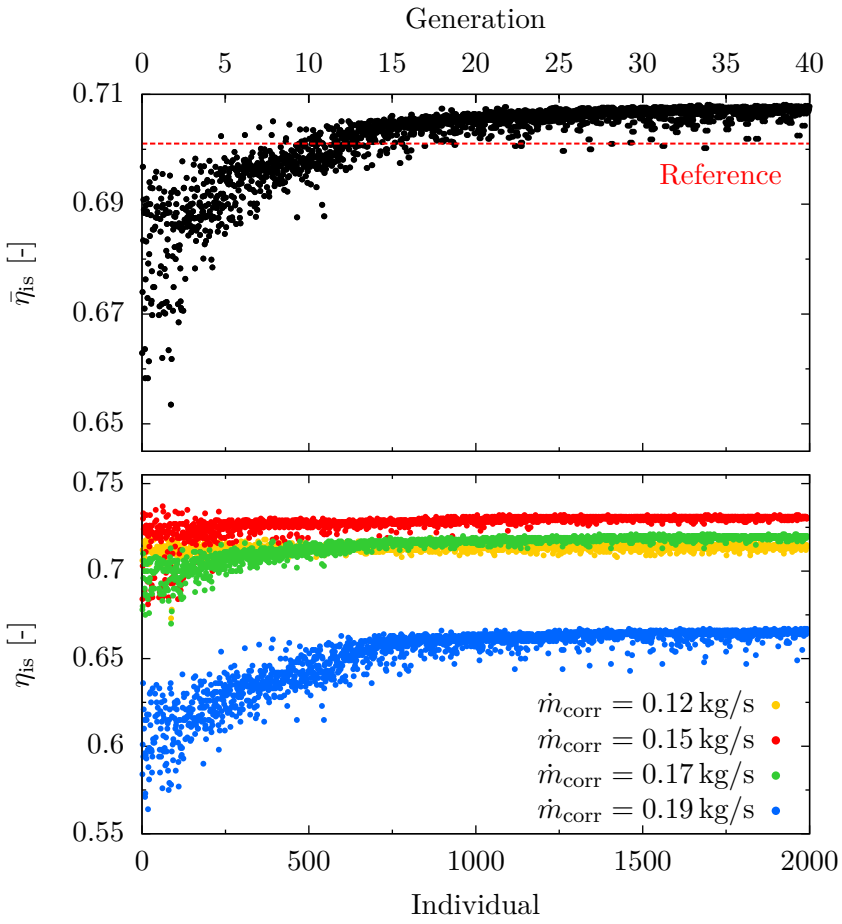

Figure 6.10: Averaged isentropic efficiency (top) and isentropic efficiency at each operating point (bottom) plotted for each individual of the genetic optimization.

the computational time is about 2 560 000 h CPU time, or nearly 73 years on a four core workstation. For this reason, such a complex task can only be performed using state of the art HPC cluster.

The progress of the genetic optimization is monitored by evaluating the average isentropic efficiency of every individual as shown in Figure 6.10 (top). At the beginning of the optimization, the difference between the worst and best volute geometry for each generation is nearly 5 % and the average performance is worse than the reference centrifugal compressor. During the first few generations, the stage efficiency increases significantly. After about five generations, the performance of the reference volute is passed and after 25 generations (equals 1250 individuals), no further significant

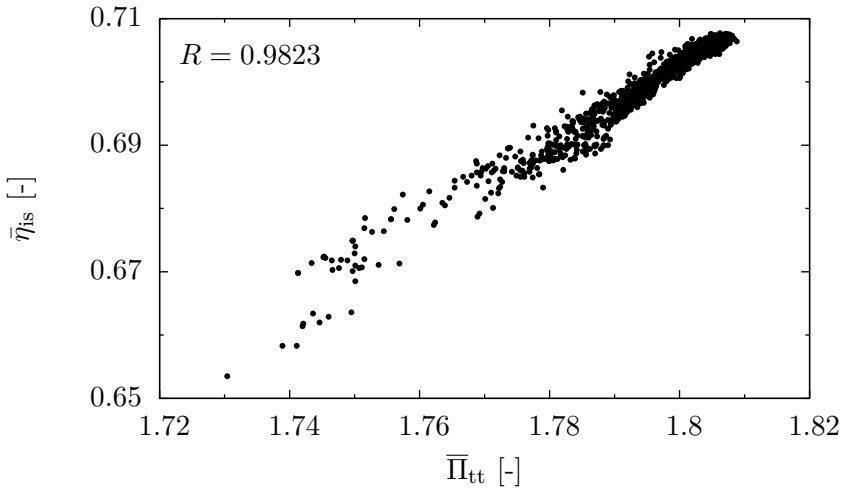

Figure 6.11: Averaged isentropic efficiency plotted against the averaged total pressure ratio and the resulting correlation coefficient R.

improvement is noticeable. At this point, the difference between the best and worst individual of a generation is less than 1 %. A clear trend towards an improved compressor performance is recognizable. The best volute geometry after 40 generations claims an increase in average isentropic efficiency of about 0.5 % compared to the reference compressor.

The improvement of η_{is} during the optimization is not distributed equally between the four investigated operating points. It is mainly contributed by efficiency gains at high off-design flow rates (see Figure 6.10, bottom). The average rise of η_{is} during the optimization for the highest flow rate is over 7 %, while the increase at 0.17 kg/s is about 3 %. The performance improvement at lower mass flow rates is less than 1 %, though. The operating point with the highest efficiency remains at 0.15 kg/s.

The genetic optimization uses only the isentropic efficiency η_{is} of the compressor for calculating the objective function. This assumes that a change in η_{is} also results in a correlated change in total pressure ratio Π_{tt}. For this reason, Π_{tt} is not needed for a second objective function. This assumption is supported by plotting $\bar{\eta}_{is}$ against $\overline{\Pi}_{tt}$ for each individual (see Figure 6.11). There is a positive, linear correlation between both characteristics with a correlation coefficient of $R = 0.9823$. Thus, a rise in isentropic efficiency also leads to a proportional increase in total pressure ratio. Therefore, it is sufficient to perform an optimization for just one variable. There are outliers of

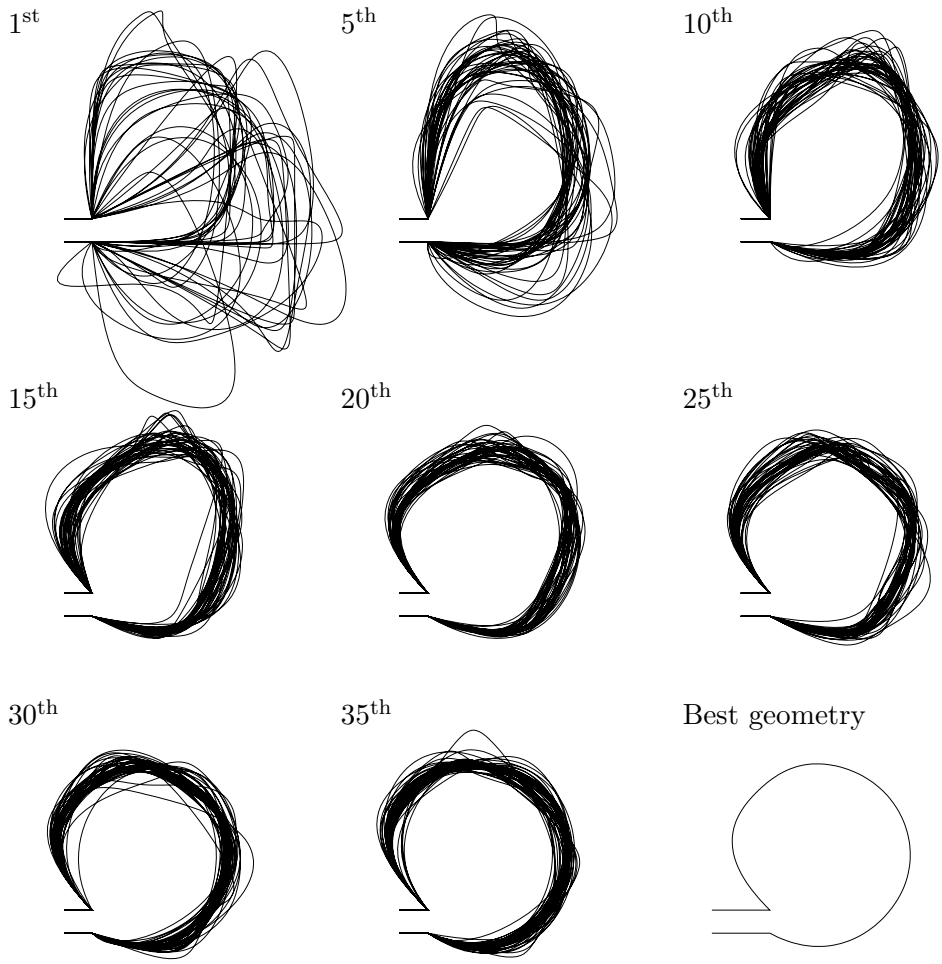

Figure 6.12: Volute shapes for every fifth generation and the best geometry at the end of the optimization.

this correlation. The reason for this might be interactions between the flow in the compressor wheel and the volute. However, this effect is assumed to be neglectable for the optimization.

A general statement about the isentropic efficiency improvement of the optimization is difficult since it strongly depends on the initial parameters. For instance, the optimization of Baloni et al. [9] presented in section 2.4 yielded an increase in performance of about 7.4 %. However, the efficiency of the reference model was very low with 46.7 %. In contrast, both Jang et al. [54] and Huang et al. [48] reported an increase in compressor performance of well below 2 %. Therefore, the achieved improvements in the presented optimization are well in line with typical results of other publications.

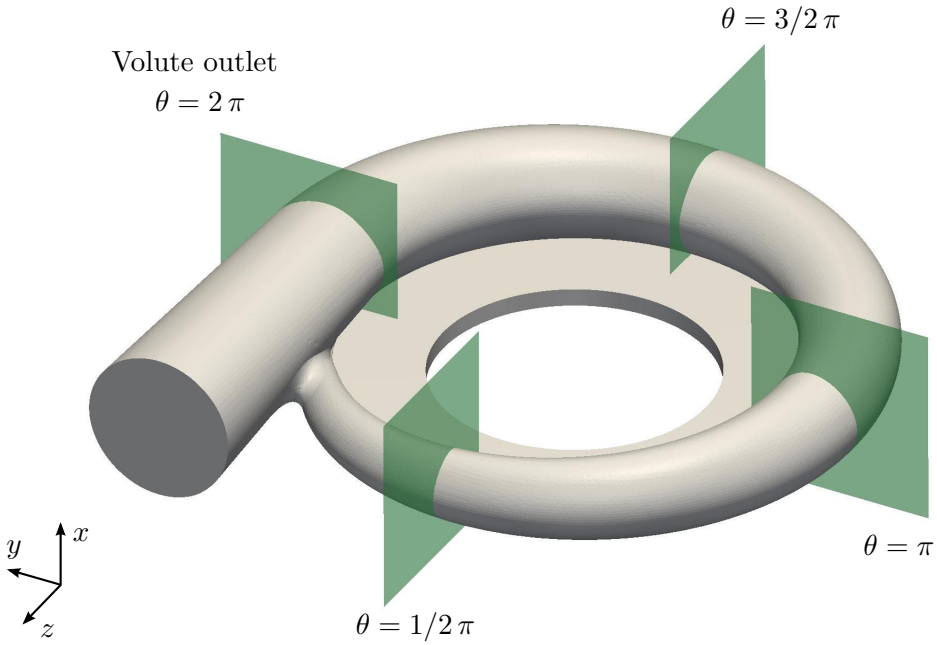

Figure 6.13: Definition of four planes for post-processing along the volute channel.

The volute geometry varies greatly over the course of the optimization. Different shapes for every fifth generation and the best cross-sectional volute shape are shown in Figure 6.12. There is a significant diversity during the first generations due to the wide range of initial volute shapes. A trend towards a favorable shape is clearly visible after ten generations, though. As the optimization progresses, poor performing individuals are sorted out and fitter ones start to dominate. The best individuals all have the same geometric features in common:

1. tangential volute inlet
2. lower radial location of the volute channel
3. rounded shape.

These characteristics are analyzed in detail in the following sections in order to assess their influence onto the volute performance. Four planes are used for post-processing as defined in Figure 6.13. These are used to plot velocity and pressure contour plots along the volute channel.

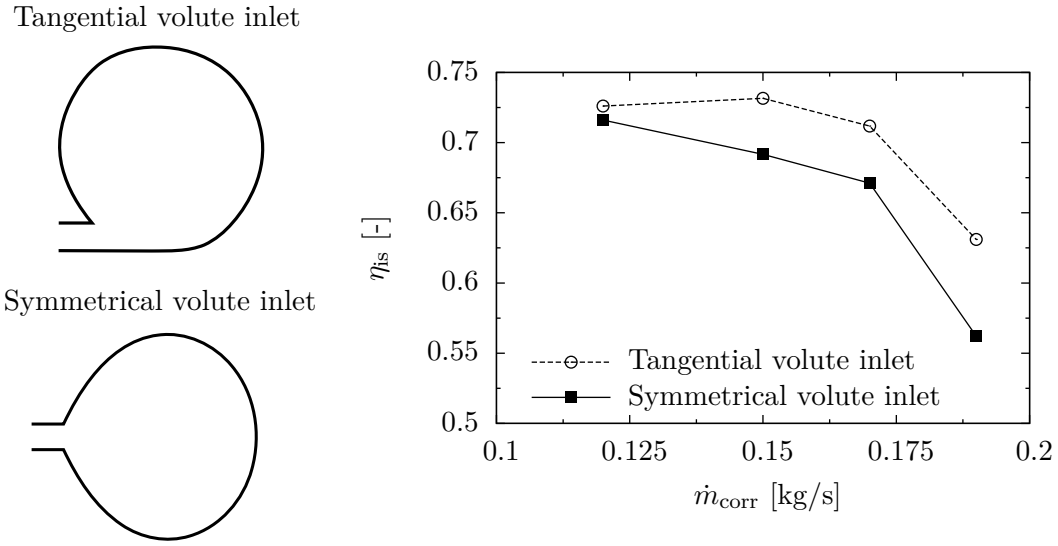

Figure 6.14: Volute cross-sectional shapes with different inlet location (left) and the corresponding compressor performance (right).

6.4.2 Volute Inlet Location

The location of the volute inlet has a significant impact on the compressor performance. In order to investigate this aspect, two different circular shaped volutes are compared (Figure 6.14, left). Both geometries are taken from the results of the optimization. The first one offers a symmetrical inlet while the second one is the geometry from the reference compressor with a tangential inlet. Despite the different inlet position and a slightly larger center radius of the volute channel, both geometries are identical. Nevertheless, differences in performance can be mainly attributed to the inlet location. In general, the shape with a tangential inlet offers a significantly better isentropic compressor efficiency as shown in Figure 6.14 (right). The difference is up to 8 % at high mass flow rates. Both geometries offer similar results at low flow rates, though.

Static and total pressure at the volute exit are shown in Figure 6.15 and 6.16 for a corrected mass flow rate of 0.12 kg and 0.19 kg, respectively. Despite the differences in pressure profiles, the average static pressure level is similar for both geometries. The maxima are located at the back wall of the volute. Due to the conservation of angular momentum, the flow velocity is lower at larger radii. Therefore, the static pressure is increased at the outer wall. Consequently, the fluid is reaccelerated at the inner wall of the volute due to the smaller radius, which leads to a lower static pressure.

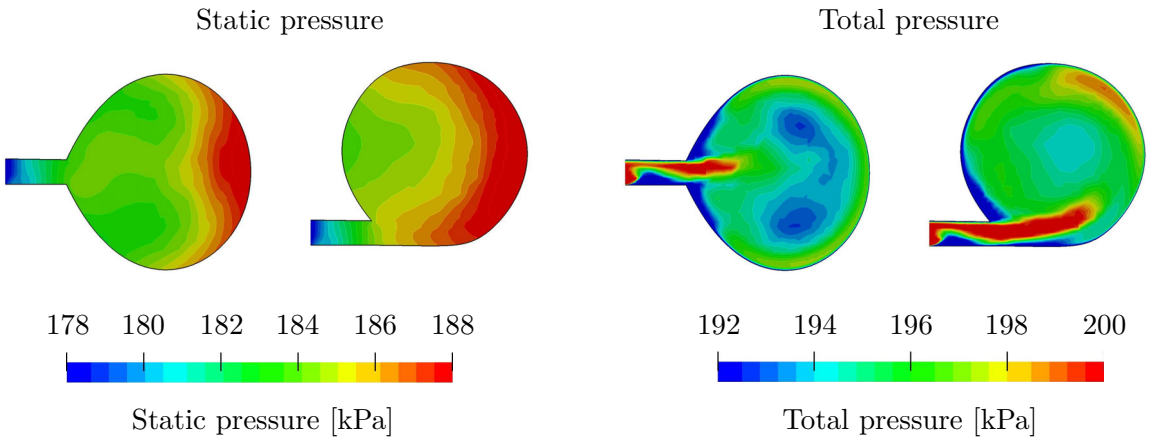

Figure 6.15: Static pressure and total pressure contour plots at the volute exit for symmetrical and tangential volute inlet at $\dot{m}_{\text{corr}} = 0.12\,\text{kg/s}$.

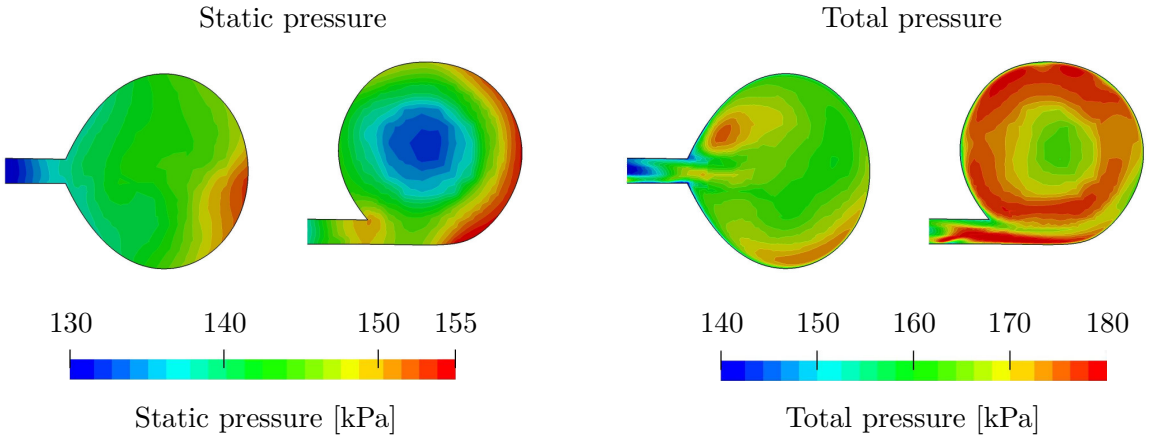

Figure 6.16: Static pressure and total pressure contour plots at the volute exit for symmetrical and tangential volute inlet at $\dot{m}_{\text{corr}} = 0.19\,\text{kg/s}$.

Furthermore, centrifugal forces at high mass flow rates lead to an accumulation of fluid with high kinetic energy at the volute walls. As a result, static and total pressure are increased in these regions. Furthermore, low energy fluid leads to a decreased level of total pressure in the center of the volute channel. Another observation is the higher static and total pressure at lower flow rates. This results from lower shear stress losses due to reduced flow velocities. Additionally, the volute is designed for operating conditions of $(0.12 - 0.15)\,\text{kg/s}$. As a result, it cannot accommodate larger flow rates and starts to act like a nozzle. The reduction of these high losses offer large potential of improving at off-design conditions.

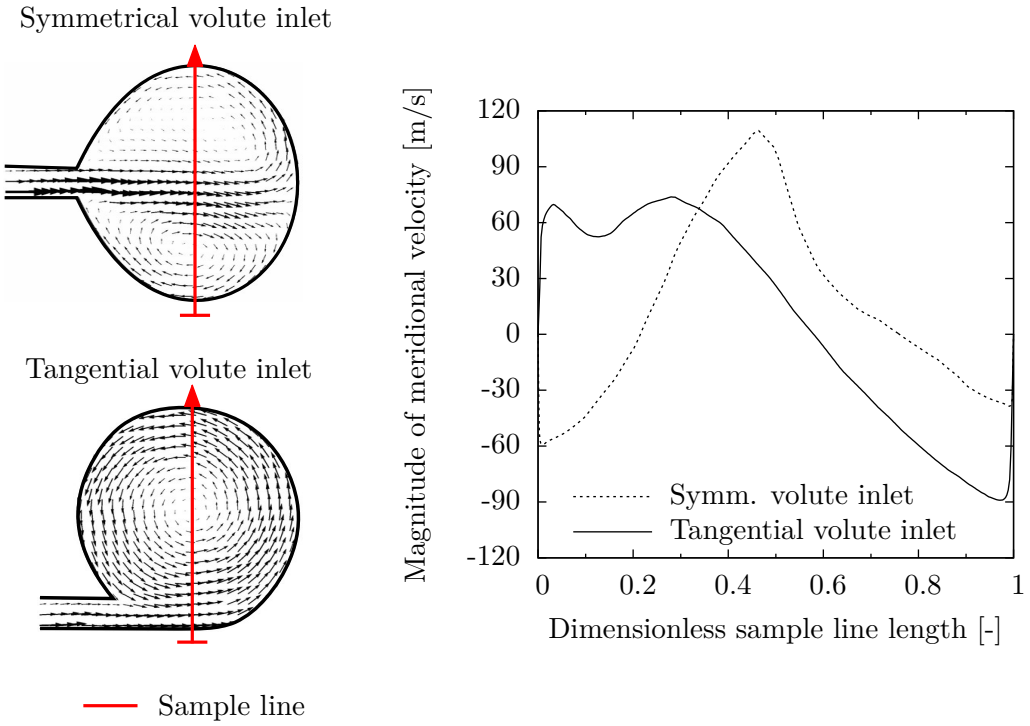

Figure 6.17: Meridional velocity vectors (left) and profile (right) over a sample line for different inlet locations at volute exit at $\dot{m}_{\text{corr}} = 0.19\,\text{kg/s}$.

The differences in performance between a volute with a symmetrical and tangential inlet increase at higher mass flow rates. Although the average static pressure is similar, the average total pressure of the tangential inlet is significantly higher compared to the symmetrical one. The difference in average total pressure is nearly 9 kPa. This directly correlates with the superior isentropic efficiency of the compressor. The reason for the inferior performance can be found in the shear stress losses resulting from the different vortex structures. A vector plot of the meridional velocity[1] is shown in Figure 6.17 (left). The tangential inlet results in a single large vortex with its center in the middle of the volute channel. In contrast, the symmetric inlet forms a jet inside the volute, which creates two smaller vortices. Due to this double vortex, the meridional velocity gradients are higher as shown in Figure 6.17 (right). This is in particular the case close to the jet in the center of the volute channel. At the same time, the tangential inlet results in more homogeneous velocity distribution and therefore lower losses.

[1] Vector sum of axial and radial vector components of velocity with respect to the global coordinate system of the compressor.

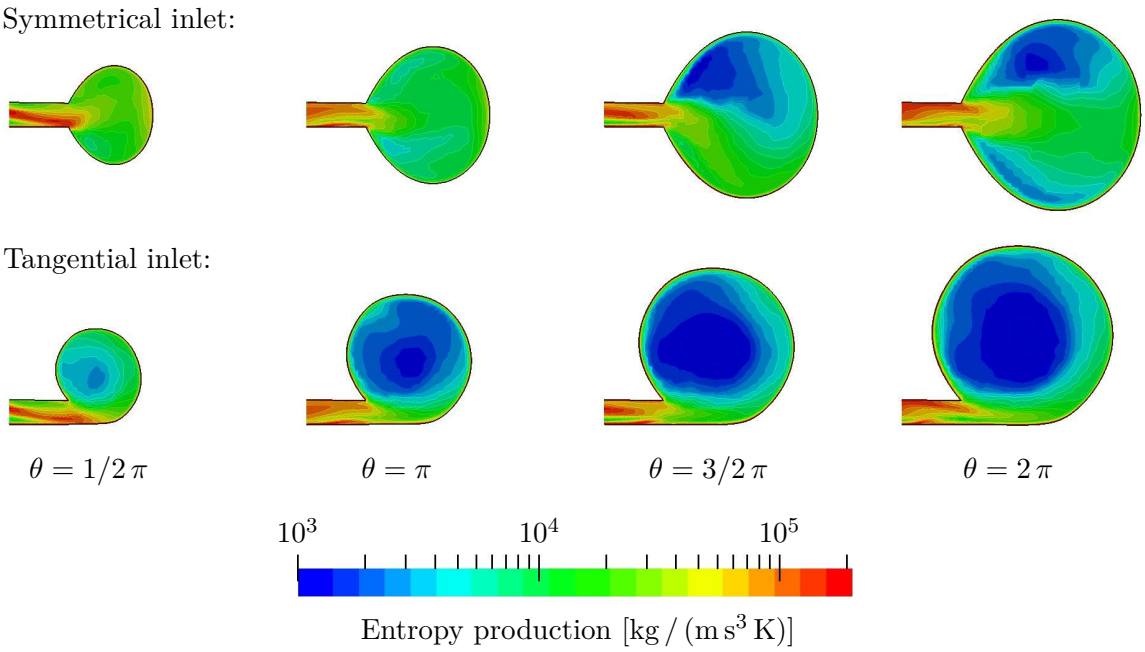

Figure 6.18: Entropy production contour plots in the volute channel at different circumferential positions for symmetrical and tangential volute inlet at $\dot{m}_{\mathrm{corr}} = 0.19\,\mathrm{kg/s}$.

These findings are supported by plotting the entropy production rate P_S. According to Kock and Herwig [58], this rate can be estimated as following:

$$P_S = \frac{1}{T}\left(\underline{\underline{\tau}} : \nabla \underline{u}\right) + \frac{\rho\epsilon}{T} + \frac{\lambda}{T^2}\left|\nabla T\right|^2 + \frac{a_t}{a}\frac{\lambda}{T^2}\left|\nabla T\right|^2 \ , \tag{6.7}$$

with the thermal conductivity λ, the laminar a and turbulent a_t thermal diffusivity, and the turbulent dissipation estimated from the SST-RC $k-\omega$ turbulence model:

$$\epsilon = \beta^* k\omega \ . \tag{6.8}$$

The first term on the right-hand side describes the entropy production rate by direct dissipation, the second one by turbulent dissipation, the third one by heat conduction due to mean temperature gradients and the fourth one by heat conduction due to fluctuating temperature gradients.

Figure 6.18 shows the entropy production for both geometries at an operating point of $\dot{m}_{\mathrm{corr}} = 0.19\,\mathrm{kg/s}$ at different circumferential positions. A double vortex structure

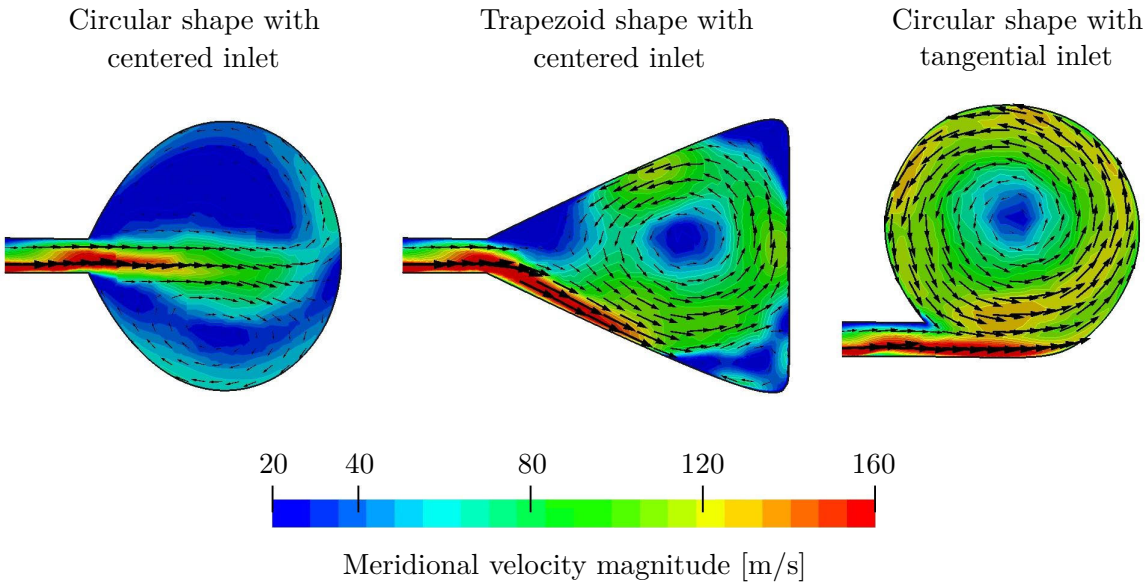

Figure 6.19: Meridional velocity magnitude and vectors for three different volute shapes with centered and tangential inlet at $\dot{m}_{\mathrm{corr}} = 0.19\,\mathrm{kg/s}$.

leads to high entropy production in the volute channel due to increased velocity gradients. In contrast, a single large vortex with leads to lower entropy generation, in particular in the center of the volute channel. This directly correlates to the significantly better isentropic efficiency of a volute with tangential inlet compared to a symmetrical one.

The negative effect of a symmetrical inlet position does not depend on the actual volute cross-sectional shape. For instance, a trapezoidal shape with a centered inlet leads to even higher losses. This is due to instabilities induced by the highly non-uniform flow downstream the compressor wheel. The two smaller vortices typically found in volutes with symmetrical inlet are overtaken by a single vortex as shown in Figure 6.19. However, this results in regions with recirculation in the corners of the channel and at the volute inlet. Fluctuations and additional movement eventually leads to increased losses. In contrast, a volute with tangential inlet leads to a large stable vortex in the center of the volute with no recirculation and reduced losses.

These findings can be generalized by introducing the eccentricity e as defined in Figure 6.20 (left). A value of zero indicates a symmetrical volute inlet while values close to -1 and 1 stand for a tangential inlet position. An eccentricity close to -1 was not investigated due to limited installation space. A volute channel in negative

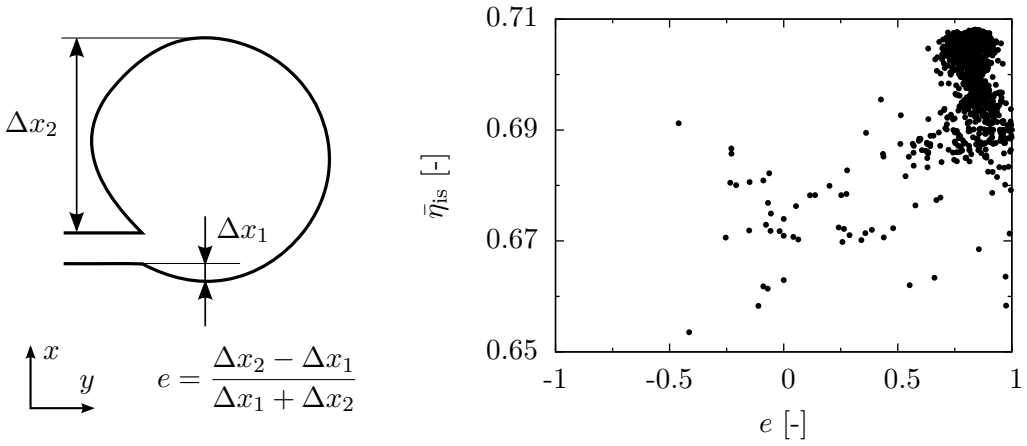

Figure 6.20: Definition of the eccentricity e (left) and its effect onto the average compressor efficiency $\bar{\eta}_{is}$ for each individual (right).

x-direction is obstructed by the turbocharger oil circulation system and the turbine side. The results of the optimization show that a value of approximately 0.85 results in the highest compressor performance (see Figure 6.20, right). This corresponds to the final shape of the numerical optimization. A volute with a perfectly tangential inlet ($e = 1$) does offer a slightly worse performance, though. The tendency is that a symmetrical inlet offers the worst performance. The differences between tangential inlets with various eccentricities correlates to the radial location of the volute channel. This will be explained in the following section.

6.4.3 Radial Location of the Volute Channel

The radial location of the volute channel is the second characteristic of the optimized model. Three different volute geometries are chosen to investigate this effect onto the compressor performance as shown in Figure 6.21. The first geometry is called baseline model and consists of a circular shape with a rectangular connection between the upper diffuser wall and the volute channel. The overhung with respect to the volute inlet Δx and Δy is zero. This variant has the largest radial location of the volute channel in this investigation. The reference model is the original volute shape of centrifugal compressor presented in chapter 5. It also offers a circular shape. However, the overhung in x-direction is approximately 5 mm. Therefore, the radial location of the volute channel is smaller compared to the first geometry. The last model is the

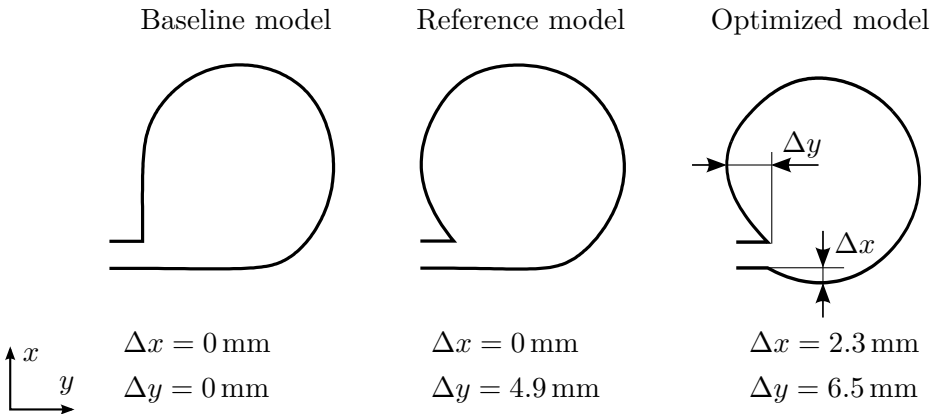

Figure 6.21: Three different cross-sectional shapes with different location of the volute channel indicated by the overhung in x- and y-direction at volute exit.

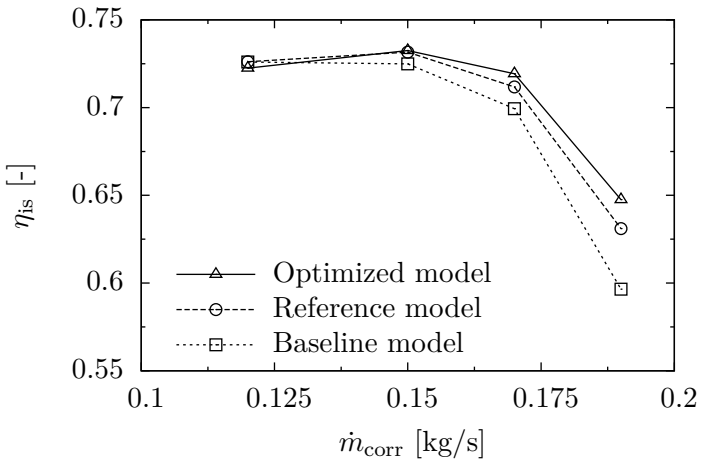

Figure 6.22: Isentropic efficiency of volute shapes with different radial location.

best shape of the numerical optimization. Its radial location is shifted even further by 6.5 mm and 2.3 mm in x- and y-direction, respectively. The remaining geometric parameters are identical for all three models.

The isentropic efficiency for all three variants is compared in Figure 6.22. Similar to the previous findings, the differences between the geometries are very small for low mass flow rates with a small edge in isentropic efficiency for the baseline and reference model by 0.4 %. As the flow rate increases, the optimized model yields the best performance. This results in an increased isentropic efficiency of 2 % compared to the reference model and 5 % compared to the baseline model at the highest mass flow rate.

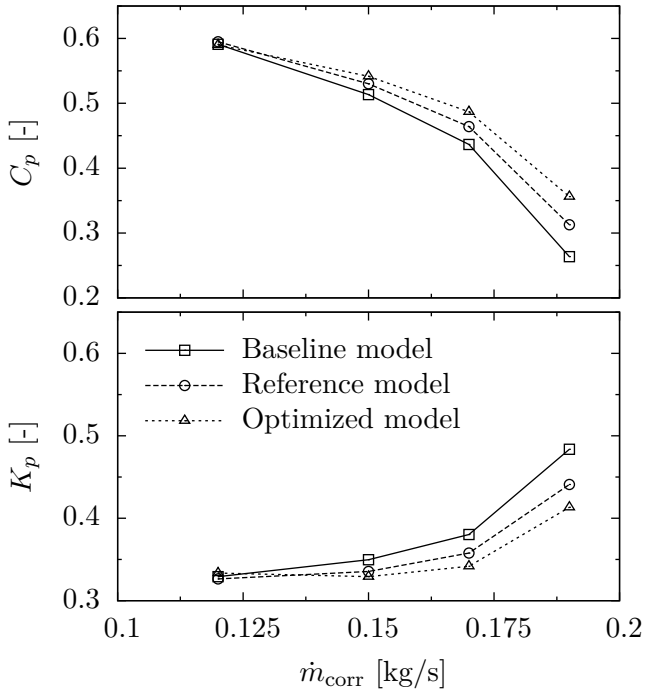

Figure 6.23: Static pressure recovery C_p and total pressure loss coefficient K_p of the volute for different radial channel locations.

Figure 6.23 shows the volute performance for the three variants. Similar to the previous results, there are no differences at low flow rates for the different geometries. However, as the flow rate increases, the optimized volute offers a significantly better pressure rise coefficient and lower total pressure loss coefficient. The improvement is over 12 % for C_p and about 6 % for K_p compared to the reference model at $\dot{m}_{\mathrm{corr}} = 0.19\,\mathrm{kg/s}$. Although the influence of the radial location of the volute channel onto the stage performance is small, the effect onto the flow inside the volute and is noteworthy.

The flow pattern of the three volutes are very similar at low flow rates. Figure 6.24 shows the meridional velocity at the volute exit for a mass flow rate of 0.12 kg/s. The maximum velocity is low with 60 m/s. In all cases, the jet downstream the volute inlet results in a primary vortex in the volute channel. Secondary vortices are developed at the rectangular connection between radial diffuser and inner volute wall for the baseline model. In case of the reference and optimized model, a recirculation zone is present at the lower wall of the volute. As a result, the jet is slightly deflected towards the channel center. Overall, the friction losses are minor due to the low flow speeds.

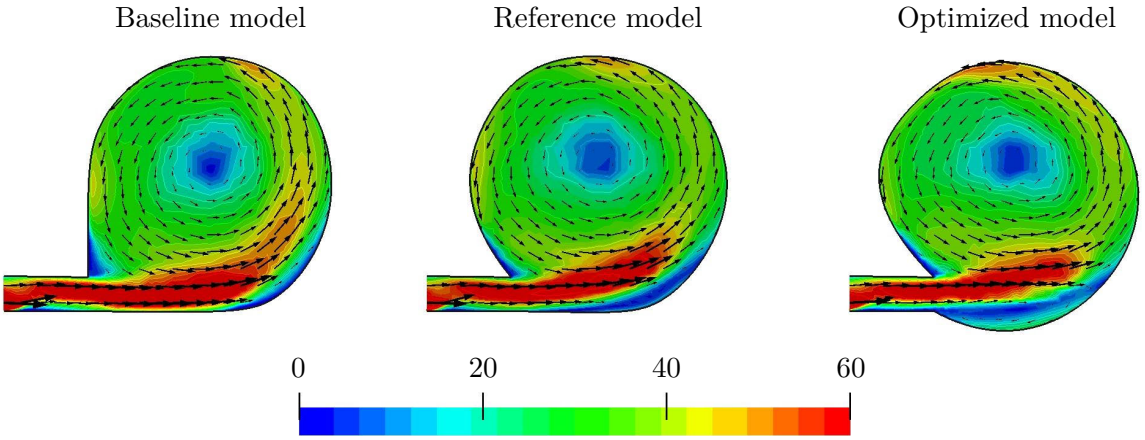

Figure 6.24: Meridional velocity magnitude and vectors for the baseline, reference, and optimized volute model at $\dot{m}_{\mathrm{corr}} = 0.12\,\mathrm{kg/s}$.

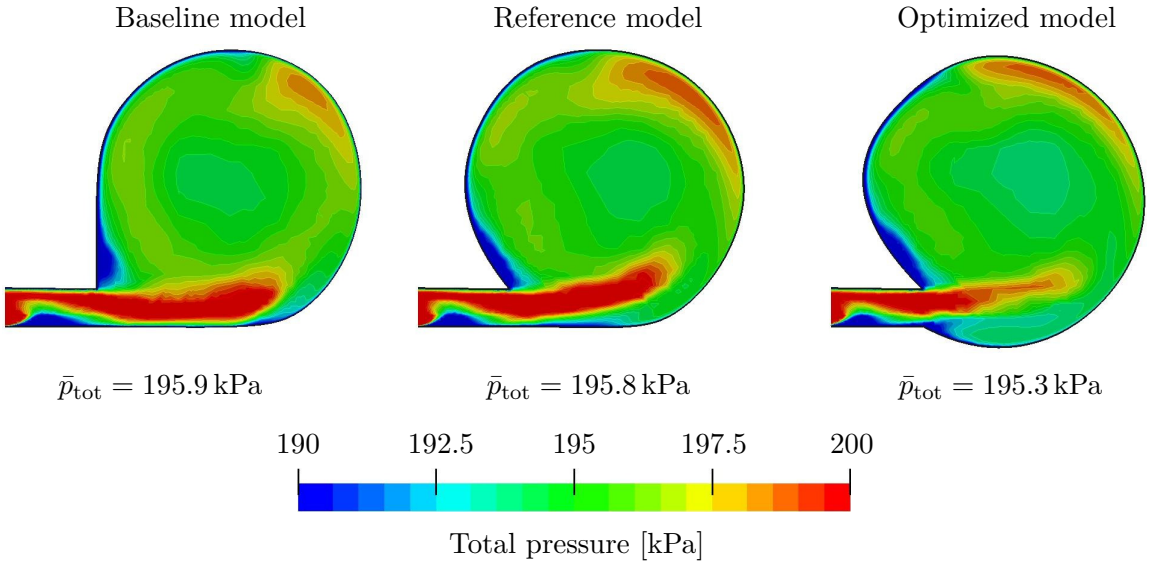

Figure 6.25: Total pressure contour plots at the volute exit at $\theta = 2\,\pi$ for the baseline volute model, reference model and optimized model at $\dot{m}_{\mathrm{corr}} = 0.12\,\mathrm{kg/s}$.

As a result, the compressor performance is very similar despite differences in flow pattern in the volute channel. This similarity is also visible in the total pressure plots at the volute exit as shown in Figure 6.25. The optimized model has a slightly lower total pressure level at the volute exit. The differences of $\Delta\bar{p}_{\mathrm{tot}} = 0.6\,\mathrm{kPa}$ results in a lower average isentropic efficiency of about 0.4 %. The baseline and reference model yield a similar performance.

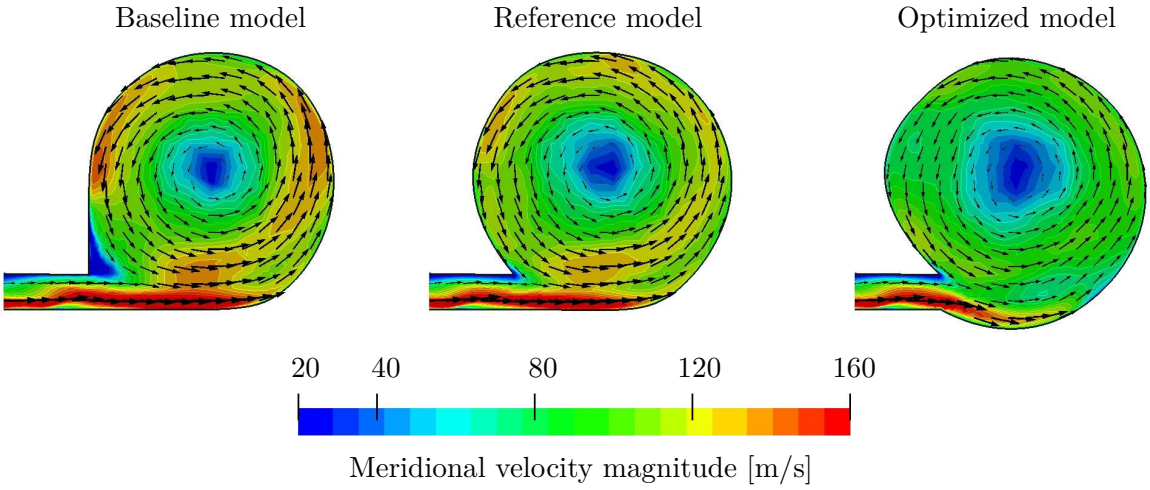

Figure 6.26: Meridional velocity magnitude and vectors for the baseline, reference, and optimized volute model at $\dot{m}_{\mathrm{corr}} = 0.19\,\mathrm{kg/s}$.

Despite the similar performance at low flow rates, the three models offer very different results at high flow rates. Figure 6.26 shows the magnitude of meridional velocity at volute exit and the corresponding velocity vectors. A large vertex is developed in all cases with a velocity minimum at the center of the volute channel. Differences can be found in the recirculation zone near the volute inlet of the baseline model. Furthermore, the near-wall velocity is much higher close to the lower wall of the baseline and reference model. In general, the meridional velocity of the optimized model is lower and the velocity profile more homogeneous in the volute channel. These differences lead to lower shear stress losses resulting in a higher average total pressure as shown in Figure 6.27. The average value of the baseline model is about $(3-4)\,\mathrm{kPa}$ lower than the other models. The total pressure is lower due to the higher losses compared to low flow rates. However, it is more evenly distributed throughout the volute cross-section.

Two geometrical changes lead to different flow pattern and consequently an improved performance as shown in Figure 6.28. Firstly, the rectangular connection between the volute and the upper radial diffuser in the baseline model leads to the development of a recirculation zone. As a result, a part of the volute cross-section is blocked by this vortex for the flow through the volute. Therefore, the flow velocity is higher in the rest of the volute channel. This secondary vortex is avoided by the reference and optimized model using a lower angle at the corner between volute and upper

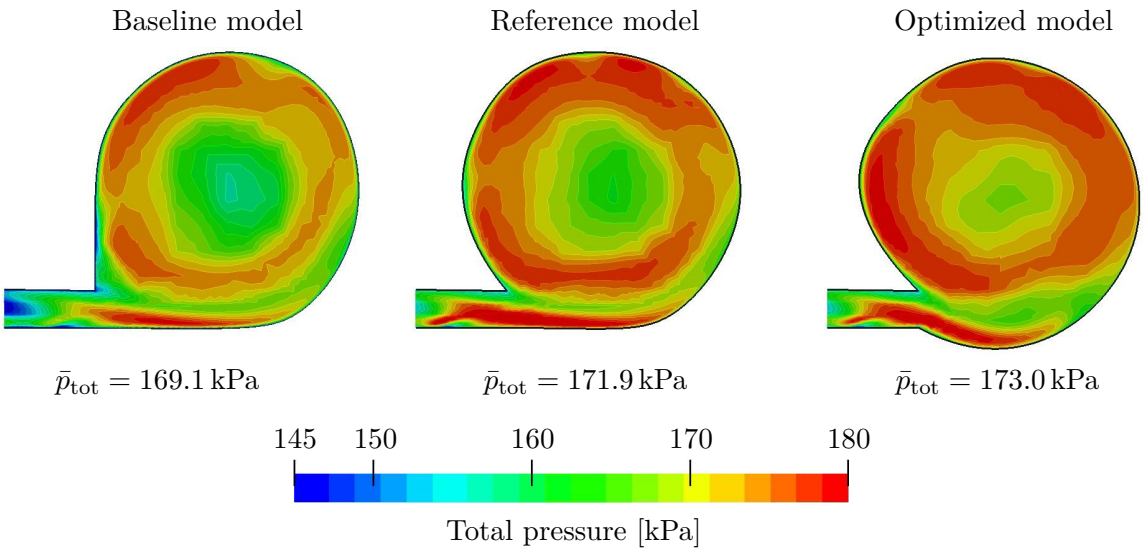

Figure 6.27: Total pressure contour plots at the volute exit at $\theta = 2\,\pi$ for the baseline volute model, reference model and optimized model at $\dot{m}_{\mathrm{corr}} = 0.19\,\mathrm{kg/s}$.

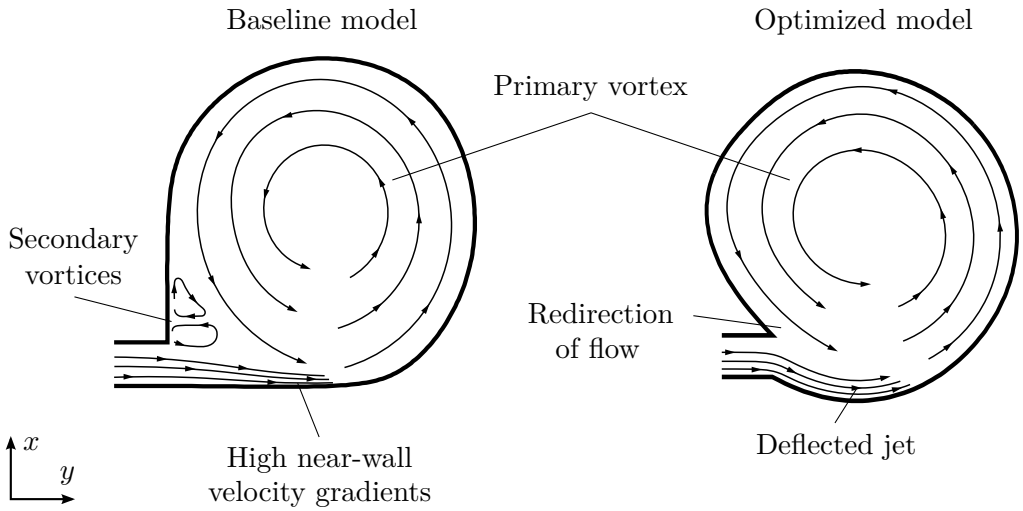

Figure 6.28: Schematic streamlines and flow phenomena for the baseline model (left) and the optimized volute model (right) at high flow rates.

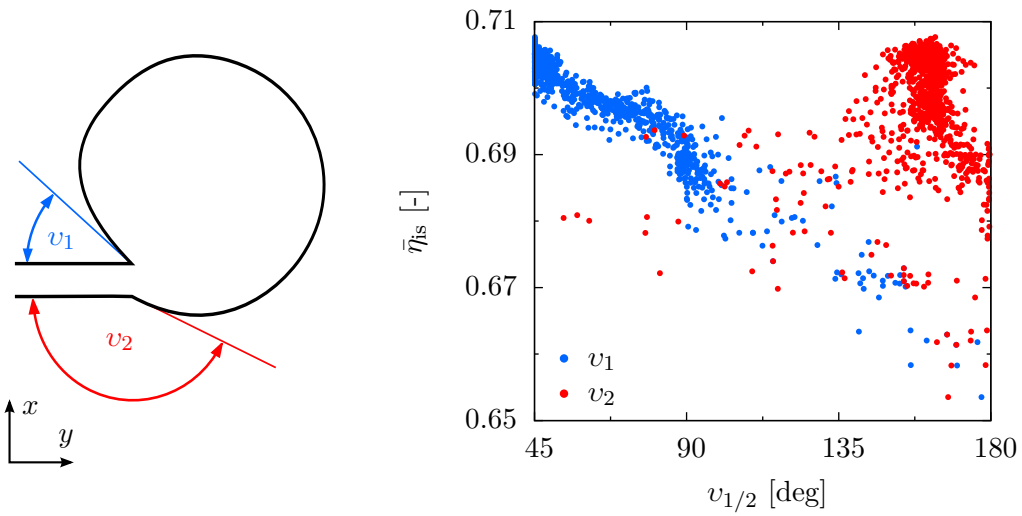

Figure 6.29: Definition of the volute inlet angle $\upsilon_{1/2}$ (left) and its influence onto the average compressor efficiency $\bar{\eta}_{is}$ for each individual (left).

Table 6.2: Inlet angles for the investigated models.

Model	υ_1	υ_2
Baseline	90°	180°
Reference	45°	180°
Optimized	45°	160°

radial diffuser. The second effect is the straight lower wall of the volute channel in the baseline and reference model which results in higher near-wall velocity gradients. As a consequence, larger gradients result in increased flow losses. The optimized geometry features a curved wall. Therefore, the jet downstream the volute inlet can be deflected by the primary vortex due to the higher momentum compared to low flow rates. This leads to lower near-wall velocities and a shortened jet.

The lower radial position of the volute channel and the curved lower wall can be characterized by the volute inlet angle $\upsilon_{1/2}$ as defined in Figure 6.29 (left). The corresponding angles for the baseline, reference and optimized model are summarized in Table 6.2. A lower limit of $\upsilon = 45°$ is introduced as constraint for the optimization to avoid unmanufacturable designs. Geometries with sharp angles are difficult to manufacture using die-casting. The effect of these angles onto the average compressor

efficiency is shown in Figure 6.29 (right). As the angle υ_1 is reduced, the performance of the volute is increased. The correlation coefficient is $R_1 = -0.9572$ showing a negative, linear relationship. The maximum is achieved at a value of $\upsilon_1 = 45°$. The correlation between inlet angle υ_2 and the efficiency is weak with $R_2 = 0.1676$. However, a clear maximum is recognizable for a angle of about 160°. This value results in a shape like the optimized model with a tangential volute inlet.

6.4.4 Volute Cross-sectional Shape

The third characteristic of the optimized volute model is its circular shape. In order to investigate this influence, two different volute shapes are analyzed (see Figure 6.30, left). The first model is a circular volute with a rounded corner. The second one is a semi-circular shape with a sharp corner the outer lower wall. Otherwise, both shapes are similar in terms of radial position and inlet location. The isentropic compressor efficiency is shown in Figure 6.30 (right). The circular shape offers a better performance compared to the semi-circular shape with a difference of about 0.5 %. Similar to previous sections, the difference is negligible at low flow rates. In contrast, the offset is nearly constant at flow rates between (0.15 – 0.19) kg/s, though.

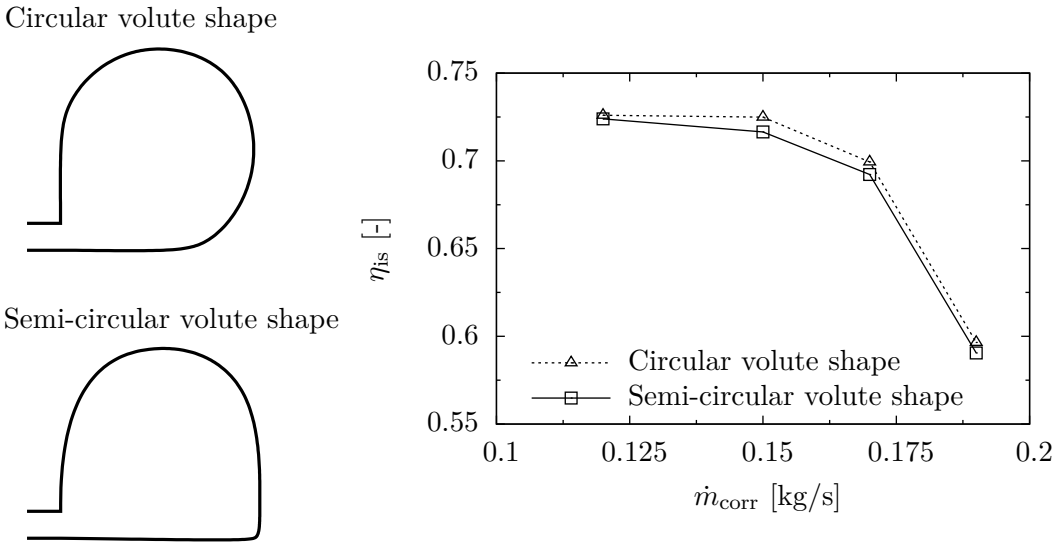

Figure 6.30: Different volute cross-sectional shapes (left) and the corresponding compressor performance (right).

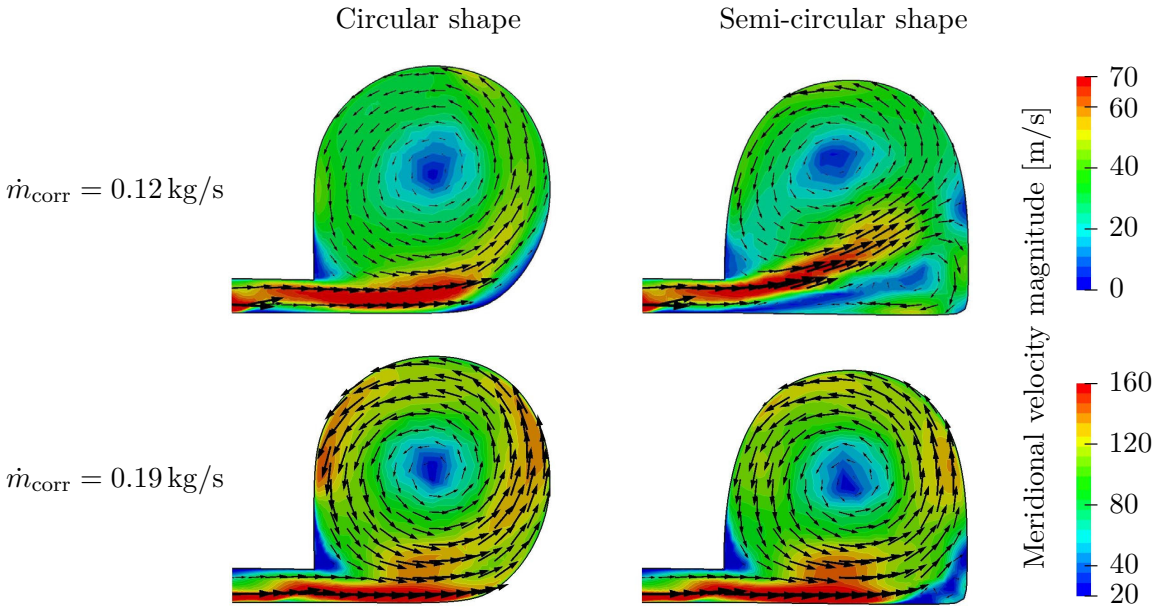

Figure 6.31: Magnitude of meridional velocity at the volute exit for the circular and semi-circular shaped volute at a corrected mass flow rate of 0.12 kg/s and 0.19 kg/s.

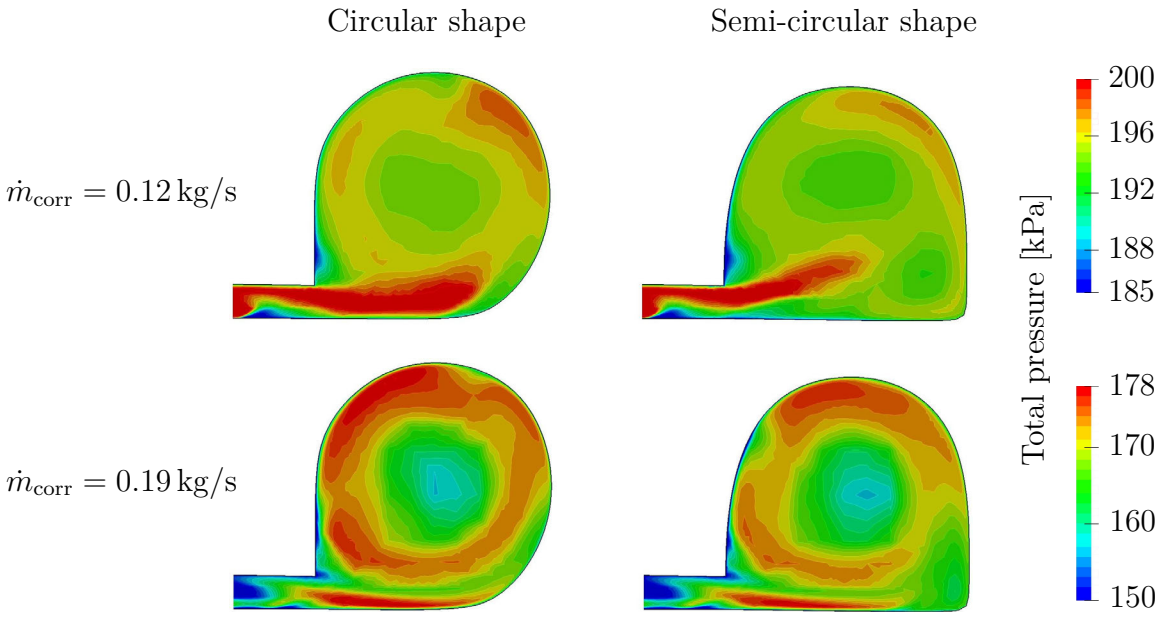

Figure 6.32: Total pressure at the volute exit for the circular and semi-circular shaped volute at a corrected mass flow rate of 0.12 kg/s and 0.19 kg/s.

The meridional velocity magnitude at the volute exit is compared in Figure 6.31 for different flow rates. A primary vortex is developed in the volute channel in both geometries. However, the sharp corner of the semi-circular shape results in a recirculation region in the lower right edge of the channel. Its size depends on the flow velocity. At low mass flow rates, the jet downstream the volute inlet is deflected by the recirculation region. Therefore, its size is considerably larger compared to high mass flow rates. Due to lower flow velocities, it has a smaller impact onto compressor performance at lower flow rates, though. In contrast, the circular shape avoids this secondary vortex entirely leading to better performance. The effect of the recirculation zone is also visible in the contour plot of the total pressure at the volute exit (see Figure 6.32). The total pressure is significantly lower at the sharp corner of the semi-circular volute at high flow rates. This behavior is to a lesser extent similar at lower flow rates. The difference in total pressure between both models is approximately 1 kPa at each operating point.

The influence of the actual shape of the volute channel onto the compressor performance is only minor compared to other geometric characteristics, such as inlet or radial position of the volute channel. This is apparent when comparing different geometry variations from the optimization with nearly similar performance. The isentropic efficiency is shown in Figure 6.33 for four volute shapes. Although they are quite different in shape, the performance is nearly identical. The variation in average isentropic efficiency is less than 0.1 %. Similarly, the profiles of total pressure at the volute exit are almost identical as shown in Figure 6.34. All four shapes have in common that the inlet is tangential, the radial volute position is slightly reduced, and the lower wall is curved. As long as there are no sharp edges resulting in recirculation, the actual shape of the volute is not an important geometric parameter.

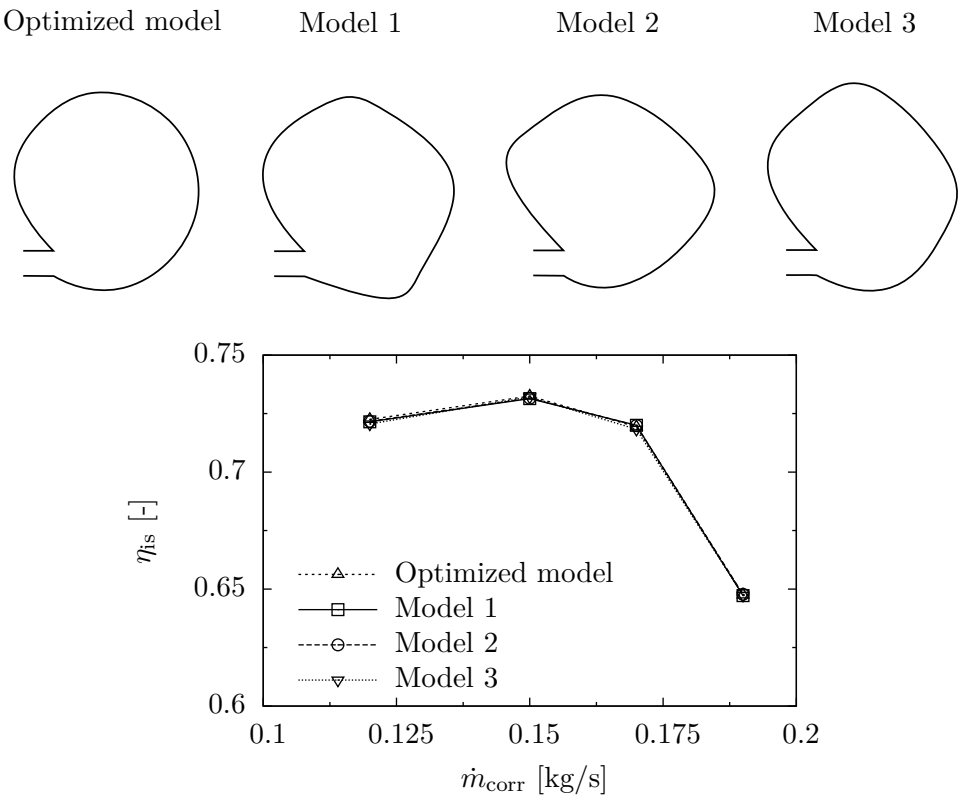

Figure 6.33: Different volute cross-sectional shapes (top) and compressor performance (bottom).

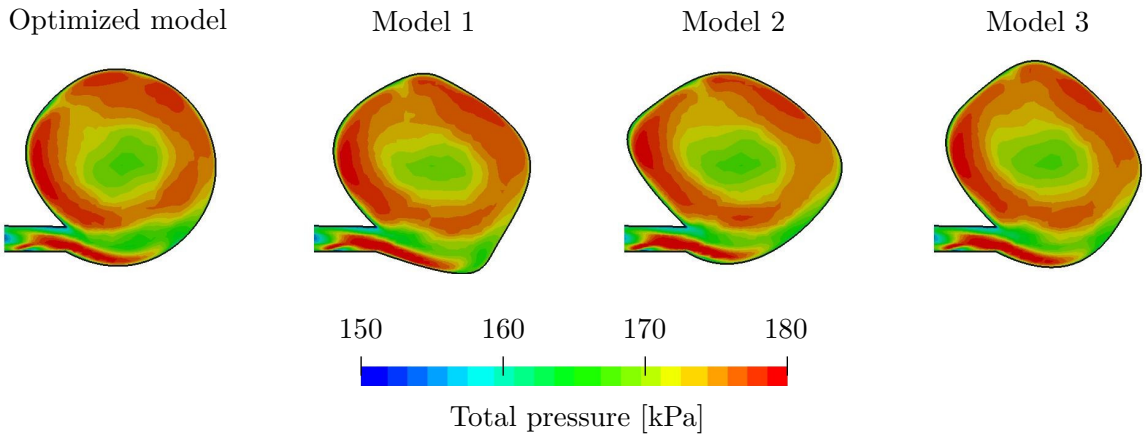

Figure 6.34: Total pressure at the volute exit for four different volute shapes.

7 Conclusion

The genetic optimization of a volute housing presented in this thesis is a novelty in the scientific community. In this particular field of research, the number of publications is very sparse. As shown in section 2.4, only three similar paper were published in recent years. In all three cases, the shape of the cross-sectional volute is fixed and only its proportions are varied. For instance, Jang et al. [54] used a trapezoidal shape with a tangential inlet and its length and width as design parameters. Still, the actual shape remains trapezoidal. Similarly, Baloni et al [9] and Huang et al. [48] investigated a rectangular volute shape with width, among others, as optimization parameters. Once again, the variation of parameters is very limited.

In contrast to this, the proposed numerical optimization utilizes a geometry generation algorithm with B-splines to model different geometric parameters. The spline control points are used as design parameters. Therefore, the shape of the volute can vary freely during the optimization resulting in circular, trapezoidal, rectangular, or an other arbitrary shape. This allows a degree of freedom in design unprecedented in scientific publications regarding investigations of flows within volutes. Furthermore, the radial location of the cross-section is altered as well as the location of the volute inlet. Referencing to the five geometric specifications of a volute defined by Ayder et al. [7] in section 2.3, the presented optimization covers three of them: radial location of the volute channel, cross-sectional shape of the volute, and the inlet position of the volute. Only the area of the cross section and the tongue geometry are kept constant as characteristics of the volute.

The simulations were performed with the open source CFD software OpenFOAM. A new numerical model had to be developed since no included solver is suited for thermal turbomachinery simulations. The proposed model consists of a density-based solver utilizing the SLAU scheme of Shima and Kitamura [57, 89] for the inviscid flux

calculation in conjunction with a variable reconstruction using the van Leer slope limiter. Implicit residual smoothing, local time stepping and flux-preconditioning are implemented to improve convergence rate at low Mach numbers and reduce the computational time for steady-state simulations. In case of transient problems, dual time stepping is employed. Furthermore, the SST $k-\omega$ turbulence is extended for turbomachinery applications by adding the rotation and curvature correction (RC) developed by Smirnov and Menter [90].

Two validation cases were run to show the accuracy of the solver. Firstly, the laminar flow around a circular cylinder showed the temporal and spatial accuracy of the proposed solver for low Mach number flows. The integrated and local flow characteristics coincide very well with other publications and experimental data. In particular, the SLAU scheme showed its advantages compared to other flux calculation schemes, such as AUSM$^+$-up or HLLC. Secondly, the impeller of the Radiver centrifugal compressor is simulated. The results reveal a good accuracy of the numerical model for turbomachinery cases, which is on par with the commercial CFD code ANSYS Fluent.

The reference model of a centrifugal compressor was taken from a turbocharger for light commercial vehicles and passenger cars. A steady-state numerical model is developed utilizing the MRF approach to model the rotation of the compressor wheel. The results show a good agreement with the test bench data for low and high rotational speeds in terms of total pressure ratio. However, the isentropic efficiency is significantly overpredicted at low flow rates due to the definition of adiabatic walls. In these cases, the heat exchange with the surroundings cannot be neglected. However, due to missing data, conjugate heat transfer simulations could not be conducted. The results also indicate that the losses inside the volute are of the same order of magnitude as losses inside the compressor wheel. Therefore, the optimization of the volute and the reduction of losses is a viable and promising way to increase the overall compressor efficiency.

The optimization utilizes a genetic algorithm to find the volute shape with the highest performance. The objective function is defined as arithmetic average of isentropic efficiency at four different mass flow rates. Due to a linear correlation between total pressure ration and efficiency, it is sufficient to use only one objective function. The

genetic optimization extends over 40 generations and 2000 individual volute geometries in total. Due to the nearly constant compressor performance after 25 generations, it is feasible to finish the optimization after 40 generations. It is assumed that a continuation would not lead to significantly better results.

The optimized geometry consists of a circular shape with an overhung volute channel, a curved lower wall, and a tangential inlet. Compared to the reference model, the final geometry results in an increase of average isentropic efficiency of 0.5 % across all operating points. The improvement is minor at low flow rates. This is due the design point of the volute being in the range of (0.12 – 0.15) kg/s. The volute channel is large enough to decelerate the flow and increase the static pressure. Therefore, the losses are low. As the flow rate increases, the volute acts like a nozzle since it cannot accommodate high mass flow rates. Shear stress losses are also increased due to higher flow velocities. However, the optimized volute geometry is capable of reducing these losses. As a result, the isentropic compressor efficiency is increased by up to 2 % at 0.19 kg/s compared to the reference model. Furthermore, based on the volute performance, the static pressure recovery coefficient is increased by over 12 %. Even though a stage improvement of 2 % might appear small at first, it is very well in line with other optimization research [48, 54]. An additional positive aspect of the optimized geometry is its similar shape compared to the reference model. Therefore, there should be no problems in manufacturing the new geometry. In summary it can be stated that the performance curve of the optimized compressor is widened so it can operate more efficiently at higher off-design flow rates.

A direct comparison with other publications dealing with volute optimization is difficult due to their severe constraints in geometric freedom. For this reason, the geometric characteristics of the optimized geometry are broken down similarly to the previous sections: (1) volute inlet location, (2) radial location, and (3) cross-sectional shape of the volute. These three characteristics can be compared separately to corresponding research work.

This study found that the **volute inlet location** has a significant impact onto the volute flow and therefore the compressor performance. Although differences at low flow rates are small, high mass flow rates lead to an increase of up to 8 % using a tangential inlet compared to a symmetrical volute inlet. The optimized geometry has

an inlet eccentricity of 0.9. These findings are in line with other publications such as Abdelmadjid et al. [1] and Hassan [42]. Both investigated a centrifugal compressor and concluded an improvement of up to 10 % at high flow rates; less at lower flow rates, though. The characteristic flow pattern described by Chen et al. [24] are also recognized in this thesis as the main reason for the efficiency gains. However, the specification of an eccentricity for an optimal performance has not yet been defined in literature. Therefore, a comparison with other research work cannot be made.

The effect of the **radial location** of the volute channel is found to have a large influence onto the compressor performance as well. As the radial location is reduced, the efficiency is increased. In combination with a slightly curved lower wall, the volute offers the best results. This effect is in particular visible at high off-design flow rates. The reason for this lies in the better filling of the volute channel with lower near-wall velocity gradients and recirculation areas. These observations are in contrast to the very limited publications available regarding this topic. Mishina and Gyobu [74] used a rectangular shaped volute channel with different radial locations. They concluded, a smaller centroid radius leads to higher flow velocities at lower radii due to the conservation of angular momentum. Consequently, the periodic acceleration and deceleration of the fluid leads to higher losses. In addition, Stiefel [93] investigated two centrifugal compressor volutes to get similar results. However, the cross-sectional area of the volute channels in that research were not equal. Therefore, differences in performance cannot be attributed solely to the radial location. Although both publications are nearly 40 years old, no recent scientific work was conducted on this field. The results in this thesis now show that the filling of the volute is more efficient with a reduced centroid radius of the volute channel. Therefore, losses are reduced and outweigh the effect of the reacceleration due to the lower radii.

The third geometric characteristic is the **cross-sectional shape** of the volute channel. The results in this work indicate only a minor influence. Even when using a shape with a sharper edge, the effect onto the isentropic efficiency is less than 0.5 %. In addition to that as long as the first two geometric parameters are chosen well, the actual shape has nearly no influence at all onto the performance curve. The results in literature are quite diverse on this topic as shown in section 2.3.1. A direct comparison is difficult since a change in shape often results in slightly different inlet position or radial location of the volute channel. Therefore, it is ambiguous to attribute a change

in performance to different shapes.

The question whether the result of the numerical optimization is the *optimal* geometry cannot be answered. One can never rule out the possibility of a better shape. However, these observations are very important for identifying the main influencing geometric factors for the volute performance. Furthermore, the improvements of compressor performance help to reach future emission targets and reduce the output of greenhouse gases. Due to the wide field of application, the findings can also be adopted for large turbochargers in container ships, auxiliary power units for aircrafts and gas turbines in power technology. In all cases, a higher efficiency leads to the reduction of greenhouse gas and a cleaner environment.

8 Outlook

Even though the performed optimization is very comprehensive, there are still open questions and possibilities for improvements. These can be grouped into (1) the numerical model for the compressor simulations, (2) the setup for the genetic optimization, and (3) the area of application.

The proposed **numerical model** offers a good accuracy with experimental data in case of adiabatic walls. However, heat exchange with the surroundings at low compressor speeds lead to a reduction in isentropic efficiency. The developed model has to be extended to include conjugate heat transfer (CHT) to incorporate these effects. As an example, Bohn et al. [13] performed a CHT simulation of a turbocharger including compressor, oil cooled housing and turbine. The results showed the significant influence of heat transfer from the hot turbine side to the cold compressor side.

Another shortcoming of the model are the high calculation times. The developed density-based solver uses a segregated approach to solve the governing equation consequently. This restricts the maximum Courant number to values in the order of one due to stability reasons. Therefore, the time stepping size is severely restricted resulting in long calculation times. Mangani et al. [68] and Heyns et al. [46] implemented steady-state coupled approaches for solving the governing equations simultaneously and reduce the computational cost. They reported an speed up of factor $5 - 10$ for meshes with 10^6 elements.

Improvements to the **genetic optimization** setup are twofold. Firstly, the size of parameter space could be increased. This could be achieved by adding more control points to the B-spline for the volute shape generation. Alternatively, NURBS could be used instead of B-splines introducing an additional weighting factor for each control point. In both ways, the geometrical freedom could be increased allowing for more

complex shapes. However, it remains unclear whether more complexity would lead to better shapes and consequently higher volute performance. Investigations in this direction were not performed yet in the science community. The size of parameter space could also be increased by introducing additional variables such as the tongue geometry and cross-sectional area distribution. This way, all important volute geometry specification could be used. Either way, a larger parameter space would inevitably lead to a significant increase in computational cost for the optimization. For this reason, a better numerical model is required with lower calculation times.

Secondly, the numerical optimization could be improved by choosing a different evolutionary algorithm. There are newer bio- and socio-inspired algorithms, which promise better results in some applications. For instance, the Cuckoo optimization algorithm was developed by Rajabioun [84] and mimics the egg laying and breeding strategy of the bird family Cuckoo. Similarly, the Bat algorithm formulated by Yang [111] is based on the echolocation behavior of bats. Both algorithms offer an improved convergence and solution accuracy. However, it is uncertain whether the outcome of the presented optimization would be different. Nevertheless, faster convergence would be promising for future optimization applications.

Finally, a genetic optimization could be repeated for a different **area of application**. This includes the volute optimization for pumps, fans, and blowers. These results would show the transferability of the presented findings to different kinds of turbomachines. Moreover, this would lead to further insights regarding the dominant geometric volute parameters in general.

Bibliography

[1] C. Abdelmadjid, S.-A. Mohamed, and B. Boussad. "CFD Analysis of the Volute Geometry Effect on the Turbulent Air Flow through the Turbocharger Compressor". In: *Energy Procedia* 36 (2013), pp. 746–755. DOI: 10.1016/j.egypro.2013.07.087.

[2] B. M. Adams et al. *Dakota, A Multilevel Parallel Object-Oriented Framework for Design Optimization, Parameter Estimation, Uncertainty Quantification, and Sensitivity Analysis: Version 6.0 User's Manual*. Tech. rep. Sandia National Laboratories, USA, 2014, p. 331.

[3] T. Adams, C. Grant, and H. Watson. "A Simple Algorithm to Relate Measured Surface Roughness to Equivalent Sand-grain Roughness". In: *International Journal of Mechanical Engineering and Mechatronics* 1.1 (2012), pp. 66–71. DOI: 10.11159/ijmem.2012.008.

[4] A. Arnone, M.-S. Liou, and L. A. Povinelli. *Multigrid Time-Accurate Integration of Navier-Stokes Equations*. Tech. rep. 1993, NASA Technical Memorandum 106373. DOI: 10.2514/6.1993-3361.

[5] E. Ayder and R. Van den Braembussche. "Experimental Study of the Swirling Flow in the Internal Volute of a Centrifugal Compressor". In: *International Gas Turbine & Aeroengine Congress & Exhibition*. 1991, pp. 1–8. DOI: 10.1115/91-GT-007.

[6] E. Ayder and R. Van den Braembussche. "Numerical Analysis of the Three-Dimensional Swirling Flow in Centrifugal Compressor Volutes". In: *Journal of Turbomachinery* 116.3 (1994), p. 462. DOI: 10.1115/1.2929435.

[7] E. Ayder, R. Van den Braembussche, and J. J. Brasz. "Experimental and Theoretical Analysis of the Flow in a Centrifugal Compressor Volute". In: *Journal of Turbomachinery* 115 (1993), pp. 582–589. DOI: 10.1115/1.2929293.

[8] B. D. Baloni and S. A. Channiwala. "Design and Analysis of Volute Casing: A Review". In: *Proceedings of ASME Turbo Expo 2012: Turbine Technical Conference and Exposition*. Copenhagen, Denmark, 2012, pp. 657–664. DOI: 10.1115/GT2012-68056.

[9] B. D. Baloni, Y. Patak, and S. Channiwala. "Centrifugal Blower Volute Optimization Based on Taguchi Method". In: *Computers & Fluids* 112 (2015), pp. 72–78. DOI: 10.1016/j.compfluid.2015.02.007.

[10] O. Baris and F. Mendonca. "Automotive Turbocharger Compressor CFD and Extension Towards Incorporating Installation Effects". In: *Proceedings of ASME Turbo Expo 2011: Turbine Technical Conference and Exposition*. 2011. DOI: 10.1115/GT2011-46796.

[11] H. Berns and W. Theisen. *Ferrous Materials: Steel and Cast Iron*. Springer-Verlag, Berlin, Germany, 2008, p. 422. ISBN: 978-3-540-71848-2.

[12] J. Blazek. *Computational Fluid Dynamics: Principles and Applications*. Elsevier Ltd, 2001. ISBN: 978-0-080-44506-9.

[13] D. Bohn, T. Heuer, and K. Kusterer. "Conjugate Flow and Heat Transfer Investigation of a Turbo Charger". In: *Journal of Engineering for Gas Turbines and Power* 127 (2005), p. 663. DOI: 10.1115/1.1839919.

[14] P. Boncinelli and A. Arnone. "Impeller–Diffuser Interaction in Centrifugal Compressors: Numerical Analysis of Radiver Test Case". In: *Journal of Propulsion and Power* 23.6 (2007), pp. 1304–1312. DOI: 10.2514/1.27028.

[15] O. Borm. "Instationäre numerische Untersuchung der aerodynamischen Rotor-Stator-Interaktion in einem Radialverdichter". PhD Thesis. Technical University of Munich, 2012.

[16] O. Borm and Hans-Peter Kau. "Unsteady Aerodynamics of a Centrifugal Compressor Stage – Validation of Two Different CFD Solvers". In: *Proceedings of ASME Turbo Expo 2012: Turbine Technical Conference and Exposition*. Copenhagen, Denmark, 2012, pp. 1–12. DOI: 10.1115/GT2012-69636.

[17] F. Bouchon, T. Dubois, and N. James. "A Second-Order Cut-Cell Method for the Numerical Simulation of 2D Flows past Obstacles". In: *Computers & Fluids* 65 (2012), pp. 80–91. DOI: 10.1016/j.compfluid.2012.02.011.

[18] R. D. Bowerman and A. J. Acosta. "Effect of the Volute on Performance of a Centrifugal-Pump Impeller". In: *Transactions of the ASME* 56 (1957), pp. 1057–1069.

[19] M. P. Boyce. *Gas Turbine Engineering Handbook*. 4th. Elsevier Ltd, 2012. ISBN: 978-0-123-83842-1.

[20] J. Brokate, E.D. Özdemir, and U. Kugler. *Der Pkw-Markt bis 2040 : Was das Auto von morgen antreibt*. Tech. rep. 2013, Deutsches Zentrum für luft–und Raumfahrt e.V.

[21] W. B. Brown and G. R. Bradshaw. *Design and Performance of Family of Diffusing Scrolls with Mixed-Flow Impeller and Vaneless Diffuser*. Tech. rep. 1568. 1948, pp. 1–31.

[22] D. Chatterjee, K. Chatterjee, and B. Mondal. "Control of Flow Separation Around Bluff Obstacles by Transverse Magnetic Field". In: *Journal of Fluids Engineering* 134.9 (2012), pp. 134–143. DOI: 10.1115/1.4007316.

[23] H. Chen and P. Li. "Compressor Housing Design for Small Turbocharger Compressors". In: *Proceedings of ASME Turbo Expo 2013: Turbine Technical Conference and Exposition*. 2013, pp. 1–8. DOI: 10.1115/GT2013-94250.

[24] H. Chen, D. Tong, and X. Wang. "Vortices and Performance of Internal and External Volutes". In: *Proceedings of ASME Turbo Expo 2015: Turbine Technical Conference and Exposition*. Montreal, Quebec, Canada, 2015, pp. 1–8. DOI: 10.1115/GT2015-42462.

[25] Y.-H. Choi and C. L. Merkle. "The Application of Preconditioning in Viscous Flows". In: *Journal of Computational Physics* 105.2 (1993), pp. 207–223. DOI: 10.1006/jcph.1993.1069.

[26] C. Darwin. *On the Origin of Species*. United Kingdom, 1859.

[27] Q. Datong et al. "Experimental study on the noise reduction of an industrial forward-curved blades centrifugal fan". In: *Applied Acoustics* 70.8 (2009), pp. 1041–1050. DOI: 10.1016/j.apacoust.2009.03.002.

[28] S. C. R. Dennis and G.-Z. Chang. "Numerical Solution for Steaty Flow Past a Circular Cylinder at Reynolds Number up to 100". In: *Journal of Fluid Mechanics* 42.03 (1970), pp. 471–489. DOI: 10.1017/S0022112070001428.

[29] John D. Denton. "Some Limitations of Turbomachinery CFD". In: *Proceedings of ASME Turbo Expo 2010: Turbine Technical Conference and Exposition*. Glasgow, United Kingdom, 2010, pp. 1–11. DOI: 10.1115/1.3448334.

[30] DIN 4766. *Herstellverfahren der Rauheit von Oberflächen - Erreichbare gemittelte Rautiefe R_z nach DIN 4768 Teil 1*. 1981.

[31] R Dong, S. Chu, and J. Katz. "Effect of Modification to Tongue and Impeller Geometry on Unsteady Flow, Pressure Fluctuations, and Noise in a Centrifugal Pump". In: *Journal of Turbomachinery* 119 (1997), pp. 506–515. DOI: 10.1115/1.2841152.

[32] D. Eckardt. "Detailed Flow Investigations Within a High-Speed Centrifugal Compressor Impeller". In: *Journal of Turbomachinery* 98.3 (1976), pp. 390–399. DOI: 10.1115/1.3448334.

[33] B. Eckert and E. Schnell. *Axial- und Radialkompressoren*. 2nd. Springer, 1980. ISBN: 978-3-642-80544-8.

[34] Elsevier. *Scopus Journal Index*. 2015. URL: http://www.scopus.com (visited on Apr. 2, 2016).

[35] European Parliament and the Council. "Council Regulation (EU) No 333/2014". In: *Official Journal of the European Union* L 103 (2014), pp. 15–21.

[36] R. Gautier, D. Biau, and E. Lamballais. "A Reference Solution of the Flow over a Circular Cylinder at Re = 40". In: *Computers & Fluids* 75 (2013), pp. 103–111. DOI: 10.1016/j.compfluid.2012.12.017.

[37] P. E. Gill, W. Muray, and M. H. Wright. *Practical Optimization*. San Diego, California, USA: Academic Press, 1981, p. 401. ISBN: 978-0-122-83952-8.

[38] F. Gu et al. "A Numerical Investigation on the Volute/Diffuser Interaction Due to the Axial Distortion at the Impeller Exit". In: *Journal of Fluids Engineering* 123.3 (2001), p. 475. DOI: 10.1115/1.1385515.

[39] D. Hagelstein et al. “Experimental and Numerical Investigation of the Flow in a Centrifugal Compressor Volute”. In: *Journal of Turbomachinery* 122.1 (1999), pp. 22–31. DOI: 10.1115/1.555423.

[40] D. Hagelstein et al. “Experimental investigation of the circumferential static pressure distortion in centrifugal compressor stages”. In: *International Gas Turbine & Aeroengine Congress & Exhibition*. 1997, pp. 1–7. DOI: 10.1115/97-GT-050.

[41] A. Harten. “High Resolution Schemes for Hyperbolic Conservation Laws”. In: *Journal of Computational Physics* 49.3 (1983), pp. 357–393. DOI: 10.1016/0021-9991(83)90136-5.

[42] A. S. Hassan. “Influence of the volute design parameters on the performance of a centrifugal compressor of an aircraft turbocharger”. In: *Proceedings of the Institution of Mechanical Engineers, Part A: Journal of Power and Energy* 221 (2007), pp. 695–704. DOI: 10.1243/09576509JPE436.

[43] A. Hellsten. “Some Improvements in Menter’s $k-\omega$ SST turbulence model”. In: *29th AIAA Fluid Dynamics Conference*. 1998, pp. 1–11. DOI: 10.2514/6.1998-2554.

[44] F. Hellstrom, E. Gutmark, and L. Fuchs. “Large Eddy Simulation of the Unsteady Flow in a Radial Compressor”. In: *Journal of Turbomachinery* 134 (2012), pp. 1–10. DOI: DOI:10.1115/1.4003816.

[45] W. Hesse. *Material data sheets — Non-ferrous metals*. 1st. Beuth Verlag, 2014. ISBN: 978-3-410-23490-6.

[46] J. Heyns, O. Oxtoby, and A. Steenkamp. “Coupled solver for modelling high-speed flow”. In: *10th OpenFOAM Workshop*. Ann Arbor, Michigan, USA, 2015.

[47] Honeywell International Inc. *Turbocharger Forecast*. 2015. URL: https://turbo.honeywell.com/whats-new-in-turbo/press-release/honeywells-2015-turbocharger-forecast-signals-increased-expectations-of-turbo-technology-as-global-penetration-nears-50-percent-by-2020 (visited on Feb. 1, 2016).

[48] J. Huang et al. "Robust Performance Optimization of Centrifugal Compressor Volute With a Rectangular Cross-Section". In: *Proceedings of ASME Turbo Expo 2015: Power for Land, Sea and Air*. 2015, pp. 1–11. DOI: 10.1115/GT2015-42979.

[49] H. P. Hübl. *Beitrag zur Berechnung des Spiralgehäuses von Radialverdichtern und Vorherbestimmung seines Betriebsverhaltens*. Institut für Dampf- und Gasmaschinen, Technische Universität Wien, 1975, pp. 1–122.

[50] M. Ittershagen and S. G. Haufe. *UBA-Emissionsdaten 2014 zeigen Trendwende beim Klimaschutz*. Press release No. 14, Federal Environmental Agency (Umweltbundesamt), 2015.

[51] A. Jameson. "Time Dependent Calculations Using Multigrid, with Applications to Unsteady Flows Past Airfoils and Wings". In: *AIAA 10th Computational Fluid Dynamics Conference*. 1991, p. 14. DOI: 10.2514/6.1991-1596.

[52] A. Jameson. *Transonic Flow Calculations*. Tech. rep. Princeton University, 1983, MAE Report 1651.

[53] A. Jameson, W. Schmidt, and E. Turkel. "Numerical Solutions of the Euler Equations by Finite Volume Methods using Runge-Kutta Time-Stepping Schemes". In: *14th Fluid and Plasma Dynamics Conference*. Palo Alto, CA, USA, 1981. DOI: 10.2514/6.1981-1259.

[54] C.-M. Jang, J.-S. Lee, and S.-H. Yang. "Performance Evaluation of a Centrifugal Blower Using Optimal Design Method". In: *Proceedings of the ASME 2013 Fluids Engineering Division Summer Meeting, FEDSM2013*. 2013, pp. 1–7. DOI: 10.1115/FEDSM2013-16449.

[55] N. A. H. Jasni and M. A. Lajis. "A Comprehensive Study on Surface Roughness in Machining of AISI D2 Hardened Steel". In: *Advanced Materials Research* 576 (2012), pp. 60–63.

[56] J. H. Kim et al. "Design optimization of a centrifugal pump impeller and volute using computational fluid dynamics". In: *IOP Conference Series: Earth and Environmental Science*. Vol. 15. 2012. DOI: 10.1088/1755-1315/15/3/032025.

[57] K. Kitamura and E. Shima. "Improvements of Simple Low-Dissipation AUSM against Shock Instabilities in Consideration of Interfacial Speed of Sound". In: *European Conference on Computational Fluid Dynamics*. Lisbon, Portugal, 2010, pp. 1–20.

[58] F. Kock and H. Herwig. "Entropy production calculation for turbulent shear flows and their implementation in cfd codes". In: *International Journal of Heat and Fluid Flow* 26 (2005), pp. 672–680. DOI: 10.1016/j.ijheatfluidflow.2005.03.005.

[59] Kraftfahrtbundesamt. *Fahrzeugzulassungen (FZ)*. 2015.

[60] A. Kurganov, S. Noelle, and G. Petrova. "Semidiscrete Central-Upwind Schemes for Hyperbolic Conservation Laws and Hamilton-Jacobi Equations". In: *Journal of Computational Physics* 23.3 (2001), pp. 707–740. DOI: 10.1137/S1064827500373413.

[61] B. E. Launder and D. B. Spalding. "The Numerical Computation of Turbulent Flows". In: *Computer Methods in Applied Mechanics and Engineering* 3.2 (1974), pp. 269–289. DOI: 10.1016/0045-7825(74)90029-2.

[62] B. van Leer. "Towards the Ultimate Conservative Difference Scheme. II. Monotonicity and Conservation Combined in a Second-Order Scheme". In: *Journal of Computational Physics* 14.4 (1974), pp. 361–370. DOI: 10.1016/0021-9991(74)90019-9.

[63] B. Lendorff and H. Meienberg. *Detail-Entwicklung im Bau von Turboverdichtern*. Tech. rep. 1944, pp. 60–67.

[64] M.-S. Liou. "A sequel to AUSM, Part II: AUSM$^+$-up for all speeds". In: *Journal of Computational Physics* 214.1 (2006), pp. 137–170. DOI: 10.1016/j.jcp.2005.09.020.

[65] M.-S. Liou and C. J. Steffen. "A New Flux Splitting Scheme". In: *Journal of Computational Physics* 107 (1993), pp. 23–39. DOI: 10.1006/jcph.1993.1122.

[66] W. Lipski. "The influence of shape and location of the tongue of spiral casing on the performance of single stage radial pumps". In: *Proceedings of Sixth Conference of Fluid Machinery*. 1979, pp. 673–682.

[67] H. Luo, J. D. Baum, and R. Löhner. "On the computation of multi-material flows using ALE formulation". In: *Journal of Computational Physics* 194.1 (2004), pp. 304–328. DOI: 10.1016/j.jcp.2003.09.026.

[68] L. Mangani, M. Darwish, and F. Moukalled. "Development of a Pressure-based Coupled CFD Solver for Turbulent and Compressible Flows in Turbomachinery Applications". In: *Proceedings of ASME Turbo Expo 2014: Turbine Technical Conference and Exposition*. Düsseldorf, Germany, 2014, pp. 1–13. DOI: 10.1115/FEDSM2013-16082.

[69] D. J. Mavriplis, A. Jameson, and L. Martinelli. "Multigrid Solution of the Navier-Stokes Equations on Triangular Meshes". In: *27th Aerospace Sciences Meeting*. Reno, Nevada, USA, 1989. DOI: 10.2514/3.25233.

[70] F. R. Menter. "Two-Equation Eddy-Viscosity Turbulence Models for Engineering Applications". In: *AIAA Journal* 32 (1994), pp. 1598–1605. DOI: 10.2514/3.12149.

[71] F. R. Menter and T. Esch. "Elements of Industrial Heat Transfer Predictions". In: *16th Brazilian Congress of Mechanical Engineering (COBEM)*. Uberlandia, Minas Gerais, Brazil, 2001, pp. 117–127.

[72] F. R. Menter, M. Kuntz, and R. Langtry. "Ten Years of Industrial Experience with the SST Turbulence Model". In: *Turbulence, Heat and Mass Transfer 4*. Antalya, Turkey, 2003, pp. 625 –632. DOI: 10.4028/www.scientific.net/AMR.576.60.

[73] C. L. Merkle and M. Athavale. "A Time Accurate Unsteady Incompressible Algorithm Based on Artificial Compressibility". In: *8th Computational Fluid Dynamics Conference*. 2. Honolulu, Hawaii, USA, 1987, pp. 397–407. DOI: 10.2514/6.1987-1137.

[74] H. Mishina and I. Gyobu. "Performance Investigations of Large Capacity Centrifugal Compressors". In: *ASME Paper 78-GT-3* (1978), pp. 1–11. DOI: 10.1115/78-GT-3.

[75] H. Mohtar et al. "Effect of Diffuser and Volute on Turbocharger Centrifugal Compressor Stability and Performance: Experimental Study". In: *Oil & Gas Science and Technology* 66.5 (2011), pp. 779–790. DOI: 10.2516/ogst/2011139.

[76] M. Mojaddam, A. H. Benisi, and M. R. Movahhedy. "Investigation on Effect of Centrifugal Compressor Volute Cross-Section Shape on Performance and Flow Field". In: *Proceedings of ASME Turbo Expo 2012: Turbine Technical Conference and Exposition*. Copenhagen, Denmark, 2012, pp. 1–10. DOI: 10.1115/GT2012-69454.

[77] M. Mojaddam, A. Hajilouy-Benisi, and M. R. Movahhedy. "Optimal Design of the Volute for a Turbocharger Radial Flow Compressor". In: *Proceedings of ASME Turbo Expo 2014: Turbine Technical Conference and Exposition*. Düsseldorf, Germany, 2014, pp. 1–9. DOI: 10.1115/GT2014-26849.

[78] L. Moroz et al. "Integrated Conceptual Design Environment for Centrifugal Compressors Flow Path Design". In: *Proceedings of International Mechanical Engineering Congress and Exposition IMECE*. Boston, Massachusetts, USA, 2008, pp. 1–11. DOI: 10.1115/IMECE2008-69122.

[79] OpenFOAM Foundation Ldt. *OpenFOAM Version 2.4.0*. 2015. URL: http://www.openfoam.org.

[80] S. Patankar. *Numerical Heat Transfer and Fluid Flow*. McGraw-Hill, 1980. ISBN: 0-07-048740-5.

[81] D. V. Patil and K. N. Lakshmisha. "Finite Volume TVD Formulation of Lattice Boltzmann Simulation on Unstructured Mesh". In: *Journal of Computational Physics* 228.14 (2009), pp. 5262–5279. DOI: 10.1016/j.jcp.2009.04.008.

[82] N. M. Patrikalakis and T. Maekawa. *Shape Interrogation for Computer Aided Design and Manufacturing*. 2001, pp. 1–408. ISBN: 978-3-642-04074-0.

[83] C. Pfleiderer. *Die Kreiselpumpen*. 1st. Springer, 1924. ISBN: 978-3-662-42863-4.

[84] R. Rajabioun. "Cuckoo optimization algorithm". In: *Applied Soft Computing Journal* 11.8 (2011), pp. 5508–5518. DOI: 10.1016/j.asoc.2011.05.008.

[85] A. Reunanen et al. "Computational and Experimental Comparison of Different Volute Geometries in a Radial Compressor". In: *International Gas Turbine & Aeroengine Congress & Exhibition*. Munich, Germany, 2000, pp. 1–10. DOI: 10.1115/2000-GT-0469.

[86] H. Schlichting and K. Gersten. *Grenzschichttheorie*. 10th. Springer-Verlag, Berlin, Germany, 2006. ISBN: 978-3-540-32985-5.

[87] M. Schobeiri. *Turbomachinery Flow Physics and Dynamic Performance*. Springer-Verlag, Berlin, Germany, 2012. ISBN: 978-3-642-24675-3.

[88] K. Schreiner. *Basiswissen Verbrennungsmotor*. 2nd. 2015. ISBN: 978-3-658-06186-9.

[89] E. Shima. "A Compressible CFD Method for Flow with Sound from very low Mach Number to Supersonic". In: *BBAA VI International Colloquium on: Bluff Bodies Aerodynamics & Applications*. Milano, Italy, 2008, pp. 20–24.

[90] P. E. Smirnov and F. R. Menter. "Sensitization of the SST Turbulence Model to Rotation and Curvature by Applying the Spalart-Shur Correction Term". In: *Journal of Turbomachinery* 131.4 (2009), pp. 1–8. DOI: 10.1115/1.3070573.

[91] D. B. Spalding. "A Single Formula for the Law of the Wall". In: *Journal of Applied Mechanics* 28.3 (1961), pp. 455–458. DOI: 10.1115/1.3641728.

[92] A. Stepanoff. *Centrifugal and Axial Flow Pumps: Theory, Design and Application*. 2nd. Wiley, 1957. ISBN: 978-0-894-64723-9.

[93] W. L. Stiefel. *Experiences in the Development of Radial Compressors*. Tech. rep. May. Bruessels, Belgium: von Karman Institut, 1972, pp. 1–160.

[94] Z. Sun, C. Tan, and D. Zhang. "Flow Field Structures of the Impeller Backside Cavity and its Influences on the Centrifugal Compressor". In: *Proceedings of ASME Turbo Expo 2009: Turbine Technical Conference and Exposition*. Milano, Italy, 2009. DOI: 10.1115/GT2009-59879.

[95] W. Sutherland. "The Viscosity of Gases and Molecular Force". In: *Philosophical Magazine* (1893), pp. 507–531.

[96] K. Taira and T. Colonius. "The Immersed Boundary Method: A Projection Approach". In: *Journal of Computational Physics* 225.2 (2007), pp. 2118–2137. DOI: 10.1016/j.jcp.2007.03.005.

[97] D. J. Tritton. "Experiments on the Flow Past a Circular Cylinder at Low Reynolds Numbers". In: *Journal of Fluid Mechanics* 6.4 (1959), pp. 547–567. DOI: 10.1017/S0022112059000829.

[98] P. G. Tucker. "Computation of unsteady turbomachinery flows: Part 1—Progress and challenges". In: *Progress in Aerospace Sciences* 47.7 (2011), pp. 522–545. DOI: 10.1016/j.paerosci.2011.06.004.

[99] P. G. Tucker. "Computation of unsteady turbomachinery flows: Part 2—LES and hybrids". In: *Progress in Aerospace Sciences* 47.7 (2011), pp. 546–569. DOI: 10.1016/j.paerosci.2011.07.002.

[100] P. G. Tucker. "Trends in turbomachinery turbulence treatments". In: *Progress in Aerospace Sciences* 63 (2013), pp. 1–32. DOI: 10.1016/j.paerosci.2013.06.001.

[101] E. Turkel. "Preconditioning Techniques in Computational Fluid Dynamics". In: *Annual Review of Fluid Mechanics* 31.1 (1999), pp. 385–416. DOI: 10.1146/annurev.fluid.31.1.385.

[102] S. Velarde-Suárez et al. "Reduction of the aerodynamic tonal noise of a forward-curved centrifugal fan by modification of the volute tongue geometry". In: *Applied Acoustics* 69.3 (2008), pp. 225–232. DOI: 10.1016/j.apacoust.2006.10.009.

[103] T. Verstraete, Z. Alsalihi, and R. A. Van den Braembussche. "Numerical Study of the Heat Transfer in Micro Gas Turbines". In: *Journal of Turbomachinery* 129 (2007), pp. 835–841.

[104] A. Weiß. "Spannungs- und verformungsinduzierte Martensitbildungen in metastabilen austenitischen CrNi-Stählen". Habilitation. TU Bergakademie Freiberg, 2011.

[105] J. M. Weiss and W. A. Smith. "Preconditioning Applied to Variable and Constant Density Flows". In: *AIAA Journal* 33.11 (1995), pp. 2050–2057. DOI: 10.2514/3.12946.

[106] D. C. Wilcox. "Formulation of the $k-\omega$ Turbulence Model Revisited". In: *AIAA Journal* 46.1 (2008), pp. 2823–2838. DOI: 10.2514/6.2007-1408.

[107] C. H. K. Williamson. "Oblique and Parallel Modes of Vortex Shedding in the Wake of a Circular Cylinder at low Reynolds Numbers". In: *Journal of Fluid Mechanics* 206 (1989), pp. 579–627. DOI: 10.1017/S0022112089002429.

[108] R. C. Worster. "The Flow in Volutes and its Effect on Centrifugal Pump Performance". In: *Proceedings of the Institution of Mechanical Engineers* 177 (1963), pp. 843–875. DOI: 10.1243/PIME_PROC_1963_177_061_02.

[109] C. Xu and M. Müller. "Development and Design of a Centrifugal Compressor Volute". In: *International Journal of Rotating Machinery* 3 (2005), pp. 190–196. URL: 10.1155/IJRM.2005.190.

[110] S. Yang, F. Kong, and B. Chen. "Research on Pump Volute Design Method Using CFD". In: *International Journal of Rotating Machinery* 2011 (2011), pp. 1–7. DOI: 10.1155/2011/137860.

[111] X.-S. Yang. "A New Metaheuristic Bat-Inspired Algorithm". In: *Studies in Computational Intelligence*. 2010, pp. 65–74. DOI: 10.1007/978-3-642-12538-6_6.

[112] K. U. Ziegler, H. E. Gallus, and R. Niehuis. "A Study on Impeller-Diffuser Interaction—Part I: Influence on the Performance". In: *Journal of Turbomachinery* 125 (2003), pp. 173–182. DOI: 10.1115/1.1516814.

[113] K. U. Ziegler, H. E. Gallus, and R. Niehuis. "A Study on Impeller-Diffuser Interaction—Part II: Detailed Flow Analysis". In: *Journal of Turbomachinery* 125 (2003), pp. 183–192. DOI: 10.1115/1.1516815.